ALICE

TECHNISCHE
UNIVERSITÄT
MÜNCHEN

Fakultät für Physik

Bachelor Thesis

Production of light (anti)nuclei in Xe–Xe collisions at $\sqrt{s_{\mathrm{NN}}} = 5.44$ TeV measured with ALICE at the LHC

Gleb Shchepetnev

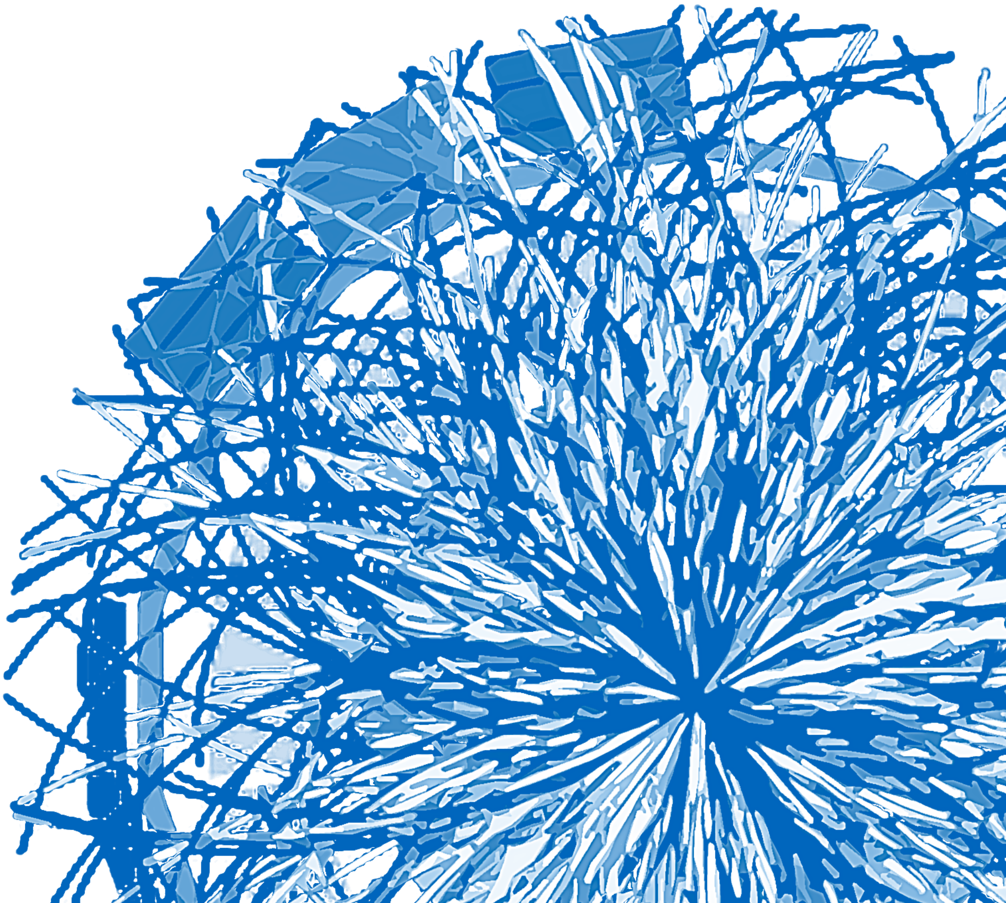

TECHNISCHE UNIVERSITÄT MÜNCHEN

ALICE

Fakultät für Physik

Production of light (anti)nuclei in Xe−Xe collisions at $\sqrt{s_{\mathrm{NN}}} = 5.44$ TeV measured with ALICE at the LHC

Produktion von leichten (Anti)Kernen in $\sqrt{s_{\mathrm{NN}}} = 5.44$ TeV Xe−Xe Kollisionen gemessen mit ALICE am LHC

Bachelor Thesis

Author: Gleb Shchepetnev
Supervisor: Prof. Dr. Laura Fabbietti
Examiner: Dr. Jan Friedrich
Advisor: Dr. Chiara Pinto
Date: 19.10.2022

I confirm that the results presented in this bachelor's thesis is my own work and I have documented all sources and materials used.

Ich versichere, dass ich diese Bachelorarbeit selbstständig verfasst und nur die angegebenen Quellen und Hilfsmittel verwendet habe.

Garching b. Munich, 19.10.2022 Gleb Shchepetnev

Abstract

The tracking and particle identification capabilities of ALICE allow detailed studies of hadron production at high energies, densities, and multiplicities. Results can shed light on the processes behind (anti)nuclei formation and can serve as an input in the indirect dark matter searches; they can also help to have insight into the state of the early Universe, where a state of deconfined matter, called Quark Gluon Plasma, is created. In the present work, the production of (anti)deuteron and (anti)helium nuclei are measured for the first time in the Xe−Xe collisions at the center-of-mass energy per nucleon-nucleon pair of $\sqrt{s_{\mathrm{NN}}} = 5.44$ TeV. Ratios between the yields of nuclei and those of protons are compared with previous results from the ALICE Collaboration in different collision systems and energies, and to predictions from different nucleosynthesis models. The comparisons confirm a smooth transition between the different collision systems, suggesting a common production mechanism across multiplicities. The coalescence parameters B_2 and B_3 are calculated and B_2 is compared to the results of EPOS simulations. Chemical freeze-out temperature is obtained from the integrated yields of deuterons, helions and previously measured protons and its value agrees with previous measurements and calculations.

Contents

1 Introduction

Dark matter (DM) is expected to account for the 27% of the matter in the Universe [1], however, not much is known about it. The two defining characteristics of DM are its darkness (nongravitaional interactions are rare) and a very long lifetime [2]. These conclusions arise from studies of the rotation curves of galaxies, measurements of anisotropies in the cosmic microwave background, weak gravitational lensing and other cosmological and astrophysical observations. Many theories of DM compete to provide a plausible explanation for the observed phenomena but are confronted with the challenges of experimental searches and navigating in the complexity of possible signatures. A promising scenario is that of subatomic Weakly Interacting Massive Particles (WIMPs) [3]. WIMPs feature in many theories of the physics beyond the Standard Model (SM), with hints to their existence found in both particle physics and cosmology. To confirm or to falsify the idea of WIMP DM would mean a tremendous progress in DM searches and in the understanding of our Universe.

Many experiments were proposed to look for possible physical consequences of DM. There are two main branches of DM research: on the one hand, the direct detection experiments aim to observe direct interactions between the dark and ordinary matter. On the other hand, indirect detection experiments look for DM through decays into or annihilation of SM particles. Other indirect searches include collider experiments, which seek to detect missing transverse energy and infer the presence of invisible particles [2]. In the end, a confirmation from an independent experiment is needed to provide independent evidence of (non)observation.

As mentioned above, the WIMP hypothesis has attracted a significant interest in the scientific community and is currently under active research. Assuming that WIMPs behave somewhat similar to the ordinary SM particles, one could expect them to annihilate with their antiparticles or with themselves if they are Majorana particles. Products of such process can then as well be the ordinary weak bosons or quarks which decay into lighter particles or hadronize. This hypothesis is illustrated in Figure 1.1, which sketches the annihilation of a WIMP DM (marked with χ) through an unspecified interaction (question marks), resulting in showers of SM particles including ordinary (anti)nuclei. If such processes take place in space, they can affect the magnitude and the composition of cosmic rays, i.e. of high energy particles moving through interstellar space. By measuring the primary cosmic ray particles that reach the Earth (or its vicinity), evidence for DM decays can be established from an excess in (anti)nuclei fluxes over the predicted background originating from interactions of primary cosmic rays (CRs) with interstellar medium (ISM). Precise measurements of cosmic rays are therefore of particular value to the indirect DM searches. Figure 1.2 shows several calculations of background and

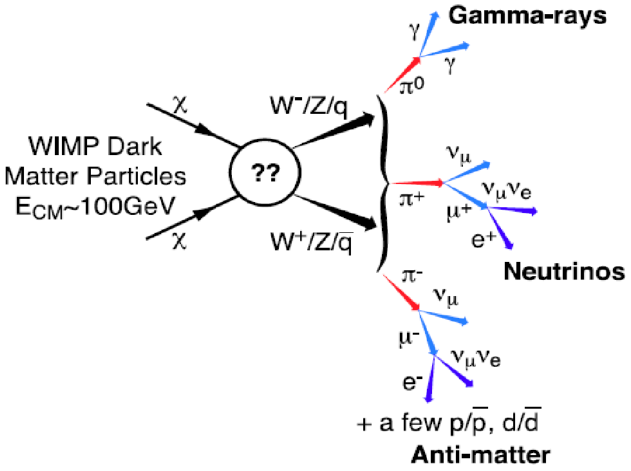

Figure 1.1: Sketch of a hypothetical WIMP annihilation through an unspecified interaction into several SM-channels.

DM flux for antihelium as a function of kinetic energy per nucleon in several models. To be able to interpret any future measurements of antinuclei in space, one consequently needs precise knowledge of the production, propagation, and annihilation of ordinary nuclei in space. Unfortunately, mechanisms of nuclei production are still unclear and can not be derived from the first principles of QCD[1]. This creates the necessity to study the (anti)nuclei production in a controlled environment, e. g., in a collider experiment. Of special interest are antideuterons and antihelions due to their negligible astrophysical backgrounds at low kinetic energies [4].

Interpretation of the measured antinuclei fluxes can serve as evidence for the existence of WIMPs. In 2018 the AMS-02 [5] on board of the international space station announced the observation of eight antihelium candidates [6], although the results have not been published in a peer-reviewed journal. Their confirmation would deliver a breakthrough in DM searches, as the results would be difficult (if possible) to reconcile with the present understanding of physics.

Constraining the inputs into the dark matter studies is not the only reason to study (anti)nuclei production in colliders. As it is mentioned above, the production mechanism of light (anti)nuclei is yet to be determined. Also unresolved is the question of how light nuclei, with their binding energies of several MeV, can survive the highly energetic environment, in which their formation is thought to take place according to the currently available production models. Several models have been proposed to explain different aspects of these phenomena, the main two being statistical hadronization and coalescence. Tests of these models depend crucially on the measurements of nuclei production in collisions of ultra-relativistic heavy ions since those offer a unique opportunity to produce and study thousands of particles in a controlled environment.

---

[1] Quantum chromodynamics, the theory of the strong interaction.

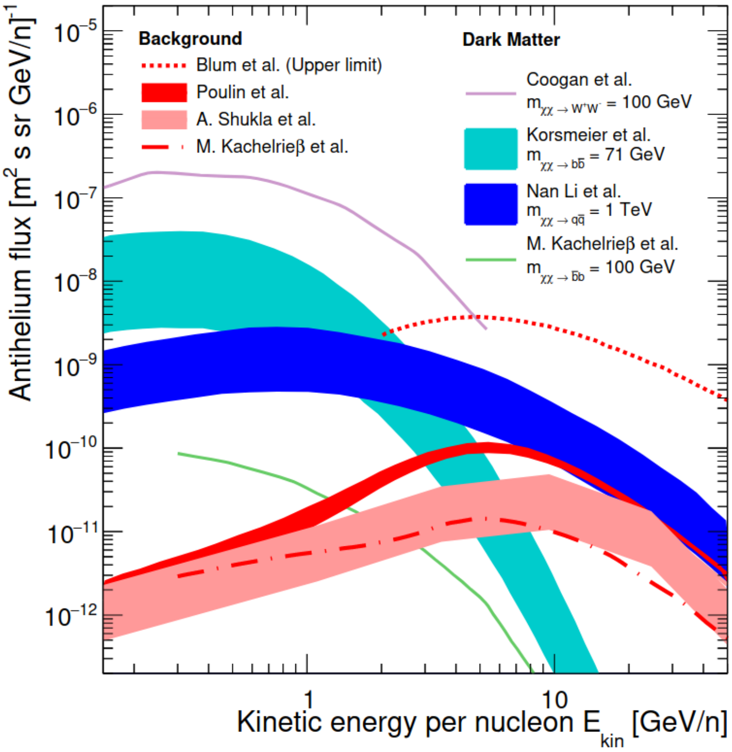

Figure 1.2: Flux predictions for $^{3}\overline{\mathrm{He}}$ for different models of DM annihilation and background calculations [7].

This thesis is structured in the following way: Chapter 2 reviews some of the theoretical ideas behind the studies in heavy-ion collisions which are relevant to this work. The experimental setup of the ALICE apparatus at CERN is described in Chapter 3. The analysis of experimental data, the main part of the work, is presented thoroughly in Chapter 4 and the results are reported in Chapter 5. The thesis is concluded with a summary of the performed study and a discussion of the results, as well as an outlook for future developments (Chapter 6).

2 Theoretical background

This Chapter summarizes some of the ideas which guide a part of the research of heavy-ion physics at ALICE in general and are relevant to this work in particular. It is structured as follows: first, general information on the production and evolution of nuclear matter is given in Section 2.1. Since the complex interactions of thousands of particles produced in collisions can not be described with the principles of QCD, phenomenological models were developed to describe observations; two main classes of these models are briefly reviewed in Sections 2.2 and 2.3. Finally, some useful definitions and relations, used to analyze experimental data, are given in Section 2.4.

2.1 Nuclear matter at the LHC

In ultra-relativistic heavy-ion collisions (anti)matter is produced under extreme conditions, resembling those of the early Universe [8]. Due to very high energies and densities, for a short time matter existed in a deconfined state, characterized by weakly interacting quarks and gluons, forming a plasma (the so-called Quark-Gluon-Plasma, QGP). Quantum chromodynamics, the theory of the strong interaction, explains how hadrons can not form under these conditions because of the running coupling constant: it vanishes at high energies and the strong force becomes ever weaker, a phenomenon known as asymptotic freedom. The energies at which such matter is produced in colliders can be expressed using temperature T since QGP is assumed to be in (local) thermodynamic equilibrium, and they reach hundreds of MeV. At the same time particles and antiparticles are indistinguishable by their interactions, resulting in their equal numbers, so that the baryochemical potential μ_B[1] is zero. T and μ_B define a phase diagram of the nuclear matter, as sketched in Figure 2.1. The region representing the early Universe is marked with a white arrow. Ordinary nuclear matter occupies a small area at $T \sim 0$ and $\mu_B \sim 1$ GeV. It is surrounded by hadron gas which undergoes a phase transition into QGP at higher temperatures. The critical point indicates where the energy density becomes continuous and a crossover takes place for lower values of μ_B at around $T \sim 160$ MeV. Regions investigated in different experiments are also shown, with the LHC achieving a vanishing baryochemical potential at high temperatures.

The evolution of the collision system at the LHC can be roughly divided into several stages in its proper time[2]. First, relativistically contracted (in the laboratory frame) nuclei-disks clash ($t = 0$) and set off hard scattering processes, characterized by high

---

[1] The baryochemical potential is defined as $\mu = (\partial E/\partial B)_{S,V}$, where E is the energy and B the baryon number of the system. It is more closely discussed in Section 2.2

[2] Here, time is measured in fm/c since fm is a typical scale of the strong force and particles are moving at velocities close to c.

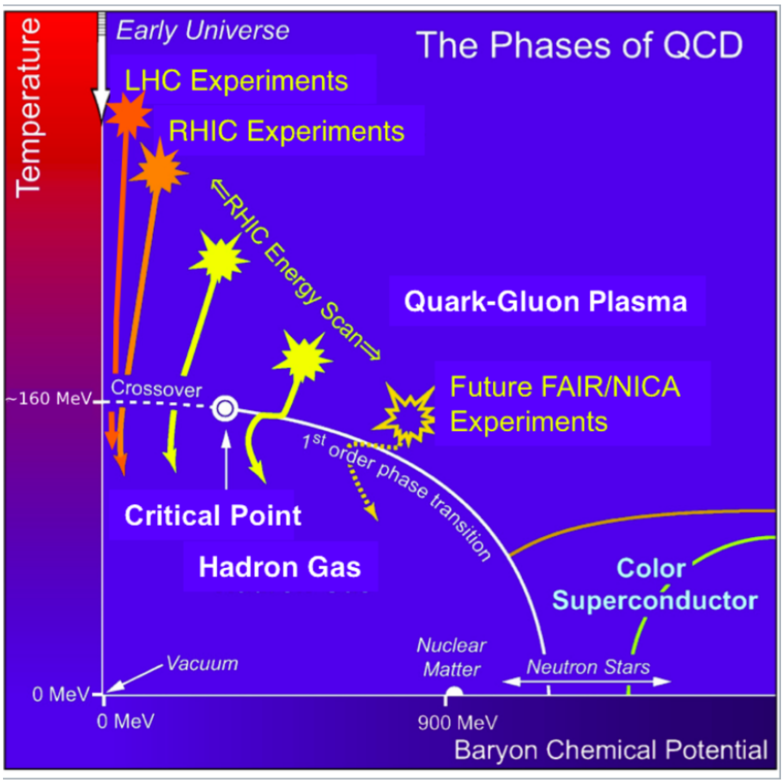

Figure 2.1: Phase diagram of strongly interacting matter (image taken from [9]).

momentum transfer between partons before ($t \lesssim 1$ fm/c) a thermal equilibrium is reached and the QGP is formed. The medium cools down as it expands and eventually undergoes a transition into hadron resonance gas at around 10 fm/c after the initial collision. This corresponds to the crossover in Figure 2.1 and is called chemical freeze-out because the average transferred momentum is not sufficient to cause inelastic processes, thus fixing the hadron chemistry. Elastic collisions continue, changing the momentum spectra of the particles, until the mean free path becomes so large that all interactions stop: a kinetic freeze-out occurs. Hadrons move further away from the interaction region and eventually reach detectors.

2.2 Statistical Hadronization Models

The following overview is based on Ref. [10].

Since extreme densities are achieved in heavy-ion collisions, and particles are produced at high multiplicities, it is natural to invoke a statistical description to explain some of the observed phenomena. The class of models that realize this approach is called statistical hadronisation models or thermal models. Their core assumption is that all final hadronic states are equally likely, if they are compatible with the conservation laws dictated by the Standard Model of particle physics [10]. This follows from the Liouville's theorem for a (closed) system at equilibrium. The conserved quantities are the quantum numbers of the system (usually charge Q, baryon number B, strangeness S), each with a corresponding chemical potential (μ_Q, μ_B, μ_S); they are used to construct a partition function[3]. The Hamiltonian H describes a hadron resonance gas and reproduces all mesons and baryons with masses up to around 1.5 GeV/c^2 and 2 GeV/c^2, respectively. Macroscopic quantities of the system, such as the average particle number, are obtained from the partition function using known thermodynamic relations.

For large systems like Pb−Pb agreement between data and prediction is achieved by using Grand Canonical (GC) ensemble. In this case, five free parameters of the partition function (the three chemical potentials μ_Q, μ_B, μ_S, temperature T and volume V) can be reduced to three by assuming strangeness (fixes μ_S) and charge (fixes μ_Q) conservation, with the latter value determined by the isospin assymetry of the colliding nuclei. The ensemble-average multiplicity $\langle N_i \rangle$ of species i is obtained as[4] (more details can be found in [10]):

$$\langle N_i \rangle = \frac{VTg_i}{2\pi^2} \sum_{k=1}^{\infty} \frac{(\pm 1)^{k+1}}{k} \lambda_i^k m_i^2 K_2 \left(\frac{k m_i}{T} \right) \tag{2.1}$$

where m_i is the particle mass, g_i spin-isospin degeneracy factor, K_2 the modified Bessel function and $\lambda_i \equiv \exp\{(B_i\mu_B + S_i\mu_S + Q_i\mu_Q)/T\}$ the fugacity[5]. By building particle ratios $\langle N_i \rangle / \langle N_k \rangle$ the volumes V cancel out and only two free parameters remain: the baryochemical potential μ_B and the temperature T. The ratios therefore provide an accessible observable for a direct comparison between model and data. This is exploited in Section 5.4.

To get the total measured multiplicity $\langle N_i \rangle$ one has to consider an additional term which describes contributions from resonance decays (j):

$$\langle N_i \rangle (T, V, \vec{\mu}) = \langle N_i \rangle^{\text{th}} (T, V, \vec{\mu}) + \sum_j \Gamma_{j \to i} \langle N_j \rangle^{\text{th, R}} (T, V, \vec{\mu}) \tag{2.2}$$

where $\langle N_i \rangle^{\text{th}}$ and $\langle N_i \rangle^{\text{th, R}}$ denote the thermal average number of particle i and of resonance j, respectively, and $\Gamma_{j \to i}$ the branching ratio of the decay $j \to i$. The model can be extended by including corrections related to repulsive interactions of hadrons and strangeness suppression in the partition function.

Figure 2.2 shows global fits of particle yields[6] measured by the ALICE Collaboration in Pb−Pb collisions at $\sqrt{s_{\text{NN}}} = 5.02$ TeV with three different implementations of the thermal model. At the LHC energies it can be safely assumed that matter is produced in the same amount as antimatter[7] which implies a vanishing baryochemical potential

---

[3] Similarly to how the chemical potential μ (of the particle number N) is contained in the fugacity $\lambda = e^{-\mu N \beta}$ of the Grand Canonical partition function of standard statistical mechanics (here $\beta = 1/(k_B T)$, with temperature T and the Boltzmann constant k_B).

[4] Here $k_B \equiv 1$.

[5] As hinted above, $\langle N_i \rangle$ is found by calculating the GC partition function $Z_i(T, V, \vec{\mu}) = \text{Tr}\left(e^{-\beta H} \lambda_i\right)$ and then using the relation $\langle N_i \rangle = \lambda_i [\frac{\partial}{\partial \lambda_i} \ln Z_i(T, V, \vec{\mu})]_{T, V}$.

[6] $\mathrm{d}N/\mathrm{d}y$ is discussed in Section 2.4, it is a quantity directly connected to particle multiplicity.

[7] See, for example, Refs. [11], [12], [13]

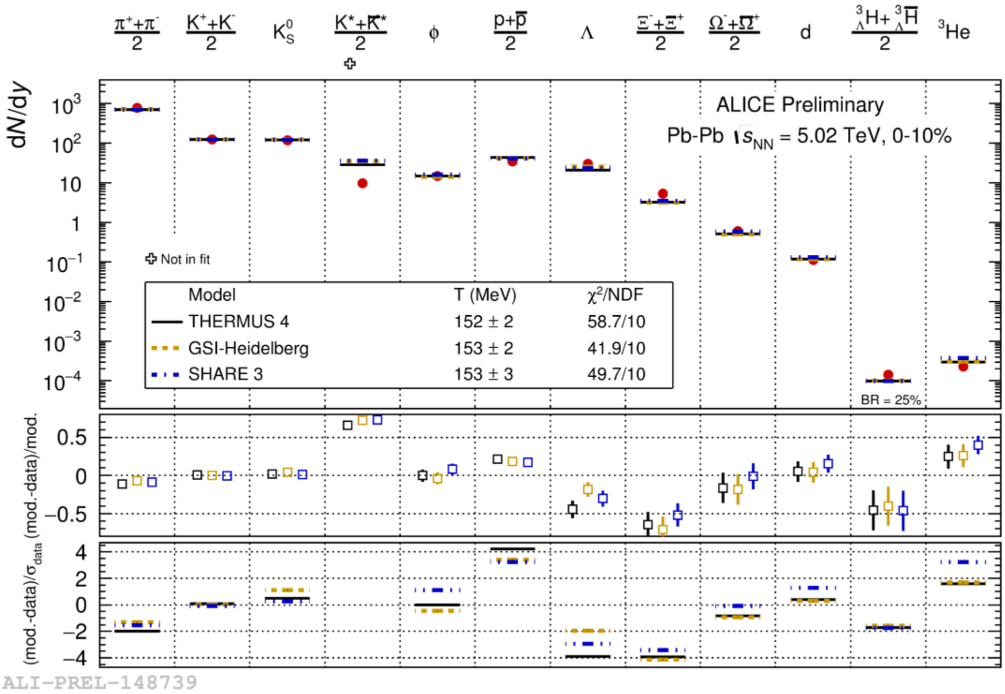

Figure 2.2: Thermal model fits to the hadron yields measured in central Pb−Pb collisions at $\sqrt{s_{\mathrm{NN}}} = 5.02$ TeV by ALICE. The fits are performed with three implementation of the statistical hadronisation models. The parameters that are estimated from the fits are the chemical freeze-out temperature T and the volume V (ALICE preliminary results).

$\mu_B = 0$. The chemical freeze-out temperature, which describes the transition of QGP to a hadron gas, is found to be around 153 MeV [14]. A slightly higher value of around 156 MeV is estimated for Pb−Pb collisions at $\sqrt{s_{\mathrm{NN}}} = 2.76$ TeV [15]. Calculations in lattice QCD predict comparable values of around 155 MeV [16]. These findings suggest that hadrons and mesons are produced in a thermodynamic equilibrium characterized by a common (freeze-out) temperature for all particles.

In case of smaller collision systems (e. g. pp or p−Pb) a better description is achieved with Canonical models (CSM) [10], which require exact conservation of charges (Q, B, S). This limits the number of accessible multi-hadronic states, a phenomenon called canonical suppression.

2.3 Coalescence models

Another approach used to predict the hadron production mechanism is implemented in coalescence models. They assume that nuclei are formed at the kinetic freeze-out with the probability dictated by how close nucleons are in phase space, i. e. by how close their momenta and position are. The key observable in such models is the coalescence parameter B_A, related to the probability to produce nuclei of mass number A with respect to protons (p):

$$E_A \frac{\mathrm{d}^3 N_A}{\mathrm{d}p_A^3} = B_A \left(E_\mathrm{p} \frac{\mathrm{d}^3 N_\mathrm{p}}{\mathrm{d}p_\mathrm{p}^3} \right)^A \Bigg|_{\vec{p}_\mathrm{p} = \frac{\vec{p}_A}{A}} \tag{2.3}$$

where $E\,\mathrm{d}^3N/\mathrm{d}p^3$ is invariant yield of nucleons (p) and nuclei (A) (see Section 2.4) and the nucleus momentum $\vec{p}_A$ is assumed to be distributed evenly among its A nucleons, $\vec{p}_\mathrm{p} = \vec{p}_A/A$. The (approximate) isospin-invariance of the strong force is used to equate proton and neutron yields and momentum distributions.

In the simplest version of the model [17], B_A is independent of the particle momentum and the size of the emitting source:

$$B_A = \frac{2J_A + 1}{2^A} \frac{1}{A^3} \frac{1}{A!} \left(\frac{4\pi}{3} p_0^3 \right)^{A-1} \frac{M_A}{m^A} \tag{2.4}$$

where M_A is the mass and J_A the spin of the nucleus, m the mass of the nucleon, and p_0 the maximum relative momentum of the nucleons required for binding[8]. As B_A was shown to depend on both nucleus momentum and event centrality [11], more advanced models of coalescence were developed. The state-of-the-art description uses Wigner density function to describe probability distribution of the nucleus in momentum space for a given final state (expressed as a nuclear wave function in coordinate space) and a correlation function.

2.4 Kinematic observables

This section summarizes some of the observable quantities frequently used in high energy heavy-ion physics, and in particular in the following chapters of the present work. This section use natural units, $\hbar = c = 1$, for compactness. In the following, the direction of the flight of a particle is set to be the z axis in the laboratory frame and the x and y axis define a plane perpendicular to it. It is a useful prescription for describing particle kinematics on colliders, see Chapter 3.

Transverse momentum p_T, defined as the component of particle momentum perpendicular to the longitudinal axis z ($p_\mathrm{T} = \sqrt{p_x^2 + p_y^2}$), often plays a central role in high energy scattering experiments since it is the same in the colliding system's rest frame and the laboratory frame of the experiment (particles are accelerated along the beam axis z so no Lorentz boost is applied in the transverse plane) and is always related to the processes at the collision point. The particles travelling in the transverse plane are carrying a part of the center-of-mass energy, which is available for the particle production, while the ones that continue moving longitudinally may have not participated in the collisions (called spectators).

---

[8] When only momentum correlations are considered, as it is the case in the simple coalescence, Eq. 2.3 can be rewritten in terms of the probability to find A out of total of N nucleons inside a sphere with radius p_0 in homogeneous momentum space. This results in Eq. 2.4 without the factor $(2J_A + 1)/2^A$, which reflects the probability for the nucleons to match the spin of the resulting nucleus.

Another useful quantity is the rapidity, defined as:

$$y = \frac{1}{2} \ln \frac{E + p_z}{E - p_z} = \frac{1}{2} \ln \frac{\sqrt{m^2 + p^2} + p \cos\theta}{\sqrt{m^2 + p^2} - p \cos\theta} \tag{2.5}$$

for a particle of mass m and energy E, momentum p, emitted at an angle θ with respect to the beam axis; p_z is its longitudinal momentum. Rapidity has two valuable qualities: it is additive (unlike the velocity) and rapidity intervals are unchanged by a Lorentz boost in the z direction. It follows from the definition that $|y| \to \infty$ if the particle has low transverse momentum, and $y = 0$ if it travels perpendicular to the beam axis. Hence measurements in the mid-rapidity region $0.5 < y < 0.5$ provide Lorentz-invariant quantities describing the particles created in the collisions.
Pseudo-rapidity is defined as:

$$\eta = -\ln\tan(\theta/2) = \frac{1}{2} \ln \frac{|p| + p_z}{|p| - p_z} \tag{2.6}$$

It can be used to describe spatial coverage of detectors around the collision point. In the high energy limit, $p \gg m$, these two quantities coincide:

$$y \approx \frac{1}{2} \ln \frac{|p| + p\cos\theta}{|p| - p\cos\theta} = \eta \tag{2.7}$$

When measuring particle production as a function of some accessible observable, e. g. the transverse momentum, it is preferable to work with a Lorentz invariant quantity. A quick calculation shows that $\mathrm{d}^3p\,/E$ does not change under a Lorentz boost β in the longitudinal direction z:

$$dp'_z = \gamma\,(dp_z - \beta dE) = \gamma\left(dp_z - \beta\frac{p_z dp_z}{E}\right) = \frac{dp_z}{E}\gamma\,(E - \beta p_z) = \frac{dp_z}{E}E'$$

where the primed quantities (E', p'_z) describe the system moving with the velocity β in the reference frame of the unprimed system (E, p_z) and γ is the Lorentz factor[9]. The first and the last equality follow from the ordinary Lorentz transformations and the second one from the differentiation $\mathrm{d}E/\mathrm{d}p_z = p_z/E$. Thus, the invariant differential yield can be expressed as:

$$E\frac{d^3N}{d^3p} = E\frac{d^3N}{\mathrm{d}p_T dp_z} = \frac{d^3N}{\mathrm{d}p_T dy} \tag{2.8}$$

where it is used that $\mathrm{d}p_z/E = \mathrm{d}y$, which follows from Definition 2.5. This and the previous quantities are extensively used throughout this work.

---

[9] $The Lorentz factor is defined as \gamma \equiv 1/\sqrt{1-\beta^2}$ in natural units.

3 Experimental setup

The Large Hadron Collider (LHC) is currently the world's most powerful particle accelerator, reaching colliding energies of the order of several TeV. Among the four major experiments located at the LHC, ALICE is the most suitable one for the study of heavy-ion interactions, production of nuclear matter, and the properties of the Quark Gluon Plasma. The present chapter provides a brief overview of the LHC and the ALICE detector under the conditions at which it is found at the time of the data collection for Xe−Xe collisions.

3.1 LHC at CERN

The CERN research complex (see Figure 3.1) consists of an intricate chain of accelerators and other experimental facilities. Before being injected into the LHC, particles undergo several stages of acceleration and beam manipulation, with the exact steps being different for protons and larger nuclei, like Pb and Xe. This is due to the production methods and the initial degree of ionization: protons are obtained by acting with an electric field on atoms of hydrogen gas, ionizing them. The resulting protons are then directly injected and accelerated in a linear accelerator LINAC2 as a first step in the CERN's accelerator chain; they then undergo a step-wise acceleration in Proton Synchrotron Booster (PSB), the Proton Synchrotron (PS), and the Super Proton Synchrotron (SPS), before being injected into the LHC. The Pb ions, on the other hand, are extracted from a purified lead sample, heated up to 500°C by microwave radiation; the partially ionized nuclei are then guided to another linear accelerator LINAC3, after which they pass a stripper foil, losing more electrons. The following stages in the preparation of beams include the Low Energy Ion Ring (LEAR) and the already mentioned PS, in which another aluminium stripper foil rids the lead ions of the remaining electrons. The resulting beams are accelerated once again in the SPS and then guided to the LHC. A similar procedure is employed for Xe, with a dedicated ion source and modifications made to LINAC3 [18, 19, 20].

As mentioned above, LHC is the final component of the CERN's complex. It is a 26.7 km long machine consisting of two opposite rings, with sections dedicated to curving the beam trajectory (realized through 1232 superconducting dipole magnets), focusing of the beam (realized through 392 superconducting quadrupole magnets), and acceleration (16 radiofrequency cavities). The beam pipes are operated with an ultra-high vacuum to prevent collisions with residual gas atoms. The maximum energies reached by the LHC are $\sqrt{s_{\mathrm{NN}}} = 5.02$ TeV (Pb−Pb), $\sqrt{s_{\mathrm{NN}}} = 5.44$ TeV (Xe−Xe), $\sqrt{s_{\mathrm{NN}}} = 8.16$ TeV (p−Pb), and $\sqrt{s} = 13$ TeV (pp) during Run 2 and $\sqrt{s} = 13.6$ TeV (pp) at the start of Run 3. Here, $\sqrt{s}$ indicates the center-of-mass energy of proton collisions and $\sqrt{s_{\mathrm{NN}}}$ that of ions per nucleon pair, calculated as:

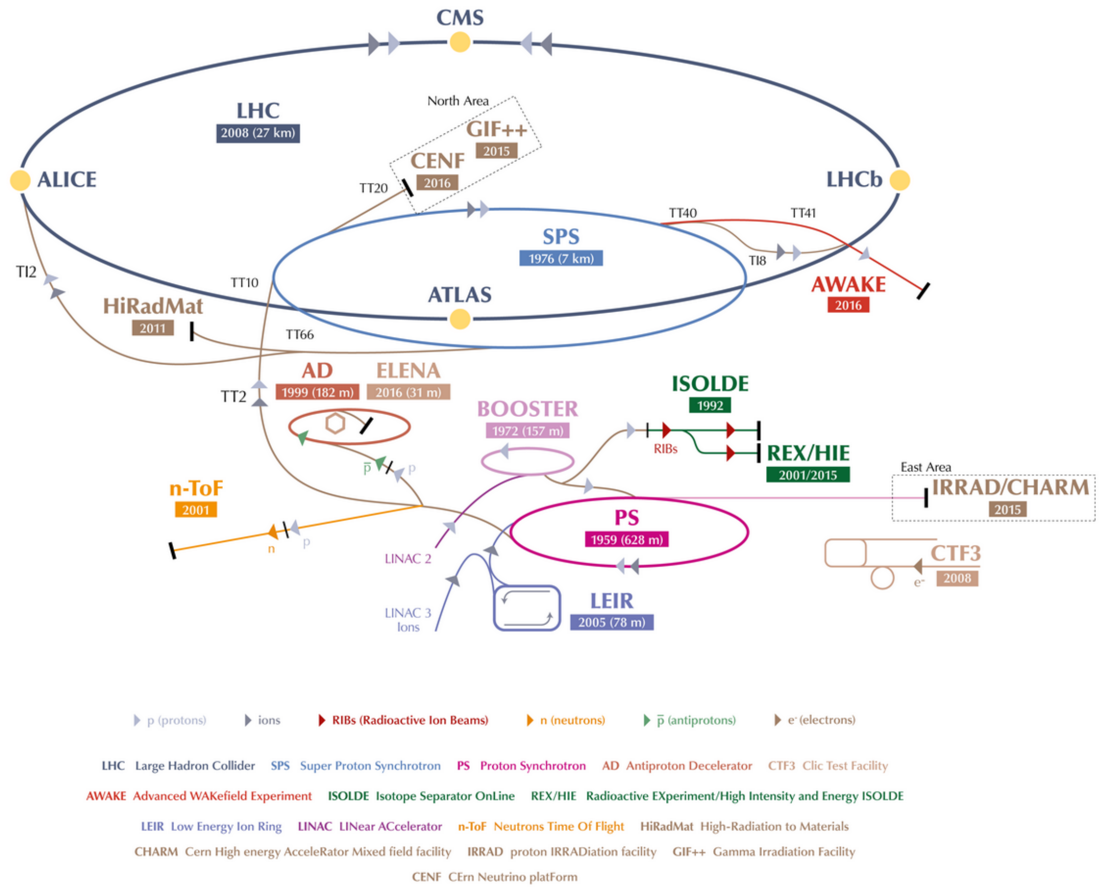

Figure 3.1: CERN accelerator complex; image taken from [21].

$$\sqrt{s_{\mathrm{NN}}} = \sqrt{Z_i/A_i}\sqrt{Z_k/A_k}\sqrt{s} \tag{3.1}$$

where $\sqrt{Z/A}$ is the correction for the ion i and k, contained in two beams (A being the atomic mass number and Z is the atomic charge).

The LHC has four points at which two oppositely rotating beams cross each other (yellow circles in Figure 3.1). The four main LHC experiments, ALICE, ATLAS, CMS, and LHCb, are located there. The two biggest detectors, ATLAS and CMS, were designed to investigate a bright spectrum of particle physics phenomena; they are located at the points of highest luminosity[1] and are equipped with multi-purpose detectors. The smallest experiment of the four, LHCb, is dedicated to studying the physics of particles with a charm or a beauty quark. It is a low-luminosity experiment that employs a series of forward detectors for particles flying in one direction. The main components of the ALICE detector relevant to this analysis are described in the following.

---

[1] Luminosity is a characteristic of an experimental setup, defined as $L = \frac{N_{\mathrm{B}}N_{\mathrm{B}}}{A}\nu$, where ν is the frequency, with which particle bunches with $N_{\mathrm{A,B}}$ particles collide with each other crossing the area A.

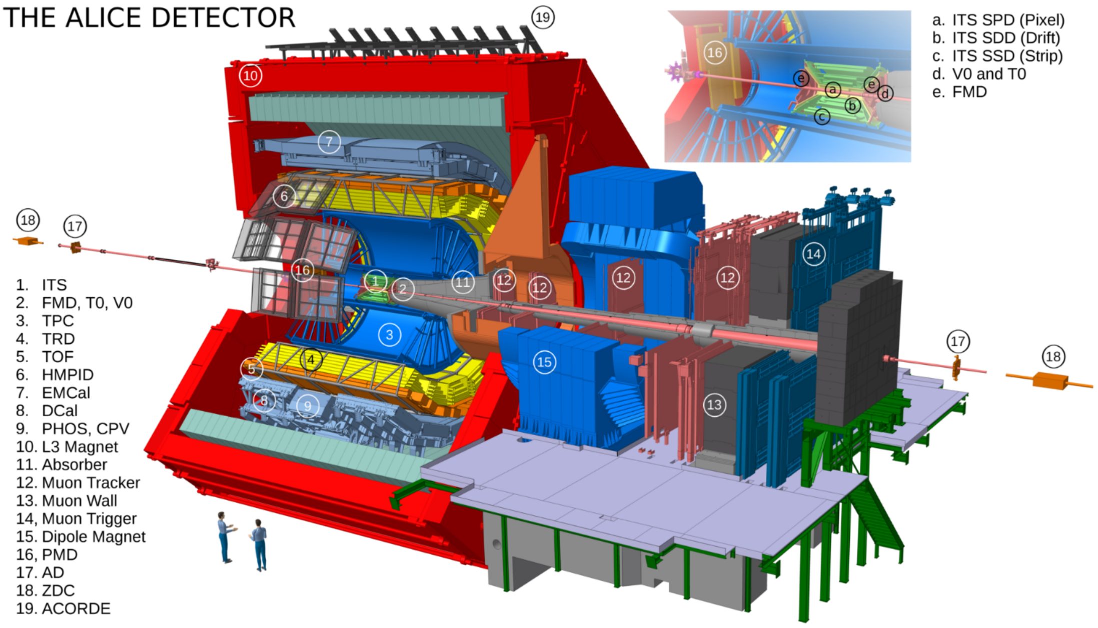

Figure 3.2: The ALICE apparatus during Run 2 (2015-2018).

3.2 ALICE detector

The ALICE (A Large Ion Collider Experiment) detector is designed to study the physics of strong interactions under high densities and temperatures using heavy ion probes. The complete setup has dimensions of $26 \times 16 \times 16$ m^3 and weights around 10^4 t. A model of the experiment, including its components, is shown in Figure 3.2. The detector can be divided into three parts: the central barrel (1, 3–9) embedded in a solenoidal magnet (10) which provides the fields of $0.2 - 0.5$ T, the arrays of forward detectors (2, 17, 18), and the muon arm (12–14).

Since collisions of heavy ions inevitably produce a high number of particles, the detector was specifically optimized to cope with extremely high values of charged particle multiplicity densities of up to $\langle \mathrm{d}N_{\mathrm{ch}}/\mathrm{d}\eta \rangle = 8000$ in the midrapidity region. It has a low material budget, allowing for light (anti)nuclei measurements at low momenta; also for this reason the magnetic field is kept at (relatively) low values. The present analysis is performed with the detectors located in the central barrel: the Inner Tracking System, the Time Projection Chamber, and the Time of Flight detector. The description of the detector systems is based on the ALICE performance report [22].

Inner Tracking System

The Inner Tracking System (ITS) is the closest detector to the collision points, providing the full azimuthal acceptance and the pseudorapidity coverage of $|\eta| < 0.9$. It consists of six cylindrical layers produced with three different technologies. The two innermost layers make up the Silicon Pixel Detector, used for the reconstruction of primary (i. e.,

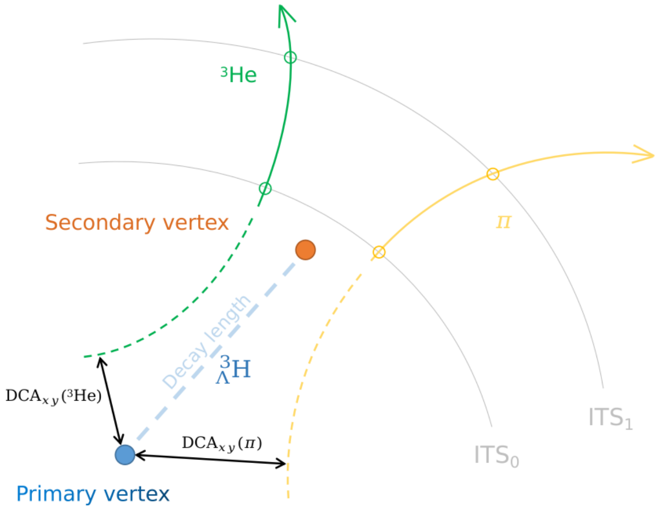

Figure 3.3: Schematic representation of the track reconstruction using the ITS for the hypertriton decay ($^3_\Lambda\mathrm{H} \to {}^3\mathrm{He} + \pi^-$). The full blue point indicates the primary vertex, in which hypertriton is produced, while the full orange point indicates the secondary vertex. The solid lines represent the reconstructed tracks of helion (light teal) and pion (light orange), while the dashed lines show extrapolations to the primary vertex. The SPD layers of the ITS are drawn as light grey lines; the intersections with the tracks symbolize measured signals.

collision) and secondary (i. e., points of decay of unstable particles) vertices in a high multiplicity environment as well as for determining the distance of closest approach DCA, defined as the closest distance between the extension of the reconstructed track and the primary vertex; this is exemplified in the sketch of Figure 3.3 for hypertriton decay ($^3_\Lambda\mathrm{H} \to {}^3\mathrm{He} + \pi^-$) (DCA is also discussed in the next chapter). DCA value plays a vital role in determining the origin of detected particles: primary from collisions or secondary from weak decay or spallation processes, i. e. from interaction with the detector material or the beam pipe. The other four layers constitute the Silicon Strip Detector (SSD) and the Silicon Drift Detector (SDD). These also provide tracking information and can additionally serve as a particle spectrometer at low momentum values by measuring particle energy loss. Furthermore, the outermost SSD is essential for track matching between the ITS and the TPC; see next Subsection.

Time Projection Chamber

The Time Projection Chamber (TPC) is the main tracking device of ALICE. It consists of a cylindrical field cage with an inner diameter of 1.2 m and an outer diameter of 5 m, covering the pseudorapidity region of $|\eta| < 0.9$, see Figure 3.4. It is divided into two chambers by the central high voltage electrode, which creates uniform electric fields of 400V/m parallel to the beam axis. Each chamber is filled with a mixture of Ar-CO$_2$ gas (90%-10%), which gets ionized by the charged particles traversing the active TPC volume. The electric field then guides the freed electrons to the end plates of the cage, where the multi-wire proportional chambers (MWPC) amplify their signal by creating an electron avalanche. The cathode plane of MWPC is divided into 18 trapezoidal sectors

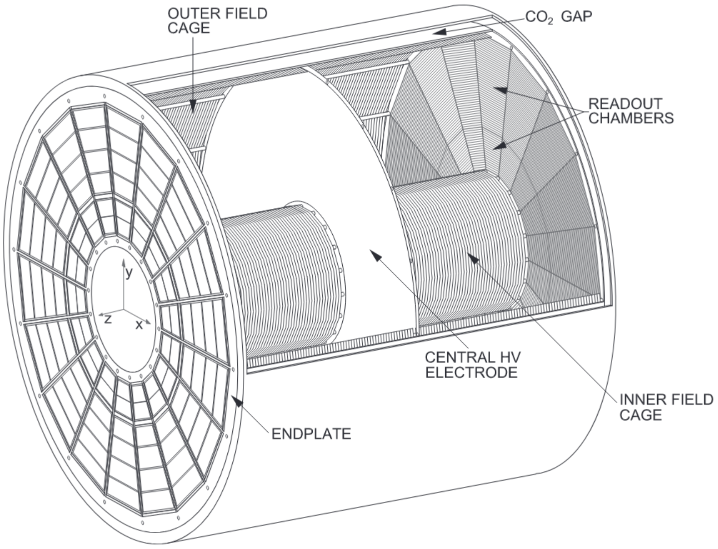

Figure 3.4: Schematic layout of the Time Projection Chamber; individual components are explained in text.

in the azimuthal direction and 159 pads in the radial direction (570132 pads in total). A row of pads with a measured signal (which can be associated with a track) is referred to as a cluster, with the maximum number of clusters for a particle being 159, following the discussion above. It is obvious that a higher number of clusters allows for better track reconstruction. The number of electrons detected in by each pad is indicative of the energy deposited by the passing particle over a given distance. This is denoted by the specific energy loss $\mathrm{d}E/\mathrm{d}x$, which allows particle identification using the Bethe-Bloch formula, which reads in its simplest form:

$$\frac{\mathrm{d}E}{\mathrm{d}x} = -\frac{4\pi}{m_e c^2}\frac{nZ^2}{\beta^2}\left(\frac{e^2}{4\pi\epsilon_0}\right)^2\left[\ln\left(2m_e c^2\beta^2/I\left(1-\beta^2\right)\right)-\beta^2\right] \tag{3.2}$$

where β is the particle's velocity in units of the speed of light c, E and Z are its energy and charge, m_e and e are the electron mass and charge, respectively, x is the traveled distance, n is the electron density of the target, and I parametrizes the target's mean excitation energy. The particle identification procedure is demonstrated in Chapter 4. The energy loss measurement is complemented by the measurement of the arrival time with respect to the nominal time of the collision, as well as the spatial coordinates of the triggered pads. This information, together with the data collected by the ITS, is used for track reconstruction with a subsequent back-propagation to estimate the primary vertex.

The TPC is characterized by excellent tracking and PID capabilities over a wide momentum range (from 0.1 GeV/c up to 100 GeV/c) with a p_T-resolution ranging from 1% at 1 GeV/c to about 3% at 10 GeV/c and a $\mathrm{d}E/\mathrm{d}x$-resolution of about 5 to 7%, depending on the collision system. This comes at the cost of a considerable electron drift time (around 90 μs), which results in a lower data acquisition rate of around 1 kHz.

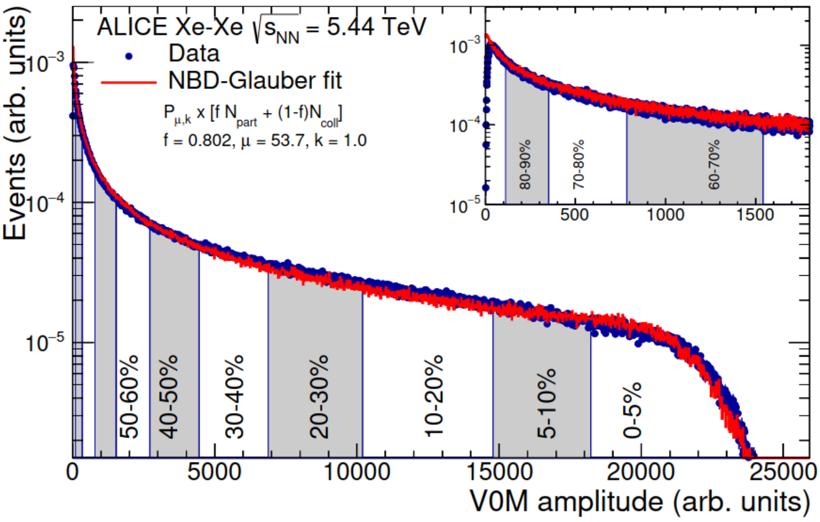

Figure 3.5: Distribution of the sum of amplitudes in the V0 scintillators for Xe−Xe collisions at $\sqrt{s_{\rm NN}} = 5.44$ TeV. The distribution is fitted with the NBD-Glauber fit shown as a red line. The inset shows the most peripheral region.

Time of Flight Detector

Another detector critical for the current analysis is the Time Of Flight detector (TOF). Like the TPC, it also provides full azimuthal coverage in the central pseudorapidity region of $-0.9 < \eta < 0.9$. The TOF cage is filled with a gas mixture of $C_2H_2F_4$ (90%), C_4H_{10} (5%), and SF_6 (5%), and has a high voltage applied to its external surfaces. It consists of 1593 individual Multigap Resistive-Plate Chambers, which detect electrons released in hard collisions of the gas molecules with passing particles. The main observable is the time of the signal with respect to the time of the collision. Details of the particle identification with the TOF detector are given in Analysis Chapter.

TOF is used for the PID in the intermediate transverse momentum range, up to around 3 GeV/c for lighter particles like pions and up to 6 GeV/c for deuteron. The time resolution depends on the collision system, being around 80 ps in Pb−Pb and 120 ps in pp collisions.

Other detectors

Other detectors shown in Figure 3.2 are less relevant to the current study, having been designed for different applications and conditions. Noteworthy, however, is the VZERO (V0M) detector, which consists of two arrays of forward scintillators counters, V0A and V0C, covering the pseudorapidity regions of $2.8 < \eta < 5.1$ (direction of particles is close to the beam axis, according to the definition of pseudorapidity Eq. 2.6) and $-3.7 < \eta < -1.7$ (particles fly almost antiparallel to the beam axis), respectively. The V0M provides the minimum bias (MB) trigger, defined as a signal in either V0A, V0C, or SPD. The centrality c of a collision can be defined as [23]:

$$c = \frac{\int_0^b \mathrm{d}\sigma/\mathrm{d}b'\mathrm{d}b'}{\int_0^\infty \mathrm{d}\sigma/\mathrm{d}b'\mathrm{d}b'} = \frac{1}{\sigma_{NN}} \int_0^b \frac{\mathrm{d}\sigma}{\mathrm{d}b'}\mathrm{d}b' \tag{3.3}$$

with σ_{NN} being the total nuclear interaction cross-section, b the impact parameter of the event and $\mathrm{d}\sigma/\mathrm{d}b'$ the impact parameter distribution. In ALICE, the centrality is measured as the percentile of the hadronic cross section corresponding to a particle multiplicity above a given threshold [23]; the cross section distributions can be replaced by the corrected number of observed events, so that the centrality can be estimated via the number of recorded particles per event. One usually restricts the total cross-section (or equivalently the event number) to exclude the large QED contributions coming from the ultra-peripheral collisions, thus considering the centrality between 0 and 90%. The results of such a study for the Xe−Xe system are shown in Figure 3.5 with a Glauber model fit and the resulting centrality classes, indicated by blue and white sections under the fit.

Another noteworthy detector is the Transition Radiation Detector (TRD), located between the TPC and the TOF. Its main purpose is to provide additional identification for electrons and pions; thus, it is not exploited in this work. It does, however, affect the number of particles that can reach the TOF due to absorption in its material; this can be used to measure the inelastic cross-section of particles (the so-called TPC-TOF method). In this analysis the TRD is considered when calculating the systematic uncertainty due to imprecise track matching between the TPC and the TOF detectors.

4 Analysis

In the following chapter the methods used to analyze the data and the logic behind them are described. It is organized as follows: first, the observables of the experiment and the measures taken to improve data quality are explained in Section 4.1.1. The discussion is continued in Section 4.1.2, where it is explained how relevant particle species can be identified and isolated from the rest of the data sample, which is then shown in Sections 4.1.3 and 4.1.4. The following four sections are dedicated to the discussion of the corrections applied to the measurements to take into account the finite resolution of the experiment. Finally, the systematic uncertainties, introduced in the previous steps of the analysis, are addressed in Section 4.3.

4.1 Raw spectra extraction

4.1.1 Event and track selection

The data studied in this analysis were collected with the ALICE detector during Run 2 of the LHC in October 2017. Xenon nuclei ($^{190}\mathrm{Xe}^{54+}$) collided at the center-of-mass energy of $\sqrt{s_{\mathrm{NN}}} = 5.44$ TeV for the first time at the LHC with the beams provided by the SPS. The luminosity amounted to $3 \times 10^{-25}\mathrm{cm}^{-2}\mathrm{s}^{-1}$ [18], and the detected hadronic interaction rate was around $80 - 150$ Hz. The solenoidal magnet of the ALICE apparatus was operated in a low-field configuration of 0.2 T. A total of about $1.14{\times}10^{6}$ events ($\sim 79\%$ of the recorded events), fulfilling the minimum requirements listed below, was collected with a minimum bias (MB) trigger (corresponding to the centrality of $0 - 90\%$). The average charged particle multiplicity density of MB events was calculated by combining the values of individual centrality classes taken from [24], amounting to $\langle \mathrm{d}N_{\mathrm{ch}}/\mathrm{d}y \rangle = 331.3 \pm 7.9$.

The analysis is done at midrapidity ($|y| < 0.5^{1}$) in the geometrical region $|\eta| < 0.8$, where the full azimuthal coverage of the ALICE central barrel is given. The primary vertex of events is required to have a maximum distance of 10 cm to the nominal interaction point with at least one contributor per vertex.

For the purposes of studying particle production, only primary particles are considered, i. e. those which are directly produced in collisions. To improve the quality of reconstructed tracks, some basic cuts are applied, similar to previous analyses by the ALICE Collaboration [11, 12, 13, 25]. The selection criteria reflect the characteristics of the detector during Run 2 [26]. They allow to increase the resolution of the track momentum and $\mathrm{d}E/\mathrm{d}x^{2}$, while suppressing the background from tracks with wrongly associated hits.

---

[1] Definitions of y, η and other used quantities are given in Section 2.4

[2] See Sections 3.2 and 4.1.3.

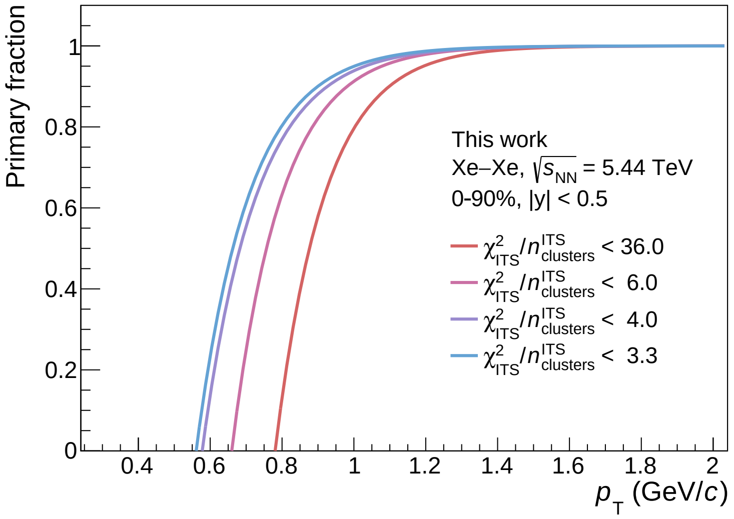

Figure 4.1: Dependence of the number of (anti)deuteron candidates on the DCA cuts.

Some of the imposed conditions (e. g. on DCA, χ^2_{ITS} as discussed below) also contribute to minimizing the number of secondary nuclei originating from interactions with the detector material or the beam pipe, as well as from weak decays. The track selection proved useful for achieving a reasonable data quality while keeping most of the relevant tracks. The minimum number of clusters of the TPC ($n^{\mathrm{TPC}}_{\mathrm{clusters}}$) which registered the passing of a given particle is required to be at least 70 out of 160. The same restriction applies to the number of pads crossed by a track but not resulting in a signal due to the limited reconstruction efficiency. The goodness of a trajectory fit, quantified by its χ^2 value, is required to be below 4 per cluster for the TPC measurements and below 36 per cluster for the ITS. However, the latter was further constrained to 3.3 for (anti)deuteron measurements done with the TPC at lower momenta: the selection reduces the number of deuteron candidates while leaving the number of antiparticles unaffected. This leads to a reduction in the fraction of secondary nuclei (produced in spallation processes with the detector material) since the antideuterons are assumed to originate mostly from the primary collisions rather than from other processes due to the baryonic number conservation. This is illustrated in Figure 4.1, which shows the best fit-to-data functions describing the evolution of the primary fraction with transverse momentum, for different values of the $\chi^2/n^{\mathrm{ITS}}_{\mathrm{clusters}}$ cuts[3] It is clear that the stricter cut of 3.3 allows to perform the analysis of particles with $p_{\mathrm{T}} \gtrsim 0.6$ GeV/c, while $\chi^2/n^{\mathrm{ITS}}_{\mathrm{clusters}} < 36$ results in a vanishing primary contribution for $p_{\mathrm{T}} \lesssim 0.8$ GeV/c. The discussion of the primary fraction is continued in Section 4.2.3.

To ensure a reliable reconstruction, tracks are also required to have at least two hits in the ITS detector ($n^{\mathrm{ITS}}_{\mathrm{clusters}}$). Additionally, it is required for deuteron candidates to be registered by at least one of the two innermost ITS layers ($n^{\mathrm{SPD}}_{\mathrm{hits}}$). Strong suppression of secondary nuclei comes from constraining the discrepancy between the origin of a

---

[3] How these functions are obtained is described in detail in Section 4.2.3.

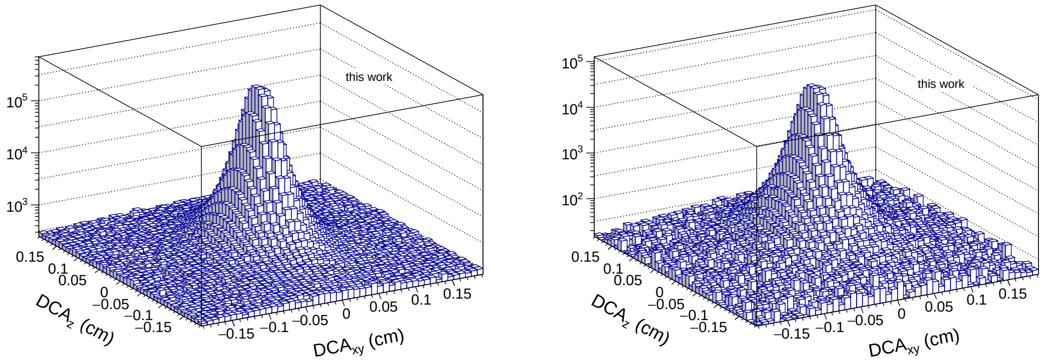

Figure 4.2: Three dimensional correlation plot (counts as a function of DCA_z and DCA_{xy}) of the deuteron and antideuteron data (*left*) and helions and antihelions (*right*). Due to different production rates counts differ by a factor of ~ 10.

reconstructed track and the position of the primary vertex, the so-called distance of the closest approach (DCA). The absolute value $|\mathrm{DCA}_z|$ along the beam axis is required to be less than 0.2 cm and in the plane perpendicular to it $|\mathrm{DCA}_{xy}|$ is set to 0.2 cm for ^{3}He and 0.1 cm for deuteron. The reason for these values is twofold: first, one observes a clear correlation between DCA_{xy} and DCA_z with most counts found at $\mathrm{DCA}_{xy} \approx \mathrm{DCA}_z \approx 0$, suggesting the primary origin of these particles (igure 4.2). The number of candidates was additionally investigated for different values of DCA cuts, shown in the right panel of Figure 4.3 for deuterons. While the number of deuteron candidates drops drastically with increasingly stricter cuts, the one of the antideuterons changes only insignificantly. This can mean that the cuts affect mostly secondary nuclei, which are not present for antideuterons but constitute a considerable fraction of deuterons. Lastly, the cuts on the $\mathrm{DCA}_{\mathrm{xy}}$ are chosen to be looser for helions to avoid rejecting too many primary candidates with respect to the sample size.

These selection criteria are summarized in Table 4.1.

4.1.2 Particle identification

To associate the reconstructed tracks with actual particles, additional steps are taken. Different detector systems are better suited for particle identification (referred to as PID) in different momentum regions. Generally, in the TPC the PID is done through measurements of the energy deposited by a particle in the detector over a given distance, i. e. by measuring its specific energy loss $\mathrm{d}E/\mathrm{d}x$. This value is then compared to the one expected for a particular particle specimen for the same transverse momentum, parameterized by the Bethe-Bloch formula. By dividing the difference between the predicted ($\langle \mathrm{d}E/\mathrm{d}x \rangle_{\mathrm{Bethe}}$) and the measured value by the corresponding resolution of the energy loss measurement ($\sigma_{\mathrm{d}E/\mathrm{d}x}$), one obtains a criterion for the PID, the number of deviations from a particle hypothesis n_σ:

$$n_\sigma = \frac{\mathrm{d}E/\mathrm{d}x - \langle \mathrm{d}E/\mathrm{d}x \rangle_{\mathrm{Bethe}}}{\sigma_{\mathrm{d}E/\mathrm{d}x}} \tag{4.1}$$

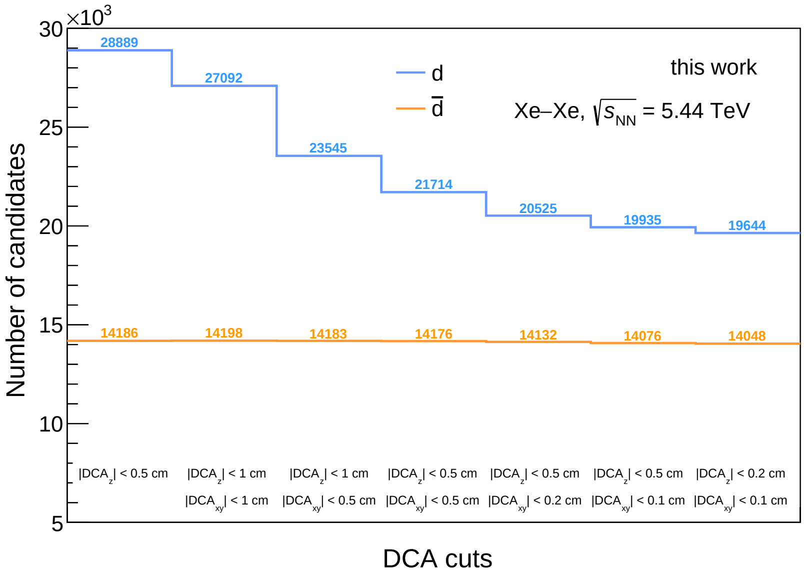

Figure 4.3: Dependence of the number of (anti)deuteron candidates on the DCA cuts.

Variable	**Selection cut**
$\lvert\eta\rvert$	< 0.8
$\lvert y\rvert$	< 0.5
$\chi^2_{\mathrm{TPC}}/\mathrm{NDF}$	< 4
$\chi^2_{\mathrm{ITS}}/n^{\mathrm{ITS}}_{\mathrm{clusters}}$	$< 36\ (3.3)^*$
$n^{\mathrm{TPC}}_{\mathrm{clusters}}$	> 70
$n^{\mathrm{TPC}}_{\mathrm{crossed}}$	> 70
$n^{\mathrm{TPC}}_{dE/dx}$	> 50
$n^{\mathrm{TPC}}_{\mathrm{crossed}}/n^{\mathrm{TPC}}_{found}$	> 0.8
$n^{\mathrm{TPC}}_{\mathrm{clusters}}/n^{\mathrm{TPC}}_{\mathrm{crossed}}$	> 0.8
$n^{\mathrm{ITS}}_{\mathrm{clusters}}$	≥ 2
$n^{\mathrm{SPD}}_{\mathrm{hitd}}$	$\geq 1^{\ddagger}$
DCA_z	< 0.2 cm
DCA_{xy}	$< 0.1\ (0.2)^{\dagger}$ cm
$n^{\mathrm{TPC}}_{\sigma}$	$\in [-2.5, 3.2]\ ([-3.0, 3.0])^{\dagger}$
$n^{\mathrm{TOF}}_{\sigma}$	$\in [-3.0, 3.5]$

Table 4.1: Summary of track and event selection criteria. * the value in parentheses is the cut used in the TPC analysis of deuteron; the other is used with TOF for deuteron and TPC for ^{3}He. ‡ The cut is only applied for deuteron. † The value in parentheses is used in the ^{3}He analysis. (See text for details; for $n^{\mathrm{TPC}}_{\sigma}$ and $n^{\mathrm{TOF}}_{\sigma}$ see the following section)

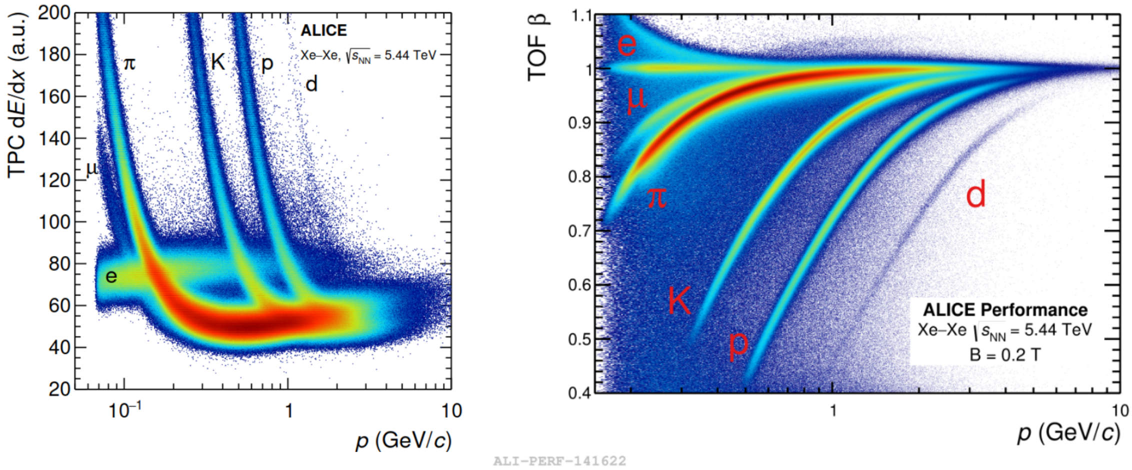

Figure 4.4: Specific energy loss (*left*) and particle velocity (*right*) as a function of the reconstructed track momentum as measured by the TPC and TOF, respectively, in Xe−Xe collisions at $\sqrt{s_{NN}} = 5.44$ TeV [25].

The flight time measured by the TOF detector can be evaluated similarly by taking the difference between the measurement and the prediction and dividing i by the time resolution of the detector. The prediction t_{TOF} is hereby calculated for a given particle mass m using the measurements of momentum p and track length L. The relationship between m and t_{TOF} can be readily expressed as:

$$m = \frac{p\,t_{\mathrm{TOF}}}{L}\sqrt{1 - \frac{L^2}{c^2 t_{\mathrm{TOF}}^2}}. \tag{4.2}$$

Figure 4.4 shows the specific energy loss measured by the TPC in Xe−Xe collisions as a function of reconstructed momentum, published in a previous analysis of light baryons and mesons [25]. Although not shown in the figure due to the low relative abundance, the ^{3}He signal is well separated over the whole p_{T} range thanks to the quadratic dependence of $\mathrm{d}E/\mathrm{d}x$ on the particle's charge number z, being 2 for ^{3}He. Therefore, the measurements of ^{3}He are done using the TPC detector over the full momentum range. For deuterons ($z = 1$), however, the TPC analysis works well in the lower momentum region before their energy loss becomes similar to that of other, more abundantly produced species. The information from the TOF then complements it for p_{T} higher than 1.15 GeV/c (see Fig 4.4, right).

4.1.3 Signal extraction using TPC

Due to statistical limitations of the collected data, the measurements in transverse momentum are grouped within appropriate intervals, forming the so-called p_{T}-bins. This approach also allows for an interval-based correction for secondary nuclei, using the shape of counts distributions in DCA_{xy} (discussed in Section 4.2.3).

The identification of ^{3}He particles is done in four transverse momentum regions, from

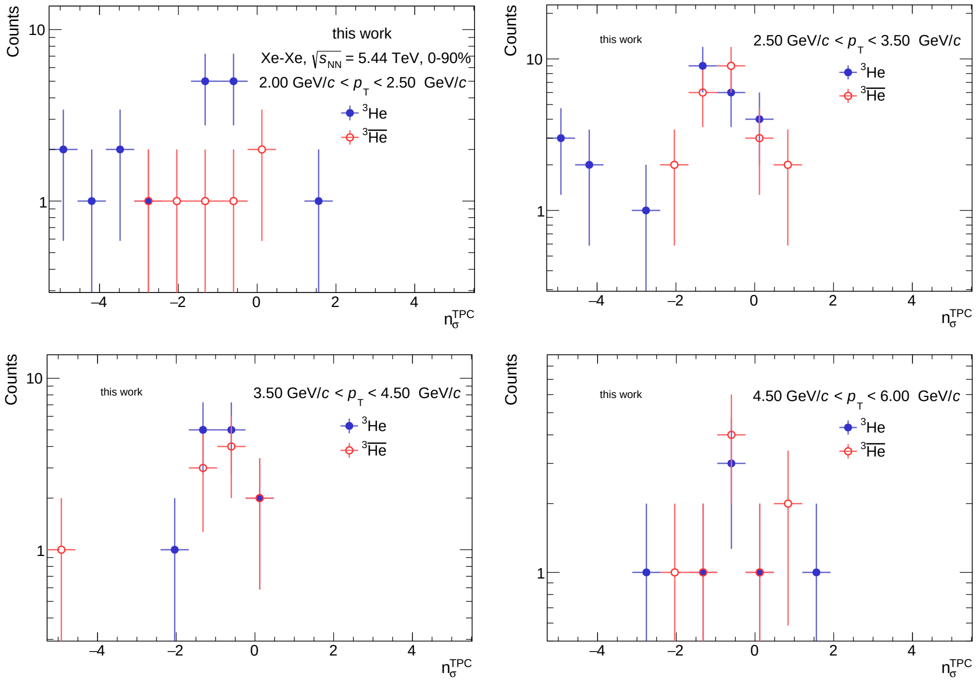

Figure 4.5: n_σ distributions of (anti)helion candidates, measured in four transverse momentum regions from 2 GeV/c to 6 GeV/c.

2.0 GeV/c to 6.0 GeV/c. The n_σ distributions of (anti)nuclei candidates that passed the selections discussed in the previous section are shown in Figure 4.5 with ^{3}He in blue and $^3\overline{\text{He}}$ in red. As mentioned before, the peak around $n_\sigma = 0$ indicates the clear ^{3}He signal signature measured in the TPC and the effectiveness of the track selection cuts. Nonetheless, a smaller rise in counts can be observed at $n_\sigma^{\text{TPC}} \sim -5$ in the first two bins, which, as one can conclude from the knowledge of Bethe-Bloch parametrizations, most likely come from triton. The same contamination is not seen in antihelions, suggesting the secondary origin of these (helion) particles. Taking into account the falling trend with n_σ the contamination is deemed insignificant in the region of signal extraction $-3 < n_\sigma^{\text{TPC}} < 3$, and the yields are obtained simply by counting the number of candidates in this region. The contamination is instead considered for the estimation of the systematic uncertainty.

The counts of (anti)deuteron candidates are shown in Figure 4.6 in green (magenta) in two transverse momentum intervals from 0.8 GeV/c to 1.0 GeV/c and from 1.0 GeV/c to 1.15 GeV/c. It is clear from the figures that the track and event selection cuts alone are not enough to guarantee the purity of a deuteron sample; the increase in counts seen at lower values of $n_\sigma^{\text{TPC}} \lesssim -3$ GeV/c, assumed to originate from secondary processes and other particle species, is likely to continue and contribute to the counts in the region of the signal extraction ($-3.0 < n_\sigma^{\text{TOF}} < 3.2$). For this reason, the background on the left is fitted with an exponential function, shown as a dashed line, and the signal is fitted with a skewed Gaussian function (thin solid line):

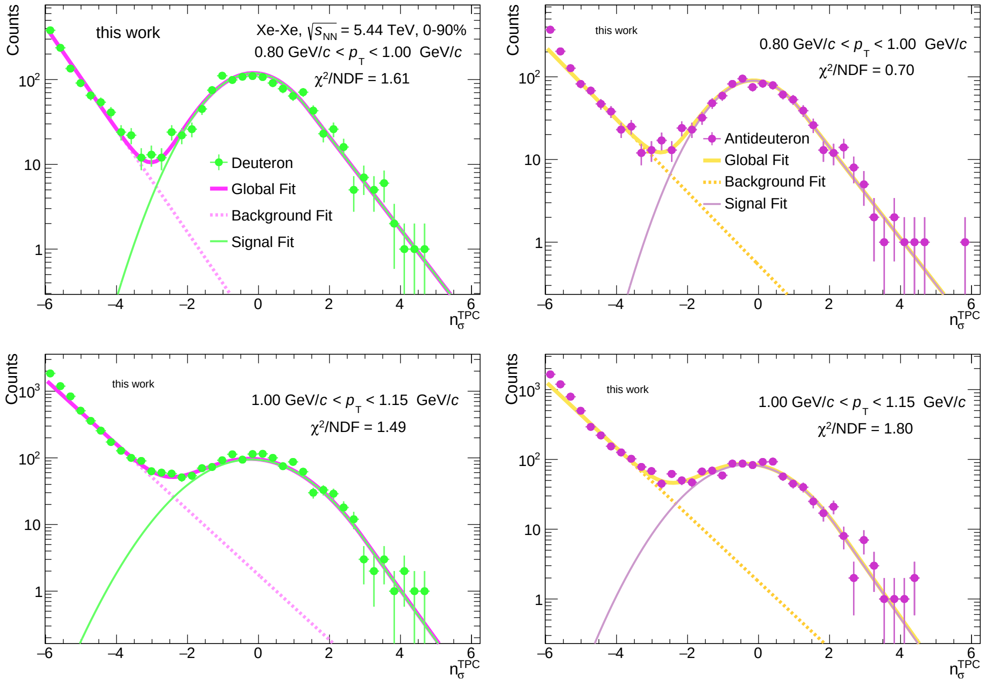

Figure 4.6: Deuterons *(left)* and antideuterons *(right)* signal extraction with the TPC in the transverse momentum region 1.0GeV/c < p_{T} < 1.15 GeV/c

$$f_{\text{signal}}(n_\sigma) = A \begin{cases} e^{-\frac{1}{2}\left(\frac{n_\sigma-\mu}{\sigma}\right)^2} & n_\sigma < \mu + \tau\sigma \\ e^{-\left(\frac{n_\sigma-\mu}{\sigma}-\frac{\tau}{2}\right)\tau} & n_\sigma \geqslant \mu + \tau\sigma \end{cases} \tag{4.3}$$

Where A, μ, σ, and τ are free parameters corresponding to the normalization constant, the centroid, the width of the Gaussian, and the number of σs from the mean, at which the function becomes exponential, respectively. This form was chosen over a normal Gaussian to account for the asymmetric tail on the right, present also in the case of the rapidly falling background contamination in the lowest p_{T}-bin. Consequently, the interval for the signal extraction is chosen to be asymmetric: the signal fit is integrated in $[-2.5 + \mu, 3.2 + \mu]$ using the fit estimate for μ. Its lower bound is increased with respect to the usual -3.0 to limit the number of contributing secondaries, and the upper bound is extended to allow for the asymmetry in the signal[4]. The integral of the fitted function is subsequently divided by the bin width to correct for the discretization of the histogram.

4.1.4 Signal extraction using TOF

The TOF detector provides the basis for the deuteron analysis, with a clear signal spanning from 1.15 GeV/c to 6 GeV/c.

In the energy loss spectrum (Figure 4.4), deuterons are close to protons and other much

---

[4] Variations of the limits are included in the systematic uncertainty; see Section 4.3

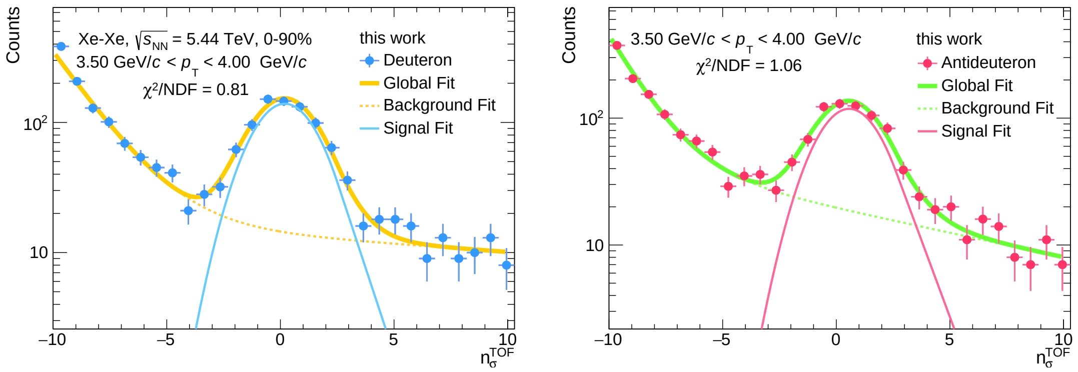

Figure 4.7: Deuterons (*left*) and antideuterons (*right*) signal extraction with the TOF in the transverse momentum interval 3.50 GeV/c < p_T < 4.00 GeV/c

more abundantly produced species. This results in a considerable background contribution in n_σ^{TOF} distributions of deuterons, being the lowest at lower momentum values (most significant signal separation between d and p in Fig. 4.4) and getting dominant with higher momentum, where the velocities of all particles converge to 1. To account for this background, two exponential functions are used together with a skewed Gaussian (Eq. 4.3) to fit the data. One of thirteen bins is shown in Figure 4.7, while all of them can be found in Appendix, Figures 7.3 7.4. For the yield extraction, the signal fit function is integrated in the interval $[-3.0 + \mu, 3.5 + \mu]$ with the mean μ estimated from the fit and then divided by the bin width. The interval is asymmetric to account for the exponential tail on the right of the signal.

4.2 Corrections to the raw spectra

The previous sections described the signal extraction methodology for (anti)d and (anti)^{3}He. To obtain the raw yields $\mathrm{d}^2N/(\mathrm{d}p_T\mathrm{d}y)$, one divides the counts by the size of the rapidity window ($\Delta y = 1$) and the width of the corresponding transverse momentum intervals. The results are shown in Figure 4.8.

Several peculiarities can be observed in these histograms. First, the slight discrepancies in the numbers of particles and antiparticles are visible over the whole transverse momentum distributions of deuteron and ^{3}He (anti)nuclei spectra. Furthermore, the deuteron distributions have a pronounced discontinuity at 1.15 GeV/c, where the transition between the TPC and TOF as the primary PID detector occurs. Both of these features can be explained through different reconstruction efficiencies of the detectors for particles and antiparticles, which are momentum-dependent, as addressed in the next section. Another interesting feature of the raw spectra concerns the lowest momentum region ($p_T \lesssim 1.5$ GeV/c), where the number of particles is larger than that of antiparticles. This effect is due to a higher probability of particle production in reactions of primary collision products with the constituents of the detectors or the beam pipe (spallation processes), which can be (at least partially) qualitatively understood by the final states of these

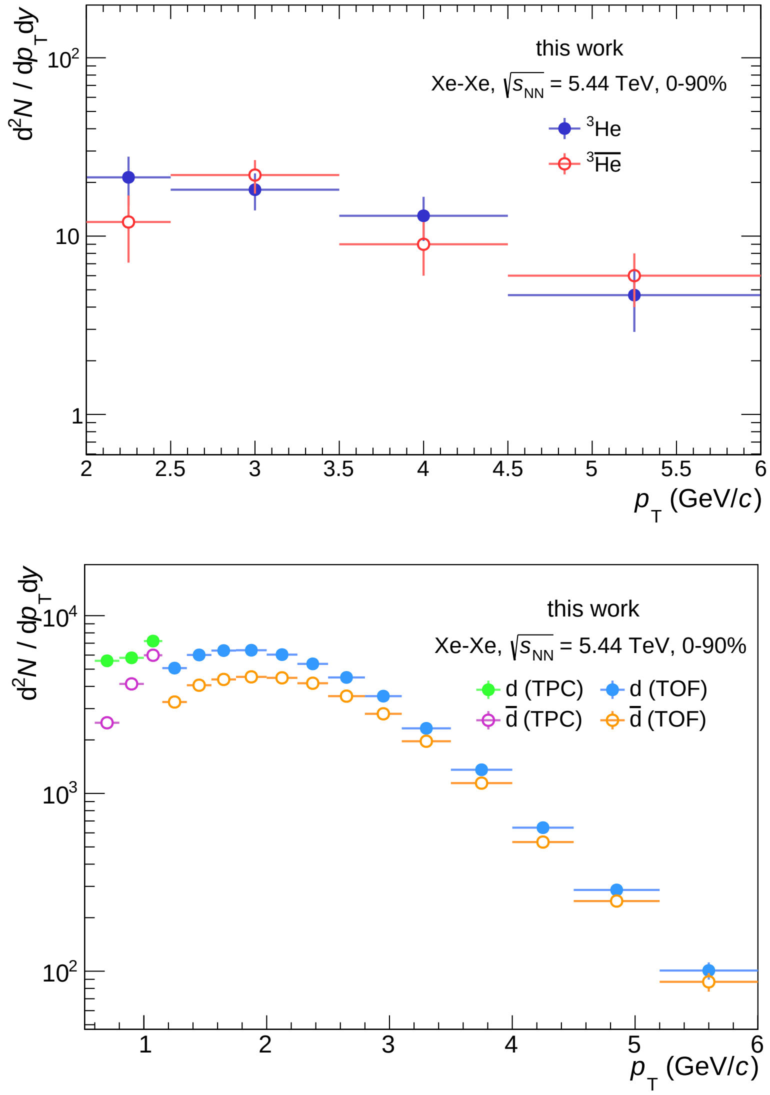

Figure 4.8: Raw yields of (anti)^{3}He (*top*) and (anti)deuteron (*bottom*).

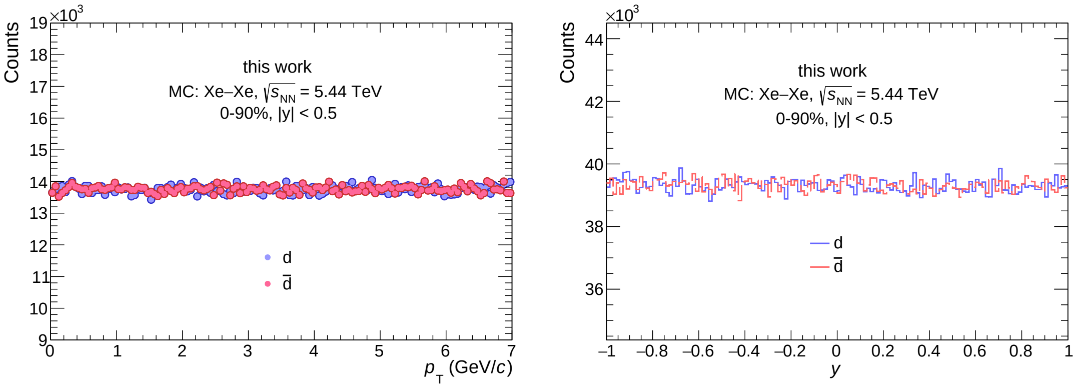

Figure 4.9: Transverse momentum distributions (*left*) and rapidity distribution (*right*) of the generated deuteron particles from a dedicated Monte Carlo simulation.

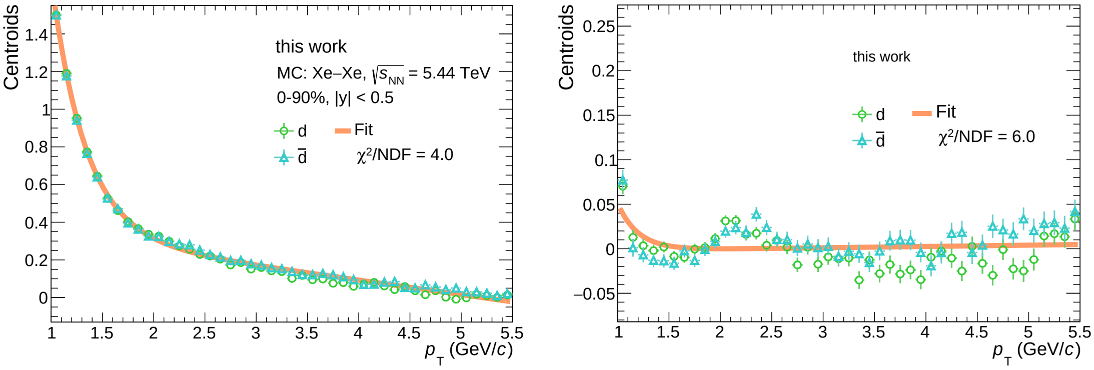

Figure 4.10: Centroids from the fits of the reconstructed TOF signal for (anti)deuterons produced in a dedicated Monte Carlo simulation, before and after the recentering.

particles having a larger available phase space (the phase space decreases with higher momentum thus decreasing the total reaction rates, according to the Fermi's golden rule). As shown in Section 4.2.3, additional measures are taken to correct for this secondary contribution.

4.2.1 Detector efficiency and acceptance

Not every particle emitted in a collision is measured, and not every detected particle is measured equally well. The detector's geometry determines its acceptance with its coverage around the experiment. Detector efficiency depends on the interaction cross-section of a specific particle with the material inside the detector at a given energy, as well as the probability of the detector producing a signal upon registering the particle and other processes in the reconstruction chain. To estimate the combined influence of these factors on the measurement, a detailed model of the complete detector system with correct dimensions and material was produced, and the propagation of particles was simulated using Monte Carlo algorithms.

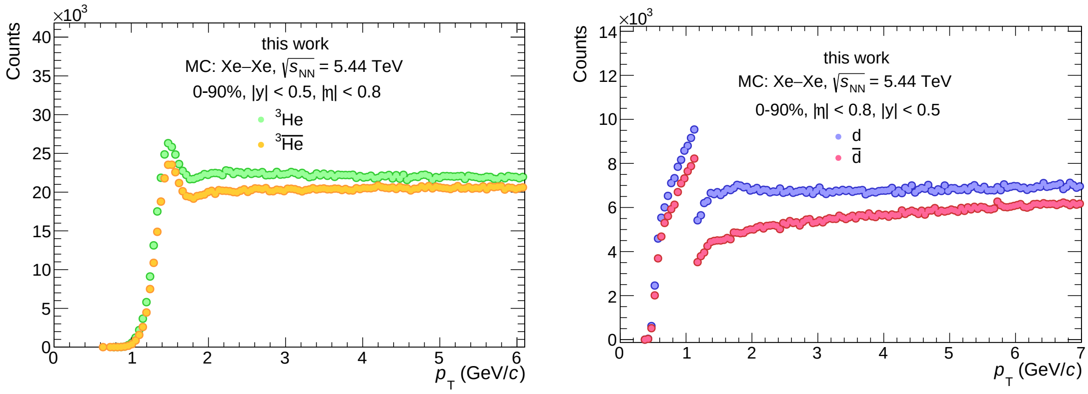

Figure 4.11: Reconstructed momentum spectra of (anti)^{3}He (*left*) and (anti)deuterons (*right*) (Monte

In particular, the particle propagation in the simulation used in this thesis was performed with the GEANT4 package [27], while HIJING [28] serves as an event generator. (Anti)nuclei are injected in the simulations used for this study, on top of the underlying events. The injected (anti)nuclei are generated with a flat transverse momentum and a flat rapidity distributions, as shown in Figure 4.9[5]. Similar results are obtained for ^{3}He (see Figure 7.5 in Appendix).

To match the conditions of the data, the same selection is applied as described in Section 4.1.1, including the geometric cut on pseudorapidity (acceptance of the detector) and the same PID restrictions on n_σ^{TPC} and n_σ^{TOF}. The latter is done after correcting the n_σ distributions for a possible miscalibration of the signal: the reconstructed counts were plotted in narrow intervals (100 MeV/c wide for TOF) against their n_σ values and fitted with a skewed Gaussian function[6]. The mean values μ of the fits are then plotted for each p_T-bin, and the mean for particles and antiparticles is then fitted, in the case of the TOF signal, with a sum of linear and exponential functions (Figure 4.10, left). This procedure is then repeated after shifting the n_σ^{TOF} value for every track with the latter function depending on the track-p_T. As shown in the right panel of Figure 4.10, the resulting signal distributions are centered at zero. Such correction is unnecessary for the TPC because no signal shift is observed. The resulting spectra for both particles are given in Figure 4.11.

Both particles have a vanishing detection efficiency at low momenta (helions: $p_\text{T} \lesssim 1.0$ GeV/c, deuterons: $p_\text{T} \lesssim 0.5$ GeV/c[7]) while the efficiency rises steeply and saturates for

---

[5] The only cut applied to the generated particles ensures that they (like the data) belong to midrapidity.

[6] No background from other species is present as the MC data collection is done with a specific particle code (PDGcode). Also, only "primary" particles are considered, as only those are generated with a flat distribution (Figure 4.9).

[7] The "momentum-threshold" for detection is higher for helions, which experience a higher energy loss at low momenta, by being more massive than deuterons (see the Bethe-Bloch formula); also they carry twice as much charge. These two facts result in a smaller curvature radius r of the particle trajectory in the magnetic field B according to a simple relation $p = qBr$, where p is the momentum and q the total electric charge of the particle. The particle then does not leave the innermost parts of the detector and thus does not reach the TPC.

higher values of p_{T}. Antiparticles are expected to have a lower detection rate due to the likely absorption and annihilation processes with the matter of the detector material. The GEANT4 results confirm this trend for both particles. One also recognizes the discontinuity in (anti)deuteron detection efficiency, coinciding with the one seen in the data: the material of the TRD prevents some particles from reaching the TOF detector. The small peak in reconstructed (anti)helions is a known feature of the TPC measurements [22] at $p_{\mathrm{T}} < 1$ GeV/c. The low-field configuration of 0.2 T employed in Xe$-$Xe collisions leads to a shift of this peak to higher momentum values.

The product of acceptance α and efficiency ε of the detector is obtained as the ratio of the reconstructed tracks to the generated particles for each p_{T} bin:

$$\alpha \times \varepsilon = \frac{N^{(\mathrm{rec})}_{|y|<0.5, |\eta|<0.8}}{N^{(\mathrm{gen})}_{|y|<0.5}} \tag{4.4}$$

To use the resulting fine-binned histograms[8] for the spectrum correction, a weighted average is built from its values for each bin of the particle spectra, with weights provided by a Levy-Tsallis function describing the deuteron production in p$-$Pb collisions at $\sqrt{s_{NN}} = 8.162$ TeV [12] and an m_{T}-exponential function of ^{3}He in the same system, for deuteron and ^{3}He, respectively. The reweighting is done to correct the artificially flat distributions of generated particles. The results of the procedure can be seen in Figure 4.12, repeating the trends discussed for the reconstructed spectra. In particular, the higher efficiency of ^{3}He is a consequence of using the TPC detector for PID, while (anti)deuterons travel through the entire length of the TRD detector to be registered by the TOF.

4.2.2 Secondary nuclei in spallation processes

As mentioned at the beginning of Section 4.2, a considerable fraction of secondary nuclei remains unfiltered in the lowest momentum bins, while the number of antinuclei is unaffected. Assuming no statistical fluctuation, the particle-antiparticle discrepancy in these bins can be indicative of such secondary nuclei. This hypothesis is supported by comparing the DCA$_{xy}$ evolution with transverse momentum for particles and antiparticles after the complete event, track, and PID selection[9] (Figure 4.13). While most of the antideuteron DCA$_{xy}$ values are contained inside a narrow band around zero, deuteron has an almost homogeneous distribution to the right and left of the center for $p_{\mathrm{T}} \lesssim 1.2$ GeV/c. It is, therefore, reasonable to suggest that this constant contribution is also present in the central region used for signal extraction $[-0.1\ \mathrm{cm}, 0.1\ \mathrm{cm}]$. It is known, in fact, that the secondary nuclei, while having a flat distribution over most of the DCA$_{xy}$ range, also have a peak at zero due to the wrongly assigned clusters of the ITS detector. To quantify this effect, one again uses simulated data from Monte Carlo. This time separation of simulated particles by their origin of production (primary, secondary from the material, and, if applicable, secondary from decays), available from simulation, allows one to make

---

[8] Figure 7.6 in Appendix.

[9] Including the cut on DCA along the beam axis.

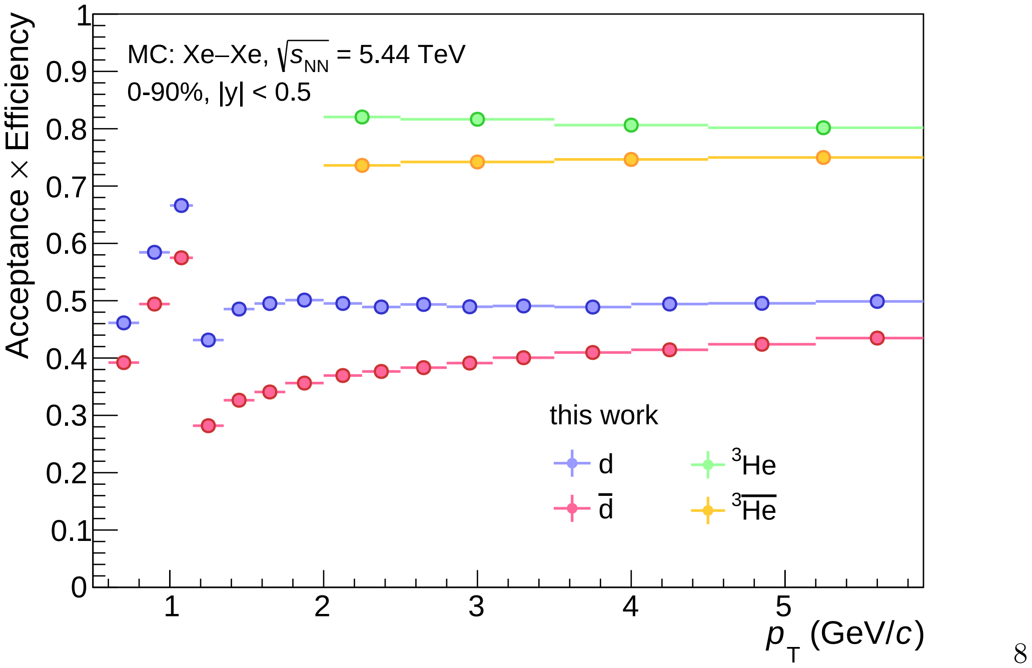

Figure 4.12: Acceptance × efficiency of the used detectors for (anti)^{3}He and (anti)deuteron.

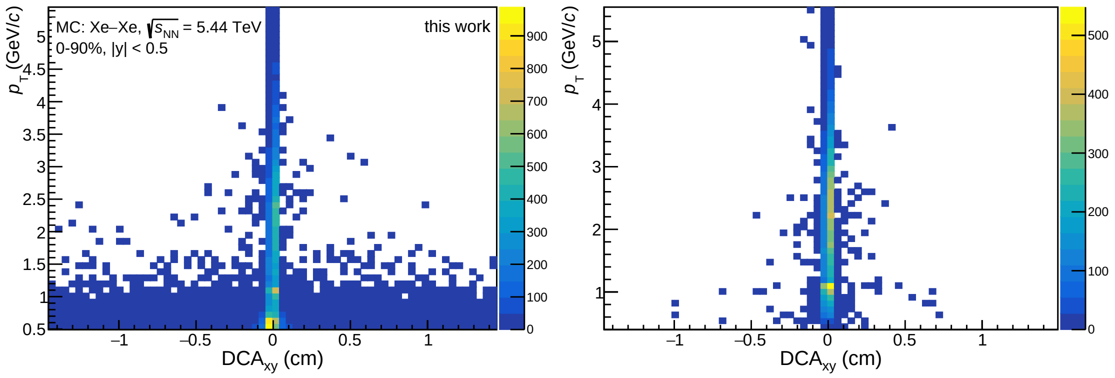

Figure 4.13: Distributions of DCA$_{xy}$ in transverse momentum after applying all the cuts for deuteron (*left*) and antideuteron (*right*).

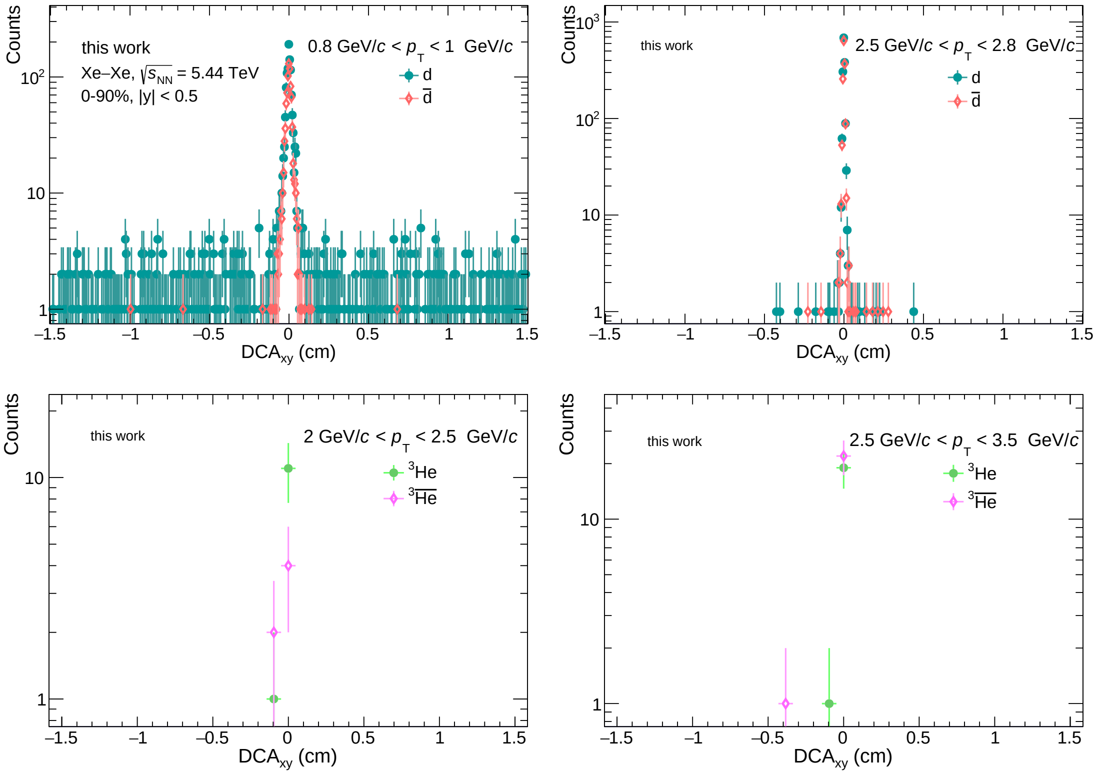

Figure 4.14: DCA$_{xy}$ distributions of deuteron (teal circles) and antideuteron (pink diamonds) candidates in the upper panel and of helions (green circles) and antihelion (light pink diamonds) in the lower panel in two p_T intervals.

predictions about the shapes of their DCA$_{xy}$ distributions. The shapes then can be compared to the measured ones and thus used to estimate and subtract the remaining secondary contribution. To this end, the DCA$_{xy}$ distributions of the data are first plotted in the same momentum intervals used in the PID part of the analysis. Two histograms are shown in Figure 4.14 for (anti)^{3}He and (anti)deuteron; the rest can be found in Appendix. Deuterons have a visible background in the first bins (an example is given on the left of the top panel of Figure 4.14), while helium has almost no counts to either side of the center (for $p_T > 2$ GeV/c, see the bottom pannel of Figure 4.14). This does not change even if the selection on DCA$_z$ is loosened to 0.5 cm. With no information outside of the relevant region $|\text{DCA}_{xy}| < 0.2$ cm, no reliable estimate of secondary contribution using the template method is possible, and so it is neglected and only considered as a part of the systematic uncertainty (Section 4.3). The following discussion focuses on deuterons.

Monte Carlo templates (i. e. simulated DCA$_{xy}$ distributions) have to fulfill the same selection criteria as the data. Due to the lack of primary particles in MC productions for the Xe−Xe system[10], a data-driven approach is taken for the primaries: antideuterons are used to model the fraction of primary nuclei since antinuclei are almost always produced

---

[10] The type of production used for fitting DCA$_{xy}$ templates to data (general purpose Monte Carlo) is not the same as the one used for efficiency estimation.

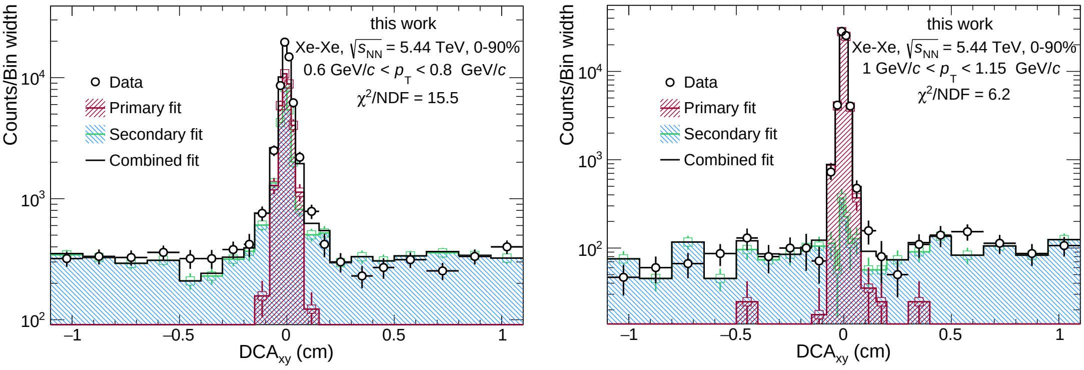

Figure 4.15: Monte Carlo template fits of deuterons in two transverse momentum intervals.

in the primary vertex. The templates are fitted to the data, requiring each of them to be between 0 and 1 with respect to the total deuteron counts. The fitting is done in the region where the production of secondary particles is expected to be relevant: from 0.6 GeV/c to 1.8 GeV/c, after which this contribution is neglected. Figure 4.15 depicts some of the results. The fits seem reasonable in the central DCA$_{xy}$ region but less so outside of it, which is also reflected by their relatively high χ^2/NDF values. The fits are carried out using the TFractionFitter method implemented in ROOT. The content of each bin is varied individually, taking the statistical uncertainties into account for the normalization. A somewhat better convergence is achieved by using more narrow bins; this allows for a better description of a steep increase in the fraction with $p_{\rm T}$. The latter is illustrated in Figure 4.16, in which the primary fractions obtained using the default $p_{\rm T}$-bins of the analysis are drawn as full, light-grey circles, and the ones from finer bins as empty blue circles.

To minimize statistical fluctuations of the templates, the discrete values of primary fractions (narrow bins) are fitted with different functions, also shown in Figure 4.16, together with their χ^2NDF values. The functions differ mainly in the low-momentum region ($p_{\rm T} \lesssim 0.65$ GeV/c), where the primary fraction is vanishing and, therefore, is harder to estimate. The most appropriate description is apparently given by the simple form $f_{\rm primary}(p_{\rm T}) = 1 - a\,e^{-b\,p_{\rm T}}$, which is then used to correct the raw yield: the integrals of the function in the transverse momentum intervals of the analysis are divided by the corresponding bin widths, and the yields are multiplied by the resulting factor. The other shapes are utilized as an estimate of the systematic uncertainty, see Section 4.3.

4.2.3 Secondary nuclei from weak decay

Another possible source of secondary (anti)nuclei production is weak decay. The only significant process for helions (antihelions) is (anti)hypertriton decay, ${}^{3}_{\Lambda}\mathrm{H} \to {}^{3}\mathrm{He} + \pi^-$ (${}^{3}_{\Lambda}\overline{\mathrm{H}} \to {}^{3}\overline{\mathrm{He}} + \pi^+$). The corresponding contribution in the $p_{\rm T}$-spectra can be estimated as

$$f_{\text{feed-down}}\ (p_{\rm T}) = \frac{\varepsilon_{\rm decay}\ (p_{\rm T})}{\varepsilon_{\rm primary}\ (p_{\rm T})} \cdot \mathrm{BR} \cdot \frac{(\mathrm{d}N/\mathrm{d}y)_{{}^{3}_{\Lambda}\mathrm{H}}}{(\mathrm{d}N/\mathrm{d}y)_{{}^{3}\mathrm{He}}} \tag{4.5}$$

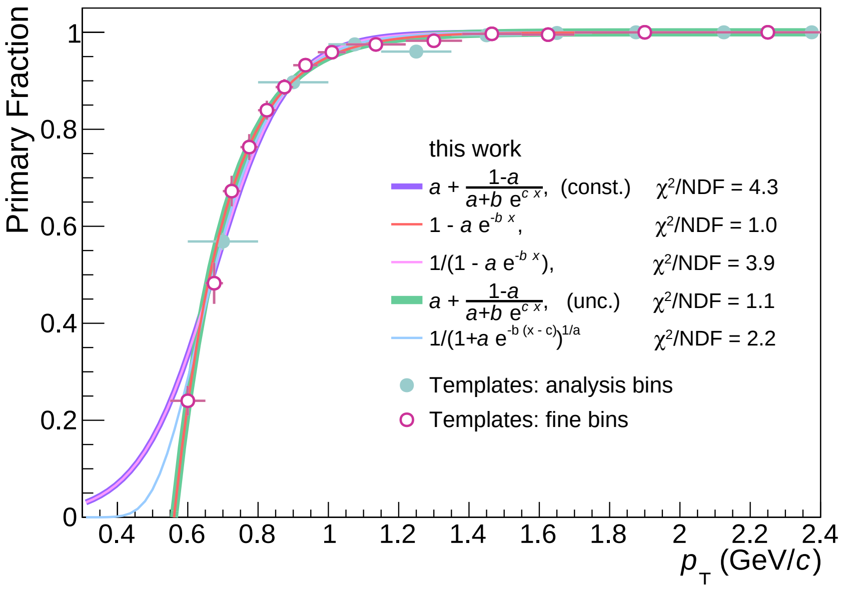

Figure 4.16: Fraction of primary deuterons calculated using the template fit method in the bins of the analysis (full grey circles) and in more narrow bins (empty blue circles). Also the fit functions are given.

Where $\varepsilon_{\text{decay}}$ and $\varepsilon_{\text{primary}}$ are reconstruction efficiencies of secondary (from decay) and primary helions, BR is the branching ratio of this reaction (taken to be 25% [29]), and the last term denotes the ratio of p_T-integrated yields of the two particles.

The efficiency of reconstructed particles from weak decay is obtained using a dedicated MC production; $\varepsilon_{\text{decay}}/\varepsilon_{\text{primary}}$ is shown in Figure 4.17 in narrow bins in the left panel and rebinned to match the helion bins in the right. As usual, the values are hereby reweighted using the m_T-exponential function to account for the shape of the spectra.

The measurements of all available hypertriton yields carried out by ALICE (divided by

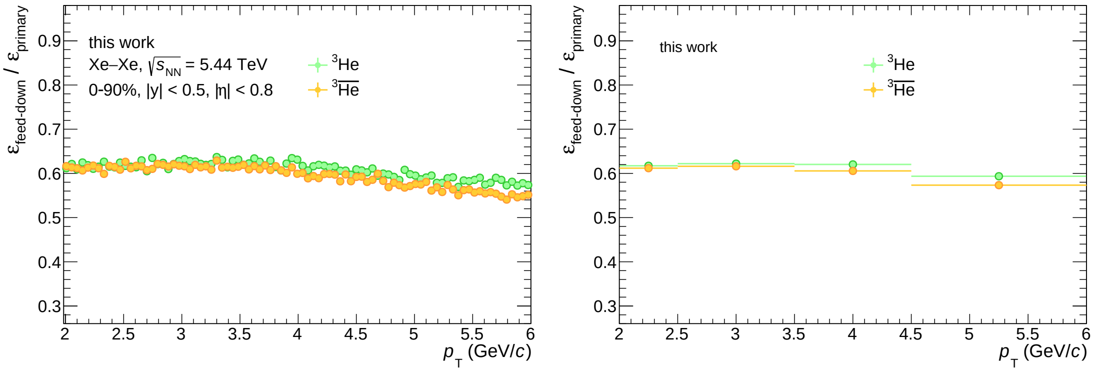

Figure 4.17: Monte Carlo analysis: ratio of the reconstruction efficiency of helion particles from weak decay to one of the primary helions in narrow and analysis bins of transverse momentum.

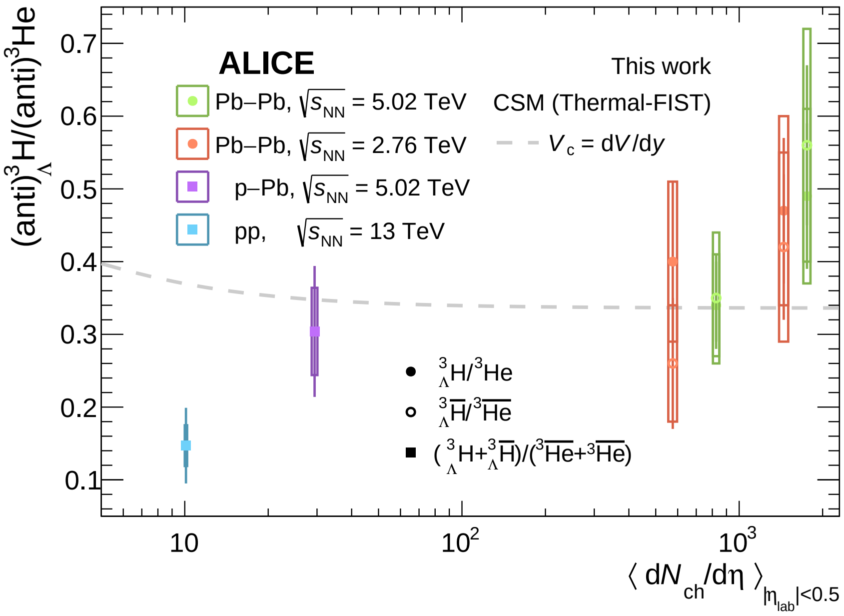

Figure 4.18: ALICE measurements of the (anti)hypertrtion-to-(anti)helion ratios as a function of charged particle multiplicity in different systems and energies. The dashed line shows a prediction of the vanilla canonical statistical model for the kinetic freeze-out temperature of 155 MeV. Statistical uncertainties are represented by vertical lines, systematic ones as boxes.

the corresponding helium yields) are shown in Figure 4.18 in a half-logarithmic scale. They are used for a linear extrapolation to the Xe−Xe charged particle multiplicity value, $\langle \mathrm{d}N_{\mathrm{ch}}/\mathrm{d}\eta\rangle_{|\eta_{\mathrm{lab}}|<0.5} = 331.3$. The resulting value is 0.250 ± 0.050 (0.241 ± 0.050) for ^{3}He/$^3_\Lambda$H ($^3\overline{\mathrm{He}}/^3_\Lambda\overline{\mathrm{H}}$), where the statistical uncertainty is estimated by evaluating the fit at $\langle \mathrm{d}N_{\mathrm{ch}}/\mathrm{d}y\rangle = 331.3$, with its free parameters increased and decreased by their respective statistical errors (the realted systematic uncertainty estimate is adressed in Section 4.3).

The resulting correction on the yield is shown in Figure 4.19 for helions. It is considered negligible for (anti)deuterons in accordance with previous studies [12].

4.2.4 Energy loss at low momentum

Looking back at the response curve of the TPC detector (Figure 4.4) or the Bethe-Block formula for its description, one recognizes the steep rise in specific energy deposition of particles at low momentum. In practice, it means that low-energy particles are more likely to lose a considerable fraction of their energy before being detected; their measured momentum is therefore lower than it was at production. To quantify this effect, one makes use of the previously discussed Monte Carlo simulation: the difference between the reconstructed momentum of a track $p_{\mathrm{T}}^{\mathrm{gen}}$ and the initial momentum of the generated particle $p_{\mathrm{T}}^{\mathrm{true}}$ (corresponding to the same track) is plotted as a function of the reconstructed transverse momentum (Figure 4.20). If the two quantities demonstrate a systematic discrepancy (peak in counts at $p_{\mathrm{T}}^{\mathrm{gen}} - p_{\mathrm{T}}^{\mathrm{true}} \neq 0$), then the distribution is fitted with a $p_{\mathrm{T}}^{\mathrm{rec}}$-dependent function representing the energy loss correction. The fit can be used to correct the measured momentum values on a track-by-track basis, after which the

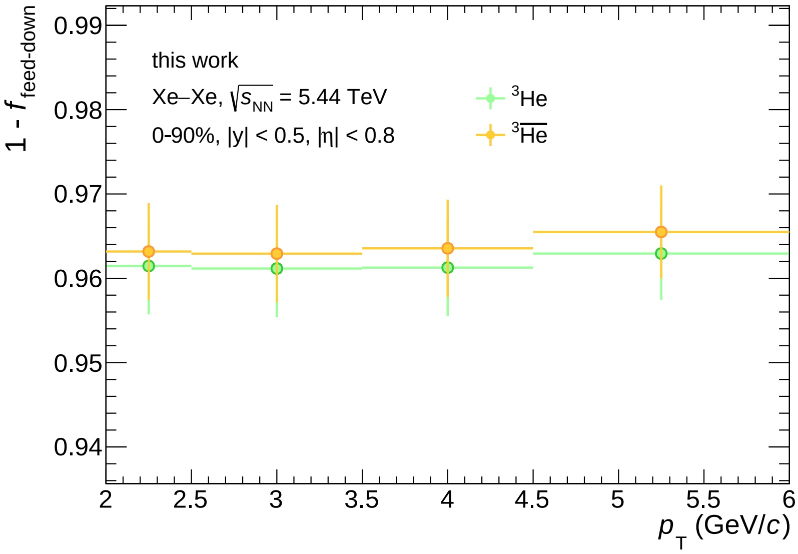

Figure 4.19: Primary fraction of (anti)helions, after subtracting the (anti)nuclei from feed-down. See text for the calculation of statistical uncertainty.

PID and the other steps of the analysis are repeated. In the present case, however, no obvious deviation from zero is observed, and thus no correction is applied. A splitting of the distribution is seen for ^{3}He, where a deviation usually occurred in previous analyses [11]. The (anti)helion is studied for the values of transverse momentum greater than 2 GeV/c, so no correction is applied since no systematic energy loss is obesrved in this region.

4.3 Systematic uncertainties

The steps taken to analyze the data inevitably introduce systematic uncertainties as a result of incomplete knowledge of some indirectly involved quantities (e. g. hadronic

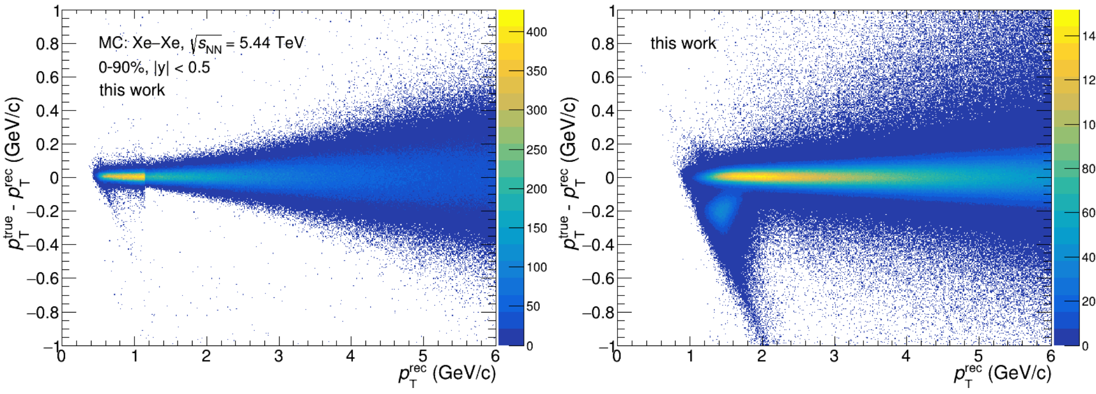

Figure 4.20: Difference between the reconstructed and the ”true” momentum as a function of the reconstructed, obtained from Monte Carlo simulation for (anti)deuterons *(left)* and (anti)^{3}He *(right)*.

particle	^{3}He ($^3\overline{\text{He}}$)	
p_T range	2.0 – 2.5 GeV/c	4.5 – 6.0 GeV/c
Source of uncertainty		
Track selection	negl.	negl.
ITS-TPC matching	5.3 % (5.3 %)	4.2 % (4.2 %)
Secondaries, material	5.7 %	negl.
Secondaries, feed-down	2.3 % (2.3 %)	2.2 % (2.2 %)
Triton contamination	2.5 %	negl.
Hadronic cross-section	1.0 % (3.0 %)	1.0 % (3.0 %)
Material Budget	0.3 % (0.2 %)	0.2 % (0.3 %)
Total	8.6 % (6.5 %)	4.8 % (5.6 %)

Table 4.2: Systematic uncertainties of helions (antihelions) in the first and the last transverse momentum bins.

cross-section, detector material) but also due to the remaining discrepancies between data and simulation (e. g. primary fraction, tracking). The following sources of uncertainties are considered in the next sections:

- Track selection (reconstruction)
- Signal extraction (PID)
- ITS-TPC matching efficiency
- TPC-TOF matching efficiency
- Correction for secondaries from material
- Correction for secondaries from decay
- Triton contamination
- Hadronic cross-section
- Material budget

The summary of the results is given in Tables 4.2 and 4.3 and Figures 4.21 and 4.22. The individual contributions are summed in quadrature to obtain the total systematic uncertainties.

Track selection

The uncertainty associated with the cuts on reconstructed tracks (Section 4.1.1) is calculated by varying these criteria 50 times in predefined ranges with a uniform distribution. Since some of the cuts are highly correlated (for example, the number of TPC clusters, crossed rows, and clusters used for PID), they are varied simultaneously. In the case of (anti)deuterons, each set of cuts is varied separately from the others, which are kept at

particle	$\mathrm{d}\,(\overline{\mathrm{d}})$	
p_{T} range	0.6 – 0.8 GeV/c	5.2 – 6.0 GeV/c
Source of uncertainty		
Track selection	7.6 % (2.2 %)	1.2 % (0.9 %)
Signal extraction	5.5 % (4.0 %)	0.5 % (0.5 %)
ITS-TPC matching	3.2%(3.2 %)	3.5%(3.5%)
TPC-TOF matching	negl.	6.2%(7.2%)
Secondaries, material	4.2 %	negl.
Hadronic cross-section	1.0%(3.0%)	1.0 % (1.0 %)
Material Budget	1.0%(0.3%)	1.0 % (1.0 %)
Total	10.9%(5.7%)	7.4%(8.2%)

Table 4.3: Systematic uncertainties of helions (antihelions) in the first and the last transverse momentum bins.

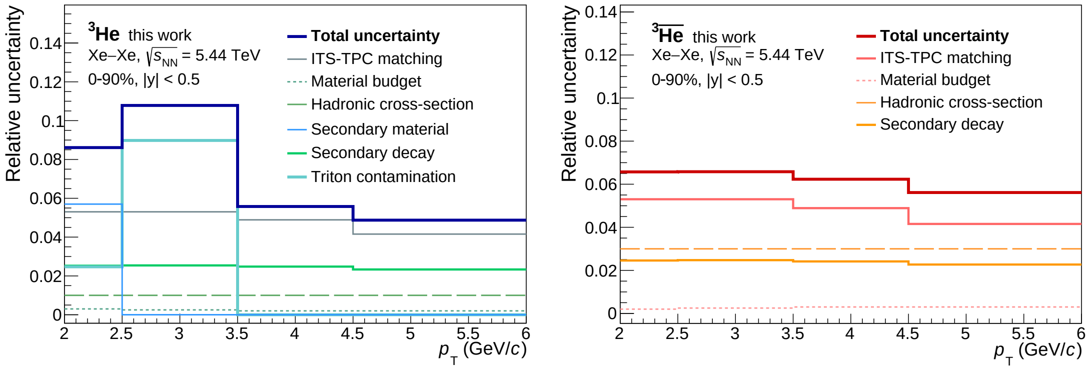

Figure 4.21: Summary of the contributions to the systematic uncertainty of (anti)helions.

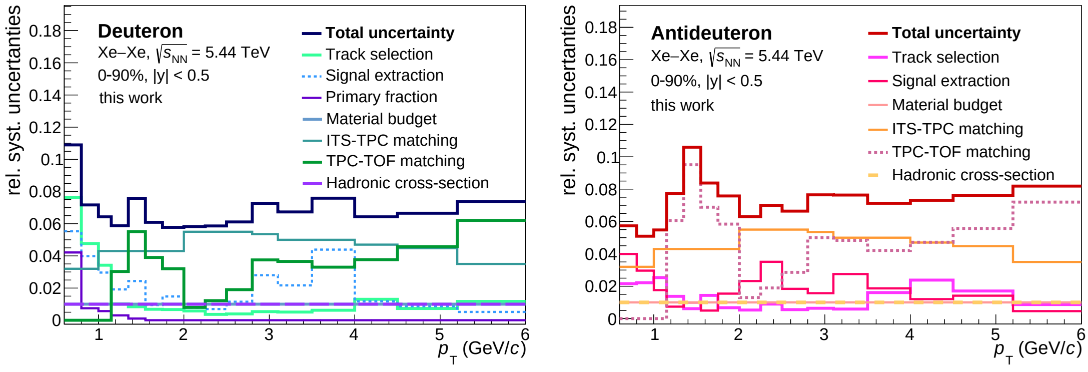

Figure 4.22: Summary of the contributions to the systematic uncertainty of (anti)deuteron.

Variable	Default value	Variation
$\lvert\mathrm{DCA}_z\rvert$	0.2	$(0.1, 0.7)$
$\lvert\mathrm{DCA}_{xy}\rvert$	0.1(0.2)	$(0.1, \lvert\mathrm{DCA}_{xy}\rvert/2)$
χ^2/NDF	4.0	$(3.0, 5.0)$
$\chi^2_{\mathrm{ITS}}/n^{\mathrm{ITS}}_{\mathrm{clusters}}$	36	$(20, 45)$
$\chi^2_{\mathrm{ITS}}/n^{\mathrm{ITS}}_{\mathrm{clusters}}{}^{\dagger}$	3.3	$(2.5, 8)$
$n^{\mathrm{TPC}}_{\mathrm{clusters}}$	70	$(65, 100)$
$n^{\mathrm{TPC}}_{\mathrm{crossed}}$	70	$n^{\mathrm{TPC}}_{\mathrm{clusters}}$
$n^{\mathrm{TPC}}_{\mathrm{d}E/\mathrm{d}x}$	50	$n^{\mathrm{TPC}}_{\mathrm{clusters}} - 20$
$n^{\mathrm{TPC}}_{\mathrm{crossed}}/n^{\mathrm{TPC}}_{\mathrm{found}}$	0.8	$(0.7, 0.9)$

Table 4.4: Track variables with their default values (Section 4.1.1) and ranges for uniform, random variations. Correlated variables are varied together. (†) The cut of 3.3 and the range (2.5, 8) applies for the study of (anti)deuterons with the TPC, for 0.6 GeV/c < p_{T} < 1.15 GeV/c.

their default values. Track variables and their variations are summarized in Table 4.4.

For each variation, the data is refilled anew using two-dimensional histograms (transverse momentum versus n_σ), which are then used to rebuild the distributions of n_σ in the p_{T} intervals of the analyses. To prevent failed fits from contributing to the final uncertainty, the fitting parameters are readjusted until all χ^2/NDF values are below 4. For (anti)deuterons, all fits are then performed again, and the yields are extracted by integrating the signal function, whereas for (anti)helions the counts were resumed in the relevant region. Also the simulated data is refilled to recalculate the new efficiency, consistent with the changed reconstruction conditions. As was pointed out in the previous sections, the fraction of primary deuterons is highly dependent on the DCA and χ^2_{ITS} cuts. For this reason the primary fraction correction is also recalculated for the variations of these cuts, in the same way as in Section 4.2.3; otherwise, the default one is used. After all the corrections, the yield distributions are plotted for each p_{T}-bin, and the uncertainty is determined as the standard deviation of the counts divided by the mean. One such distribution for each particle and antiparticle is shown in Figure 4.23.

The so-called Barlow test is used for helium particles to estimate the statistical influence in the calculated tracking systematics. The criteria C for accepting the uncertainty as systematic can be expressed as

$$C = \frac{x_{\mathrm{def}} - x_{\mathrm{var}}}{\sqrt{\sigma^2_{\mathrm{def}} - \sigma^2_{\mathrm{var}}}}$$

Where x_{def} and x_{var} are some default quantity and one obtained through some variation, respectively, and σ_{def} and σ_{var} are the corresponding statistical uncertainties. The statistical uncertainty is considered dominant if the absolute value of C is less than one, in which case the variations are discarded. Figure 4.24 shows the values of the Barlow

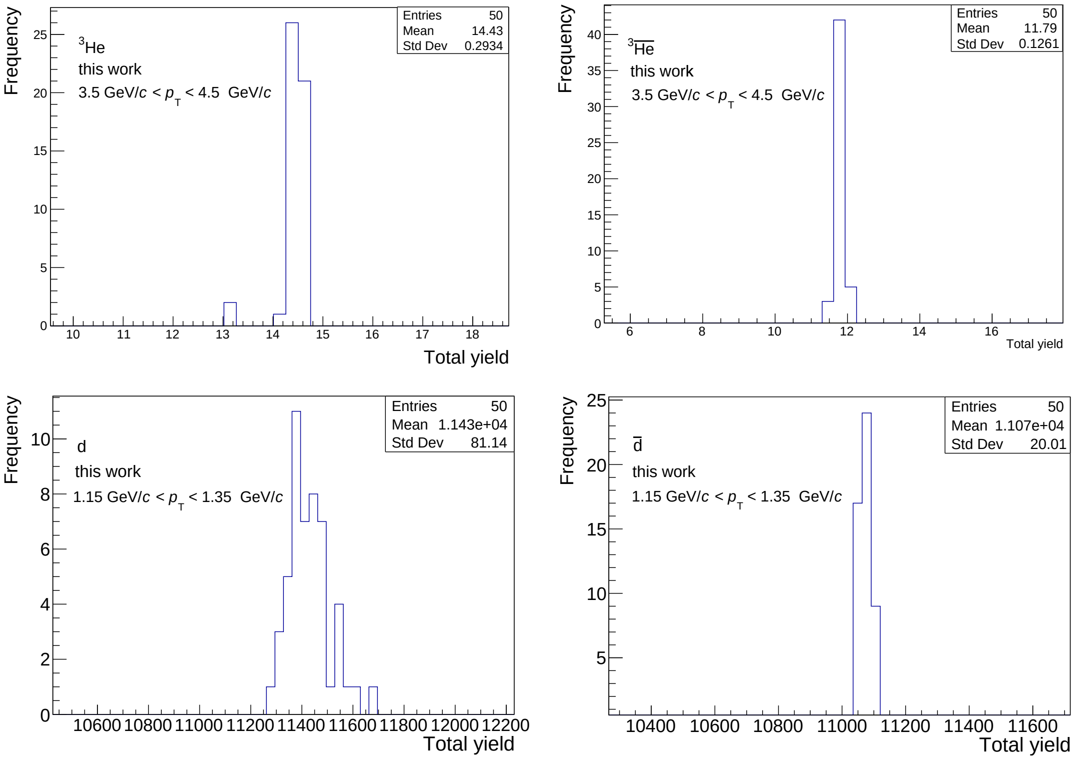

Figure 4.23: Frequency of occurrence per 50 variations for each value of counts in a p_{T} interval, obtained by varying all track selection cuts (helion and antihelion, top panel) and the cut on χ^2_{ITS}/NDF (deuteron and antideuteron, bottom panel).

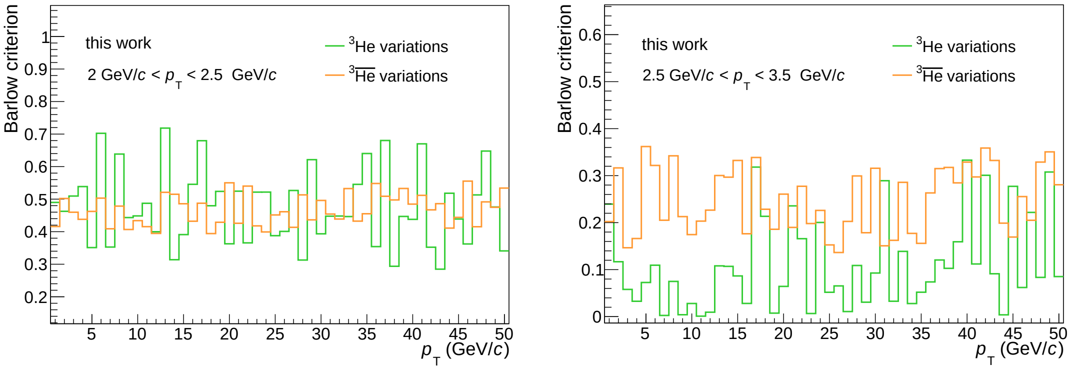

Figure 4.24: Absolute values of the Barlow criterion calculated for each tracking variation of (anti)helium in its lowest transverse momentum bins, 2.0 GeV/c $< p_\mathrm{T} <$ 2.5 GeV/c and 2.5 GeV/c $< p_\mathrm{T} <$ 3.5 GeV/c.

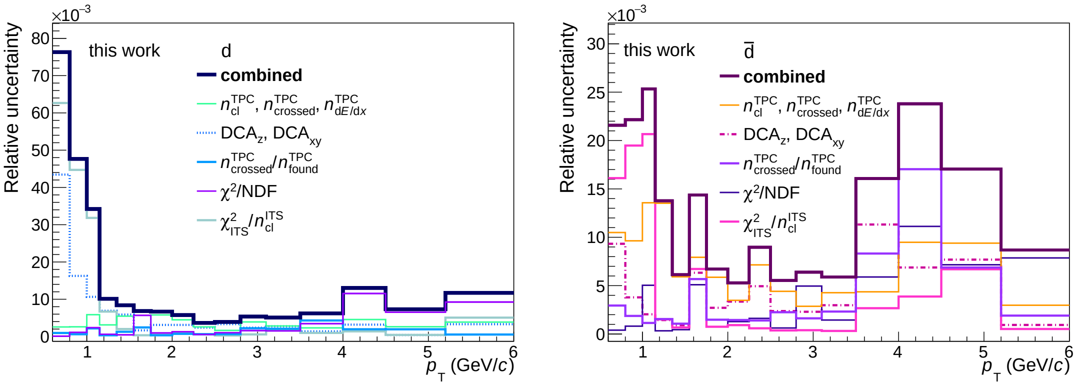

Figure 4.25: The total tracking uncertainty together with its individual components for deuterons (*left*) and antideuterons (*right*).

criterion, in two p_T bins, estimated for helium using the aforementioned variations. The systematic uncertainty of track selection is neglected since $|C| < 1$ in all four bins.

The test was not done for deuterons since the variations were investigated for each cut individually, resulting in smaller deviations from the default value x_def,and hence a smaller C. A conservative decision was made to avoid underestimating the uncertainty by keeping the calculated values added in quadrature. The total tracking uncertainty, as well as its constituents, are given in Figure 4.25 in the two panels for deuteron and antideuteron. It is dominated by the cut on $\chi^2_\mathrm{ITS}/n^\mathrm{ITS}_\mathrm{clusters}$ in the first bins of deuterons, which is not surprising considering the effect of this cut on the secondary deuteron particles (see Figure 4.1).

Signal extraction

The fits used to extract the deuteron counts allow for a more accurate distinction between the signal and the background (as well as for suppression of statistical fluctuations). However, they may originate a systematic over- or underestimation of the yields. To take this into consideration, the background fits are subtracted from the measured distributions, and the remaining counts are summed in the same n_σ regions as done for fits. Half the difference between the yields obtained with the two methods is included in the systematic uncertainty, amounting to about 1.5% on average. This (and other contributions to PID) are relevant for (anti)deuterons only, as the (anti)helion counts are obtained by simple summation and are (mostly) already limited to $|n_\sigma^{\mathrm{TPC}}| < 3$.

The extraction range ($-2.5 < n_\sigma^{\mathrm{TPC}} < 3.2$ and $-3.0 < n_\sigma^{\mathrm{TOF}} < 3.5$) is itself an estimate based on the distribution shapes and the knowledge of the detector response. Fifty variations were generated to estimate the uncertainty due to a possible under- or over-counting of candidates based on their PID response. For the TOF, the left bound of the extraction range is uniformly varied in the interval (-4.0, -2.0) and the right one in (2.5, 4.0). Similarly, the TOF ranges were (-4.9, 2.5) and (3.0, 4.5). This contribution is of the order of 1% for deuteron and antideuteron.

The final uncertainty due to the PID is computed as a quadratic sum of the two contributions.

ITS-TPC matching efficiency

The ITS-TPC matching efficiency is defined as a fraction of tracks with clusters in both the TPC the ITS to the total number of tracks in the TPC. Discrepancies between the values computed with the data and the simulation indicate limited knowledge of the underlying processes and must be evaluated and included in the final uncertainty. This task is performed once by the ALICE Data Preparation Group for each beam and detector configuration [30] and is known to be the same for all particle species since it depends only on the detector conditions for each collision system and energy. The values recommended for Xe−Xe collisions at 5.44 TeV are shown in Figure 4.26, together with the reweighted values in the transverse momentum intervals of the current (anti)helion analysis. The reweighting is done using the Levy-Tsallis function (for deuterons) and the m_{T}-exponential (for helions) from the study of the p−Pb system at $\sqrt{s_{\mathrm{NN}}} = 8.16$ TeV [12].

Secondary nuclei from material

In the case of deuterons, a part of the uncertainty due to the primary particle correction is already indirectly included in tracking, where the value of the DCA$_{xy}$ cut is randomly generated. Other sources of uncertainties are the binning of DCA$_{xy}$ distributions, the p_{T} intervals (and their size) used for fitting the function describing the fraction evolution in momentum, and the function itself. The first two are calculated together using 70 variations by an algorithm that rebins the DCA counts in all possible ranges from -1.3 cm $<$ DCA$_{xy}$ $<$ 1.3 cm to -0.4 cm $<$ DCA$_{xy}$ $<$ 0.4 cm (default is -1.1 cm $<$ DCA$_{xy}$ $<$ 1.1 cm), also making sure that the central bins are the most narrow ones. At the same time, the p_{T} intervals for template fits are slightly varied (bin width ranging from 0.03 GeV/c to 0.15 GeV/c). If the final fits of the primary fraction in momentum have a χ^2/NDF value higher than four, then the whole algorithm is

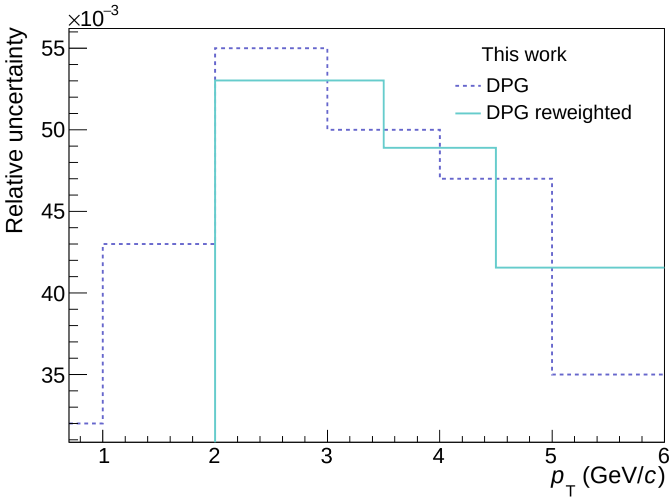

Figure 4.26: Values of systematic uncertainty due mismatched ITS and TPC tracks, calculated by the Data Preparation Group of ALICE [30] and reweighted for use in this analysis.

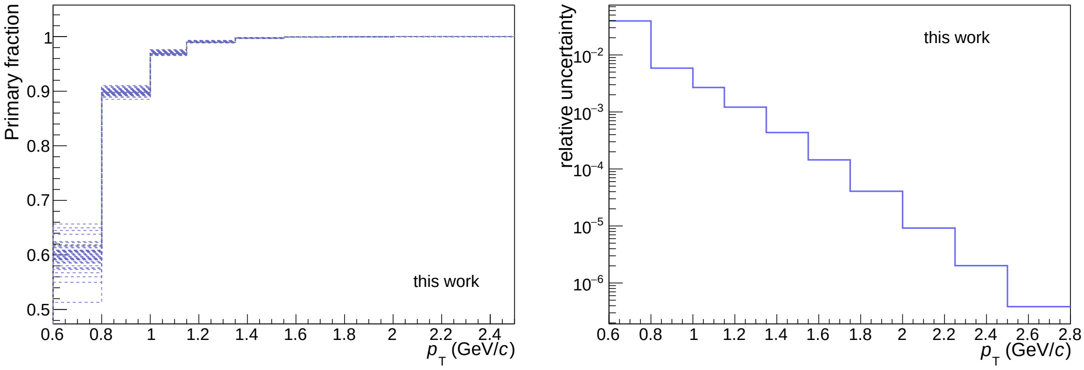

Figure 4.27: *Left*: values of primary fractions in each transverse momentum bin, obtained by varying the bins of DCA$_{xy}$ distributions and their intervals 70 times, each time fitting the points with a function and finally integrating the function in the intervals of the deuteron study, divided by their widths. *Right*: the resulting uncertainty in half-logarithmic representation.

recursively repeated and the above steps are performed again. For the used 70 variations additional 200 were generated and discarded based on this condition. The contribution is relevant only in the lowest bins since it falls exponentially with p_{T} (see Figure 4.27).

The primary fraction is also estimated in the default configuration of Section 4.2.3 using the functions shown in Figure 4.16. The uncertainty amounts to the difference between the maximum and minimum values of the yield, obtained with the functions in each momentum interval of the analysis[11], divided by two. It is negligible in all the bins but the first two, as it is already clear from Figure 4.16.

---

[11] The integral of each function is taken in the corresponding momentum interval of the analysis and then divided by the interval width.

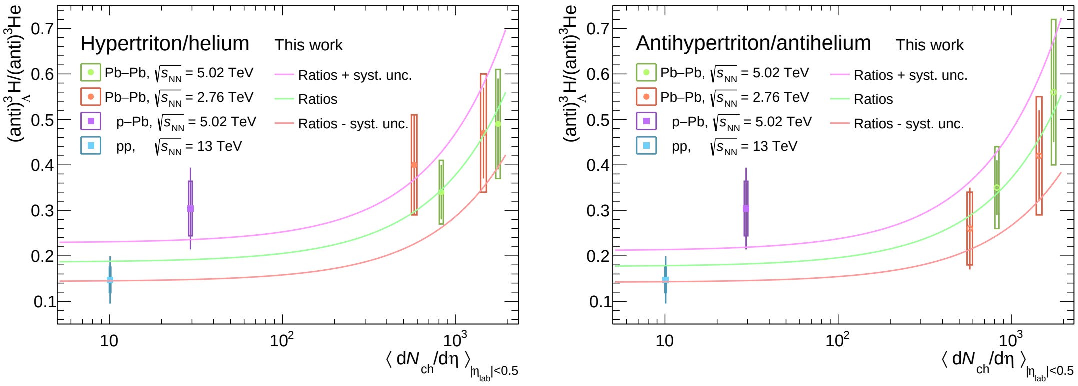

Figure 4.28: ALICE measurements of (anti)hypertriton/(anti)helium ratios in different systems, fitted with a linear function (light green line) in a half-logarithmic scaling. The other two lines represent the fits of the data points shifted up and down by their systematic uncertainty. Statictical (systematic) uncertainties are indicated by vertical lines (boxes).

Secondary nuclei from feed-down

The hypertriton-to-helium ratio, needed for the calculation of the feed-down fraction of helions, is extrapolated using the limited knowledge of the hypertriton production at different multiplicities, inevitably leading to uncertainties. The ratios are shifted upwards and downwards by their systematic uncertainties and fitted again by a linear function (Figure 4.28). Half of the difference between the values predicted by these two functions for the multiplicity of this study (331.3) is taken as the uncertainty of the ratio. The branching ratio of the hypertriton two-body decay, another component of the feed-down correction, was measured by the STAR collaboration with an upper limit of 40%. The final feed-down uncertainty is evaluated by using the maximum and minimum values of $^3_\Lambda$H/^{3}He and BR to get two extremes of $f_{\text{feed-down}}$ and dividing the difference by two. It amounts to around 2% in all momentum bins.

Deuterons, by contrast, were found to be unaffected by the weak decay of hypertriton [12], so no correction is included.

Triton contamination

Although the background contamination of the n_σ^{TPC} distributions of helium is considered insignificant (see Figure 4.5), it is still evaluated in the first two p_{T}-bins and included in the uncertainty. The counts at negative values of n_σ^{TPC} ($-6 < n_\sigma^{\text{TPC}} < -3$) are fitted with a Gaussian and an exponential function (Figure 4.29), taking half the difference in the resulting yields as uncertainty. The resulting uncertainty is 3% in the first bin and 8% in the second.

Material budget, hadronic interaction and TPC-TOF matching

The detector material budget stands for the thickness up to the middle point of the TPC, expressed in units of the radiation length. It is determined in photon conversion studies with a precision of 4.5% [22]. To estimate its effect on the reconstruction efficiency,

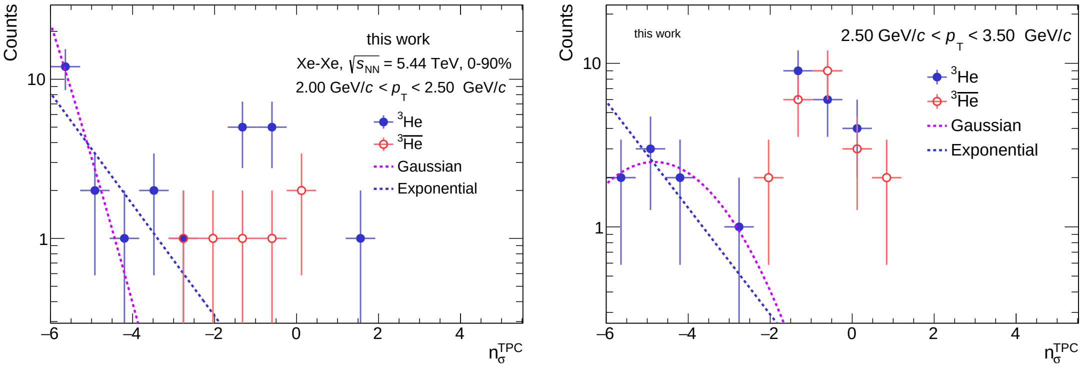

Figure 4.29: n_σ^{TPC} distributions of (anti)helions, with supposed the triton contamination fitted by a Gaussian (exponential) function, plotted in blue (purple).

dedicated Monte Carlo simulations are produced with the material budget changed by $\pm 4.5\%$; reconstruction efficiencies $\varepsilon_{\mathrm{max}}$ and $\varepsilon_{\mathrm{min}}$ are then recalculated for the two cases and the relative uncertainty σ_{MB} is obtained as

$$\sigma_{\mathrm{MB}}(p_{\mathrm{T}}) = \frac{\varepsilon_{\mathrm{max}}(p_{\mathrm{T}}) - \varepsilon_{\mathrm{min}}(p_{\mathrm{T}})}{2\varepsilon_{\mathrm{def}}(p_{\mathrm{T}})}$$

where $\varepsilon_{\mathrm{def}}$ stands for the efficiency obtained with the default material budget. In the present case, this uncertainty is inherited from the previous analyses [12, 13] (since it is not expected to be dependent on the collision system), amounting to 1% for (anti)deuterons and 0.2%-0.3% for ^{3}He.

The hadronic cross-section, describing the interaction probability of particles with the detector material, is used as an input in the Monte Carlo simulation and is subject to uncertainty. Figure 4.30 shows the ALICE measurements of the anti-^{3}He cross-section for several values of momentum. The default GEANT4 prediction (red line) is scaled to obtain the best fit to data (blue dashed line) with an uncertainty (blue band), resulting in 0.77 ± 0.21. The effect on the reconstructed particle spectra is computed using new MC productions, with the cross-section parameterized by (0.77 ± 0.21) times the default value σ_{G4}, giving the uncertainty of 3% for antihelions, momentum-independent [12]. An analogous calculation yields 1% for helions.

Another uncertainty, related to the TPC-TOF matching efficiency, originates from the material budget of the TRD detector and is only relevant for deuterons, for which the TOF is used for particle identification. It can be traced back to the measurements of proton interaction length λ_I in the TRD and the total inelastic cross-sections for protons and deuterons. The resulting uncertainty is p_{T}-dependent, with a rise at 1 GeV/c and from 4 GeV/c onward. The values can be found in Table 4.3.

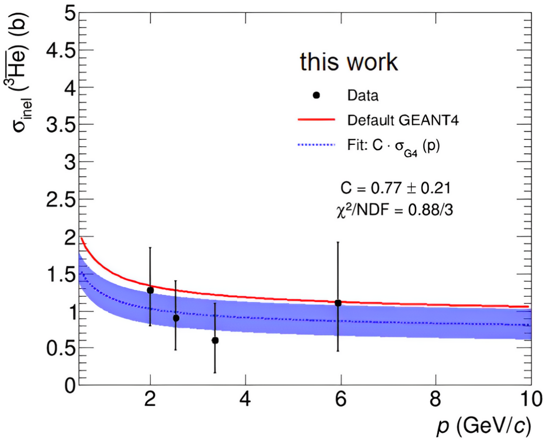

Figure 4.30: ALICE measurements of the total inelastic antihelium cross-section for several values of momentum. The red line shows GEANT4 prediction, the dashed blue line with the band is the fit to the data and its uncertainty.

5 Results

In this chapter, the final results of the study are reported, combining the intermediate steps of the analysis Chapter 4. First, in Section 5.1 the transverse momentum spectra of (anti)helions and (anti)deuterons are presented, with applied corrections for the detector acceptance and efficiency, primary fraction, and feed-down (for helions). The spectra are fitted with Blast Wave function which are also shown. Then in Section 5.2, integrated yields are calculated together with their uncertainties. Matter-to-antimatter ratios are given in Section 5.3, followed by a comparison of some observables to the predictions by the coalescence and the statistical model (Section 5.4).

5.1 Corrected spectra

The corrections to the raw yields are applied according to Eq. 5.1 for (anti)helions and Eq. 5.2 for (anti)deuterons:

$$\frac{\mathrm{d}^2N}{\mathrm{d}y\,\mathrm{d}p_\mathrm{T}} = \frac{1}{N_\mathrm{events}}\frac{N_\mathrm{obs}(p_\mathrm{T})}{\Delta y \Delta p_\mathrm{T}(\alpha\times\varepsilon)(p_\mathrm{T})}(1-f_\text{feed-down}(p_\mathrm{T})) \tag{5.1}$$

$$\frac{\mathrm{d}^2N}{\mathrm{d}y\,\mathrm{d}p_\mathrm{T}} = \frac{1}{N_\mathrm{events}}\frac{N_\mathrm{obs}(p_\mathrm{T})f_\mathrm{primary}(p_\mathrm{T})}{\Delta y \Delta p_\mathrm{T}(\alpha\times\varepsilon)(p_\mathrm{T})} \tag{5.2}$$

where N_obs stands for the raw counts, N_events for the number of the collected events (1.14×10^6), $\alpha\times\varepsilon$ is the detector acceptance and reconstruction efficiency, $f_\text{feed-down}$ is the fraction of (anti)helions originating from weak decays, f_primary is the fraction of deuterons produced in primary vertex and $\Delta y\,\Delta p_\mathrm{T}$ are, as before, the widths of the rapidity and transverse momentum intervals. The results for (anti)deuterons and (anti)helions are shown in Figures 5.1, 5.2, respectively.

The spectra are fitted with the Boltzmann-Gibbs Blast Wave function, used for a hydrodynamical description of particles produced by an expanding medium in local thermal equilibrium (Eq. 5.3). This allows one to make predictions for the spectra in the unmeasured regions[1].

$$\frac{1}{p_\mathrm{T}}\frac{\mathrm{d}^2N}{\mathrm{d}p_\mathrm{T}\,\mathrm{d}y} = A\int_0^R \mathrm{d}r\, r m_\mathrm{T} I_0\left(\frac{p_\mathrm{T}\sinh\rho}{T_\mathrm{kin}}\right)K_1\left(\frac{m_\mathrm{T}\cosh\rho}{T_\mathrm{kin}}\right) \tag{5.3}$$

Here A is a normalisation factor, I_0 and K_1 are the modified Bessel functions of the first and second kind, $m_\mathrm{T}=\sqrt{m^2-p_\mathrm{T}^2}$ is the transverse mass, r and R are the radial distance from the centrer and the radius of the fireball, $\rho=\tanh^{-1}(\beta(r))=\tanh^{-1}(\beta_\mathrm{S}(r/R)^n)$ is

---

[1] which are $p_\mathrm{T} < 0.6$ GeV/c and $p_\mathrm{T} > 6.0$ GeV/c for deuterons, and $p_\mathrm{T} < 2$ GeV/c and $p_\mathrm{T} > 6.0$ GeV/c for helions.

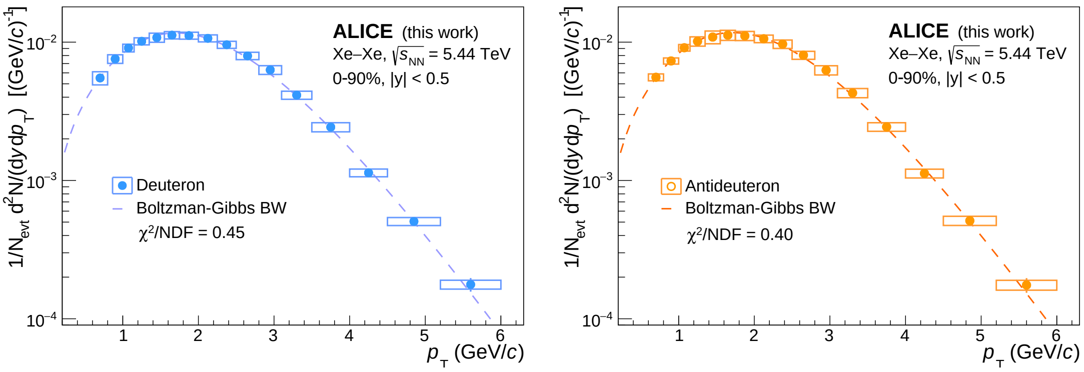

Figure 5.1: Transverse momentum spectrum of deuteron (*left*) and antideuteron (*right*) n the integrated-multiplicity class after applying the corrections discussed in the text.

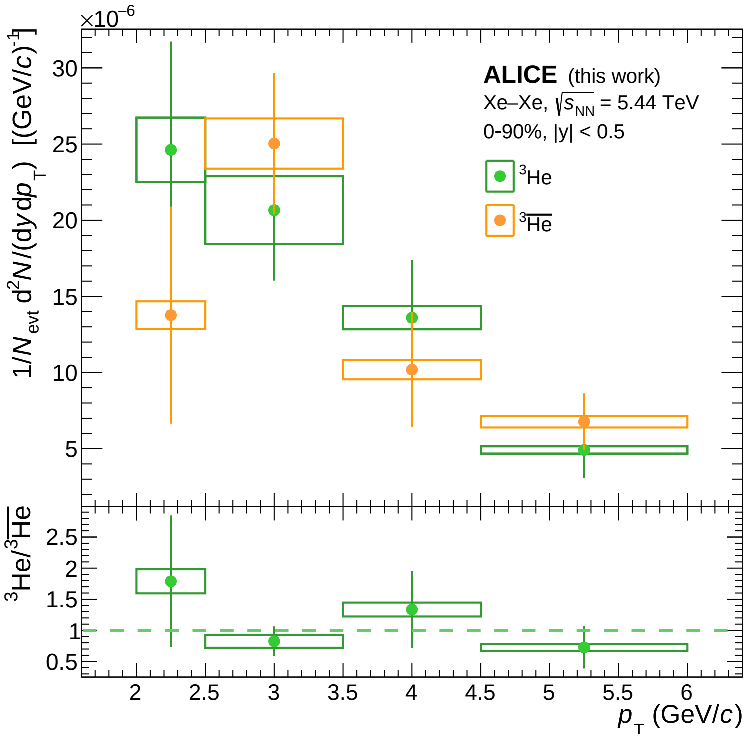

Figure 5.2: Transverse momentum spectrum of the average helion and antihelion spectrum in the integrated-multiplicity class after applying the corrections discussed in the text and matter-to-antimatter ratios.

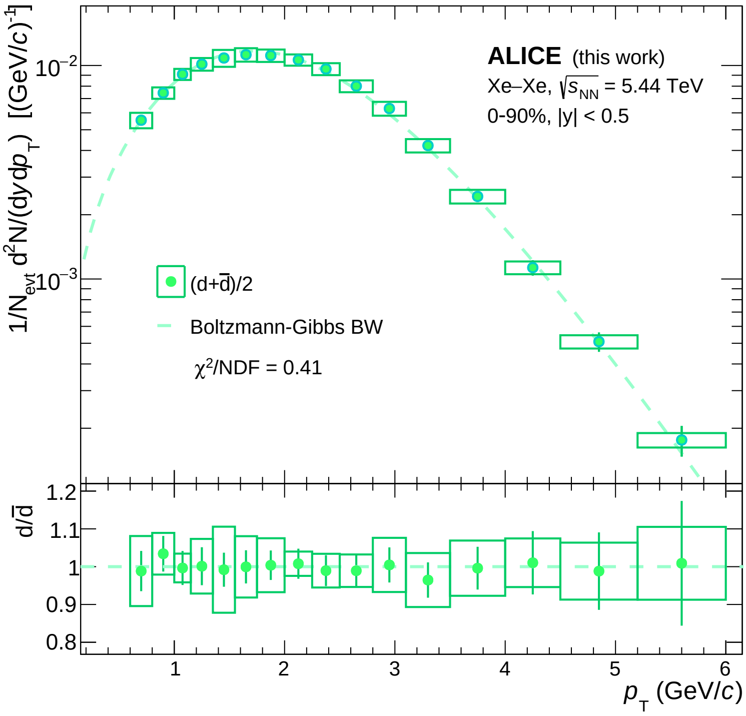

Figure 5.3: Transverse momentum spectrum of the average deuteron and antideuteron spectrum in the integrated-multiplicity class after applying the corrections discussed in the text and matter-to-antimatter ratios.

Particle	M (GeV^2/c^2)	A	β	T_{kin} (MeV)	n
d	1.876	3371 ± 4688	0.75 ± 0.06	186.0 ± 37.8	0.53 ± 0.19
$\overline{\mathrm{d}}$	1.876	2782 ± 5372	0.75 ± 0.05	189.1 ± 28.9	0.52 ± 0.16
$(\mathrm{d} + \overline{\mathrm{d}})/2$	1.876	2940 ± 5281	0.75 ± 0.05	188.2 ± 30.1	0.52 ± 0.16
$(^3\mathrm{He} + {}^3\overline{\mathrm{He}})/2$	2.809	200 ± 764	0.74 ± 0.15	200.2 ± 4.8	0.23 ± 0.71

Table 5.1: Estimated values of the free parameters A, β, T_{kin} and n of the Blast wave fits (see text for details). The particle mass M is fixed.

particle	dN/dy	(dN/dy)$_{\mathrm{function}}$	Extrapolated	(dN/dy)$_{\mathrm{Pb-Pb}}$
$(^3\mathrm{He} +^3 \overline{\mathrm{He}})/2$	6.59×10^{-5}	6.60×10^{-5}	17.3%	$(10.71 \pm 1.79) \times 10^{-5}$
$(\mathrm{d} + \overline{\mathrm{d}})/2$	2.79×10^{-2}	2.78×10^{-2}	5.0%	$(3.97 \pm 0.70) \times 10^{-2}$

Table 5.2: Momentum-integrated yields dN/dy compared to the Blast Wave integrals (dN/dy)$_{\mathrm{function}}$ and the results from Pb−Pb collisions at $\sqrt{s_{NN}} = 2.76$ TeV (because of the spatial constrains, their statistical and systematic uncertainties are summed in quadrature). The extrapolated fraction is stated as well, i. e. the integral of the function in the unmeasured region divided by the total dN/dy.

the boost angle with transverse expansion velocity at r, $\beta(r)$, and at the surface, β_{S}, n is an exponent of the velocity profile and finally T_{kin} represents the temperature at the kinetic freeze-out. The Blast Wave function has four free parameters: A, β_{S}, T_{kin} and n. They are estimated from fits and given in Table 5.1. The fit of the average deuteron spectra is shown in Figure 5.3 with its χ^2 value.

5.2 Integrated yields

As already mentioned, the integrated yields dN/dy are obtained by integrating the spectra over the whole transverse momentum range. In the regions with data points, those are summed, while the Blast Wave fits are integrated in the low and high transverse momentum regions. The results can be seen in Table 5.2 and compared to the values obtained with fitted functions (dN/dy)$_{\mathrm{function}}$ alone and with those from a previous study in the Pb−Pb system at $\sqrt{s_{NN}} = 2.76$ TeV. In both cases, the data and the fits yield very close values of dN/dy. The resulting yields for Xe−Xe collisions are of the same order of magnitude as the yields measured in Pb−Pb collisions, slightly lower as expected for a smaller system.

In the following, the uncertainties of the yields are calculated. Since the Blast Wave function is used only as an approximation for the general shape of the spectra, other functions are also employed to account for eventual discrepancies in the fit. These are Levy-Tsallis, Bose-Einstein, Fermi-Dirac, Boltzmann, power law, and m_{T}-exponential functions. The exact forms used are given in Appendix, and the fits are shown in Figure 5.7. The Levy-Tsallis helion fit exhibits a larger deviation from the data points, but considering the smaller data sample and hence the larger statistical uncertainties, it is kept for further calculations.

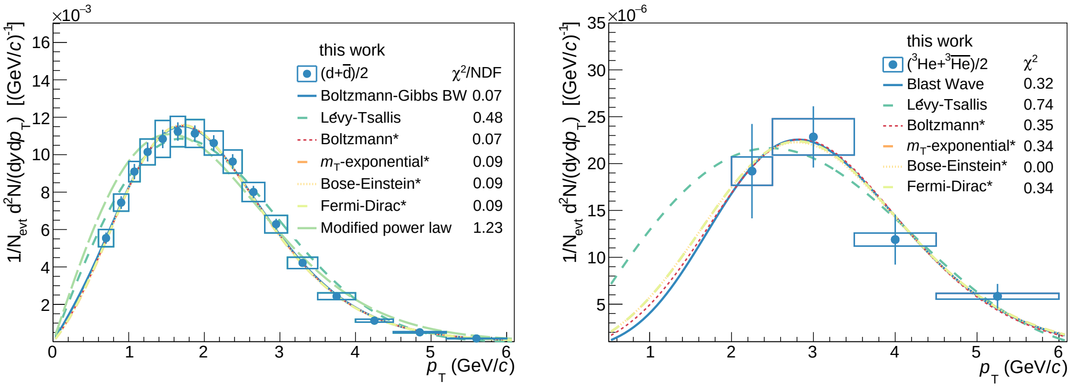

Figure 5.4: Average deuteron (*left*) and helion (*right*) spectra, fitted with different functional forms.

Shape	Mean ($\times 10^{-2}$)	Std. dev.($\times 10^{-2}$)	Uncertainty
Blast wave	2.792	0.031	1.11%
Boltzmann	2.783	0.032	1.15%
Levy-Tsallis	2.838	0.026	0.92%
Bose-Einstein	2.782	0.032	1.15%
Fermi-Dirac	2.783	0.032	1.15%
Power law	2.881	0.032	1.11%
m_{T}-exponential	2.782	0.032	1.15%
Average			**1.1%**

Table 5.3: Statistical uncertainties of the average deuteron yield calculated using different functions.

The statistical uncertainty of the integrated yield is estimated using the so-called Gaussian sampling method: points are shifted independently of each other by a Gaussian distribution centered at the default value with the sigma given by the statistical uncertainty of each point. This is done 1000 times, each time refitting the spectrum and obtaining the integrated yield. Some of the resulting distributions for different fitting shapes are shown in Figure 5.5. These are much more narrow for deuterons than for helions, which is evident considering the number of deuteron (16) and helion (4) p_{T}-bins and also their extrapolated fractions (Table 5.2). The uncertainty is calculated for each function as the standard deviation ratio to the corresponding distribution mean (see Tables 5.3 and 5.4). The average from all the shapes is then used as the final statistical uncertainty of the yield.

A distinction is made when calculating the systematic uncertainty: the uncertainties due to secondary particles, PID, material budget, and hadronic interaction are assumed to be correlated across transverse momentum, and the rest are not, as illustrated in Figure 5.6. The error propagation of the uncorrelated parts is done exactly as for the statistical one: using the Gaussian sampling on 1000 variations and taking the average values of standard deviation divided by the mean of the yield distribution for each shape. It is found to be 1.90% (4.28%) for deuterons (helions). The correlated part is found by shifting the values up and down all at once and taking the semi-difference of the resulting yields (Figure

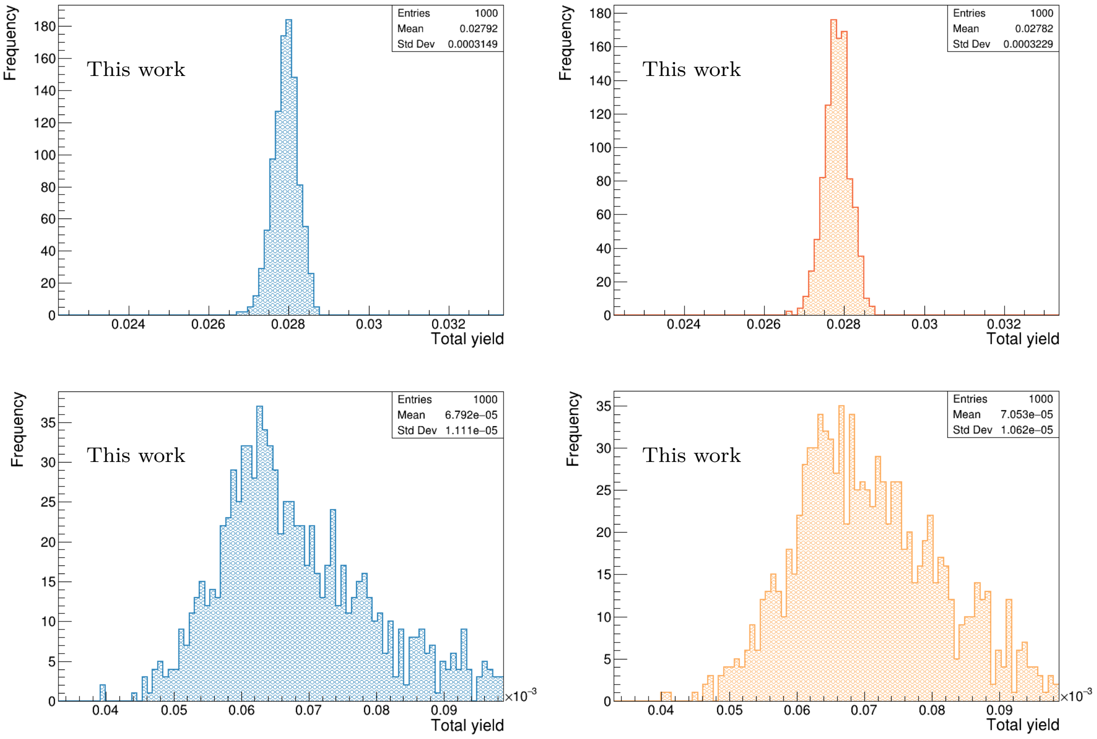

Figure 5.5: Distributions of integrated yields from the Gaussian sampling of 1000 statistical variations of deuterons (top panel) and helions (bottom panel).The blue plots show the distributions obtained with the Blast wave function, the red plots the ones with Bose-Einstein density.

Shape	Mean ($\times 10^{-5}$)	Std. dev.($\times 10^{-5}$)	Uncertainty
Blast wave	6.791	1.111	16.36%
Boltzmann	8.131	1.121	13.79%
Levy-Tsallis	6.945	0.961	13.84%
Bose-Einstein	7.053	0.062	15.06%
Fermi-Dirac	6.747	1.005	14.90%
m_{T}-exponential	6.884	1.103	16.02%
Average			**15.0%**

Table 5.4: Statistical uncertainties of the average helion yield calculated using different functions.

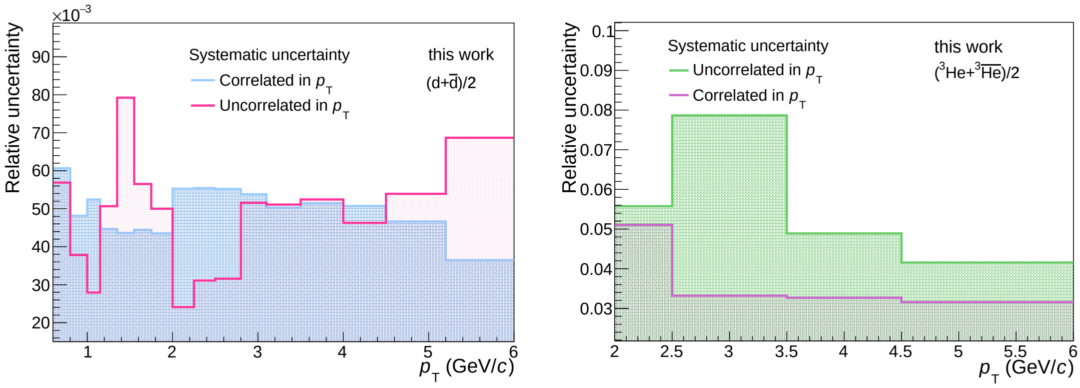

Figure 5.6: Momentum-correlated and uncorrelated contributions to the total systematic uncertainty of each analysis bin of deuteron (*left*) and helion (*right*).

5.6). The contribution is 4.61% (4.59%).

The remaining part of the uncertainty is due to the approximate nature of the fitted shapes. Again the semi-difference between the maximum and the minimum yields, computed with all the mentioned functions, is taken, amounting to 1.78% (8.95%) for deuterons (helions). It is mentioned at the beginning of the section that for helium, the Levy-Tsallis function deviates considerably from the others at lower momenta ($p_T < 2$ GeV/c), causing a higher uncertainty of almost 9% as a result. It is nevertheless considered to provide a reasonable description of the extrapolated spectrum.

The final systematic uncertainty is obtained by adding all the contributions in quadrature, the final result being:

$$\begin{aligned} &\text{Helium} \qquad && \mathrm{d}N/\mathrm{d}y = (6.586 \pm 0.988 \pm 0.718) \times 10^{-5} \\ &\text{Deuteron} \qquad && \mathrm{d}N/\mathrm{d}y = (2.790 \pm 0.031 \pm 0.147) \times 10^{-2} \end{aligned}$$

For completeness, individual components of the uncertainties of deuterons, helions, and protons (see Section 5.4) are listed in Appendix (Table 7.1).

5.3 Matter-to-antimatter ratios

The ratios of particles to antiparticles were already shown in Figures 5.2 and 5.3 for individual p_T-bins. They are now calculated for the total measured momentum range.

The total ratio is obtained by fitting the p_T-depenndent ratios of with a constant function, with weights provided by the statistical uncertainties propagated from yields; the statistical error of this value is hereby given directly by the error of the fitted parameter. The systematic uncertainty of the (p_T-dependent ratios ΔR) is obtained by treating differently the parts of the uncertainties which are correlated and uncorrelated between particles and antiparticles:

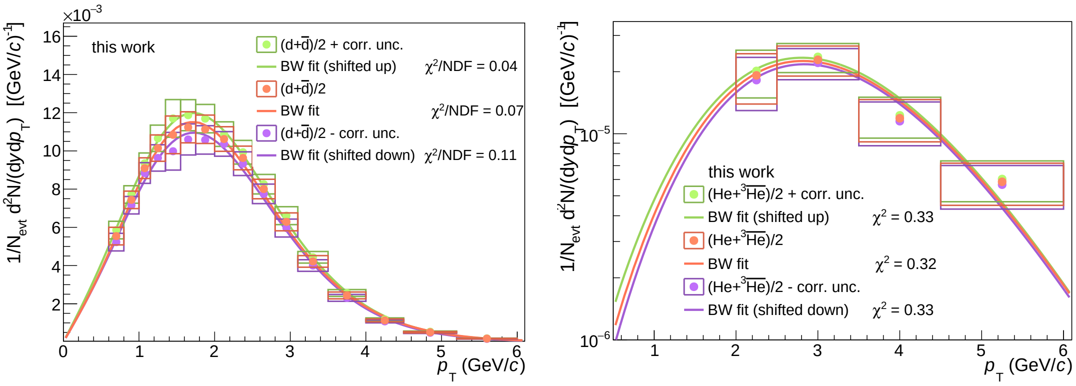

Figure 5.7: To the calculation of the correlated contribution to the total systematic uncertainty of yield: average deuteron (*left*) and helion (*right*) values (orange points) are shifted by the correlated part of their uncertainty (green and purple points) and fitted with the Blast Wave function.

$$\frac{\Delta R}{R} = \sqrt{\left(\frac{\Delta \bar{A}}{\bar{A}}\right)^2_{\text{uncorr}} + \left(\frac{\Delta A}{A}\right)^2_{\text{uncorr}} + \left(\frac{\Delta \bar{A}}{\bar{A}} - \frac{\Delta A}{A}\right)^2_{\text{corr}}} \tag{5.4}$$

Where $\Delta A/A$ is the correlated (or uncorrelated) part of the systematic uncertainty of a nucleus and $\Delta\bar{A}/\bar{A}$ of an antinucleus. It is conservatively assumed that the uncertainties due to tracking, ITS-TPC matching, material budget, and (in the case of helium) due to feed-down are correlated between particles and antiparticles, while the others are not. As shown in Figure 5.8, the points (full symbols) are then shifted upwards and downwards (hollow symbols) by the systematic uncertainties and fitted again. The semi-difference of these two values is taken as the uncertainty on the final ratios, shown as bands in the figure. The results are:

Deuteron	$\mathrm{R} = 1.00 \pm 0.01 \pm 0.06$
Helium	$\mathrm{R} = 0.87 \pm 0.18 \pm 0.09$

The ratios are found to be compatible with one within the uncertainties, implying a vanishing baryochemical potential as was already the case in the previous ALICE studies.

5.4 Comparison to models

Proton yield

To calculate the observables which then can be used for a direct comparison with model predictions (SHM and coalescence, see Chapter 2), knowledge of the proton spectrum is required. Proton production in the Xe−Xe system was analysed together with pions, kaons and ϕ-mesons in a recent study [25] in several centrality classes (Figure 5.9). Since only the minimum bias events are analyzed in he current work, the corresponding proton spectrum is obtained by combining the spectra of individual centrality classes multiplied

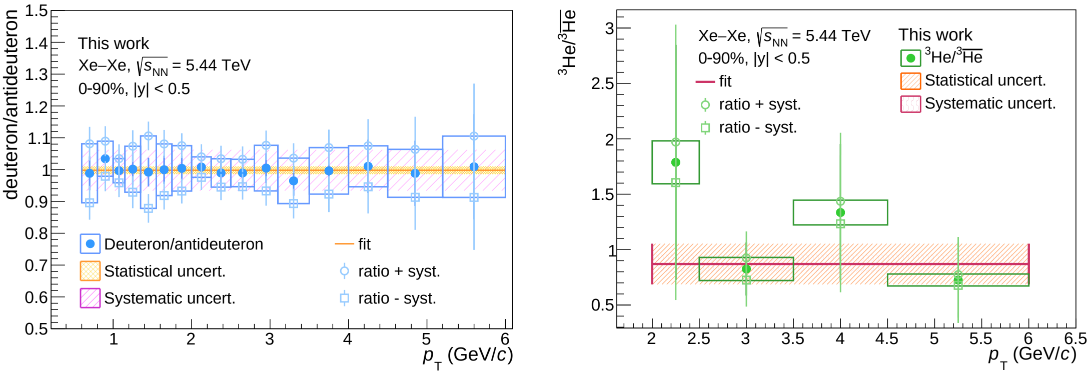

Figure 5.8: Matter-to-antimatter ratios for deuteron (*left*) and helion (*right*). The data points are shown as full circles, while the shifted points used for the estimation of the systematic uncertainty are hollow. Vertical lines represent the statistical uncertainties, boxes the systematic ones. The bands show the uncertainties estimated for the total ratios.

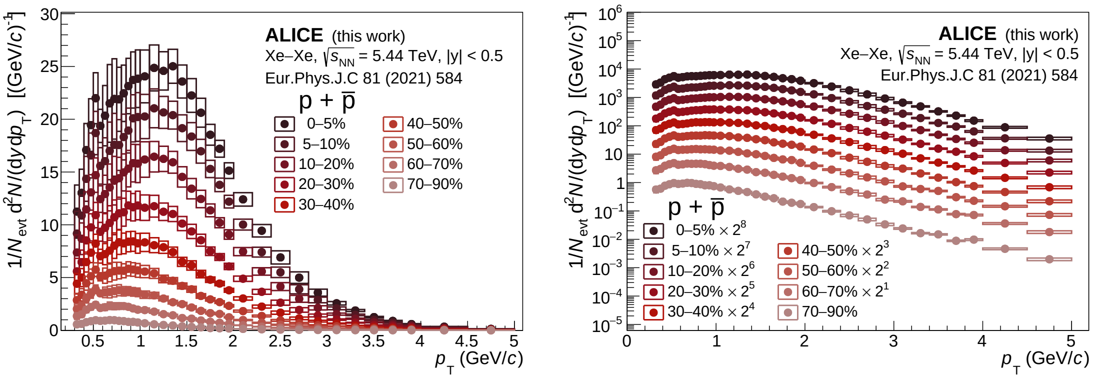

Figure 5.9: Proton plus antiproton spectra in Xe−Xe collisions at $\sqrt{s_{\mathrm{NN}}} = 5.44$ TeV in a linear and a semi-logarithmic scale. These results are taken from Ref. [25].

by their fraction of centrality (with respect to the 90% of MB; so, e. g., all of the counts in the 5% most central events are multiplied by 5/90, and so on). This is possible due to the fact that the measured number of events is independent of the centrality. The resulting average proton spectrum is shown in Figure 5.10.

Coalescence parameters

The coalescence parameters B_2 and B_3 (Section 2.3) follow from Eq. 2.3 as

$$B_A = \left(\frac{1}{2\pi p_{\mathrm{T},\,A}}\left(\frac{\mathrm{d}^2N_A}{\mathrm{d}y\,\mathrm{d}p_{\mathrm{T},\,A}}\right)\right)\Bigg/\left(\frac{1}{2\pi p_{\mathrm{T},\,p}}\left(\frac{\mathrm{d}^2N_p}{\mathrm{d}y\,\mathrm{d}p_{\mathrm{T},\,p}}\right)\right)^A = \frac{(2\pi p_{\mathrm{T},p})^{A-1}}{A}\,\frac{\mathrm{d}^2N_A/\left(\mathrm{d}p_{\mathrm{T},A}\,\mathrm{d}y\right)}{\left(\mathrm{d}^2N_p/(\mathrm{d}p_{\mathrm{T},\,p}\,\mathrm{d}y)\right)^A}$$

for a nucleus of mass number A. Here, $\mathrm{d}^2N/(\mathrm{d}p_{\mathrm{T},\,p}\,\mathrm{d}y)$ denotes the p_{T}-differential proton yield and $\mathrm{d}^2N_A/\left(\mathrm{d}p_{\mathrm{T},A}\,\mathrm{d}y\right)$ the yield of deuterons or helions, scaled down according to the relation $p_{\mathrm{T},\,p} = p_{\mathrm{T},\,A}/A$. To build the yield ratios, protons are reweighted and

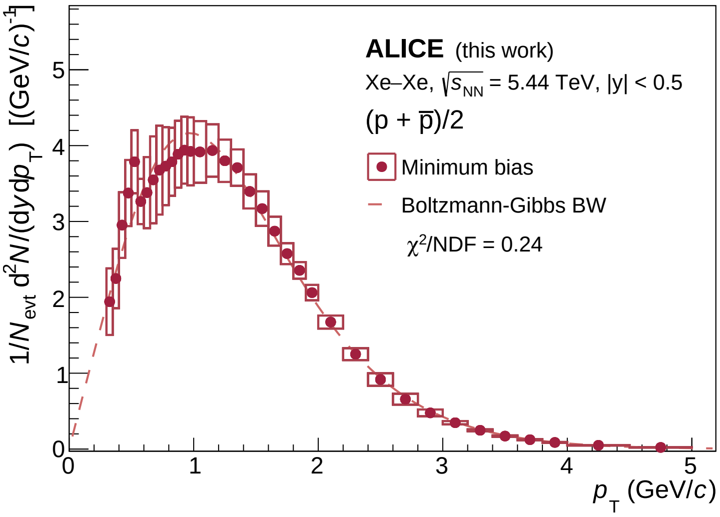

Figure 5.10: Average proton spectrum, calculated for the 0-90% centrality, using the data of Ref. [25].

rebinned as shown in Figure 5.11. The evolution in transverse momentum of the coalescence parameters B_2 and B_3 is presented in Figure 5.12. The B_2 and B_3 increase with increasing momentum, which is also observed in other systems at different energies. It may be linked to the size of the emitting source as suggested by the modern coalescence models but can not be explained by simple coalescence, see Section 2.3.

Also the EPOS event generator [31] was used to simulate the proton spectra with a total of around 2.8 million events. By rescaling the generated proton spectra to match the data and applying the p_T-dependent correction on an event-by-event basis, a source size of 6.9 fm was found to provide the best agreement with the data. The deuteron spectrum is then calculated with the Wigner formalism, described in details in Ref. [32] assuming a Gaussian wave function for the nucleus. The EPOS spectra is compared to the measurements in Figure 5.13. The ratios of the EPOS spectra to the data fits of protons and deuterons are shown in Figure 5.14. The shape of proton spectra is reproduced reasonably well (flat distribution with a systematic shift of around 6%, due to a larger abundance of antiprotons in the EPOS simulation), whereas the ratio for deuterons shows deviations from unity of around 50% depending on the p_T region. The comparison of the resulting B_2 coefficient from EPOS and from the data is shown in Figure 5.15. The simulation does not seem to reproduce the measurement (Figure 5.15), presumably due to the incomplete matching of the spectra: at higher momentum values ($p_T \gtrsim$1 GeV/c) EPOS overestimates protons and underestimates deuteron production.

Ratios to protons and T_{ch}

To verify the main conclusion of the SHM that a common freeze-out temperature T_{ch} underlies particle production at the stage of thermodynamic equilibrium (see Section 2.2), proton, deuteron and helion yields dN/dy are plotted against their mass number A

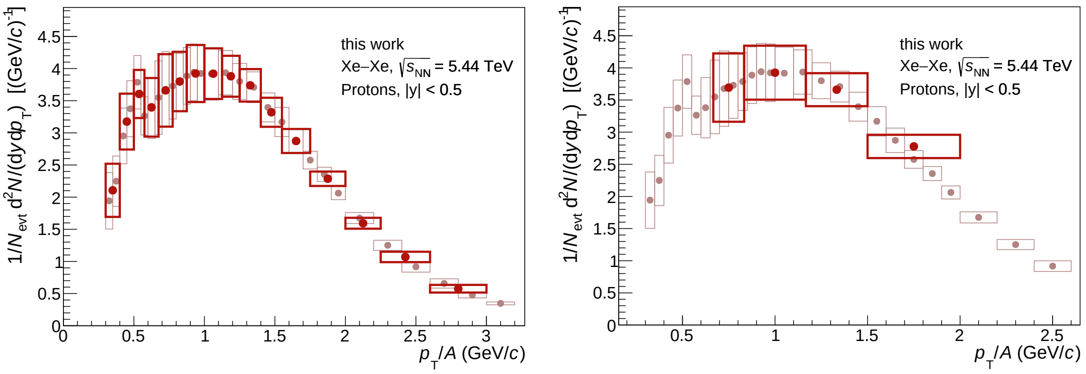

Figure 5.11: To the calculation of B_2 and B_3: proton measurements reweighted with the Blast Wave function and rebinned to match the bins of deuterons (*left*) and helions (*right*), which are scaled down according to the relation $p_{\mathrm{T},\,p} = p_{\mathrm{T},\,A}/A$; see Section 2.3. The default values are light, the rebinned ones are darker and brighter.

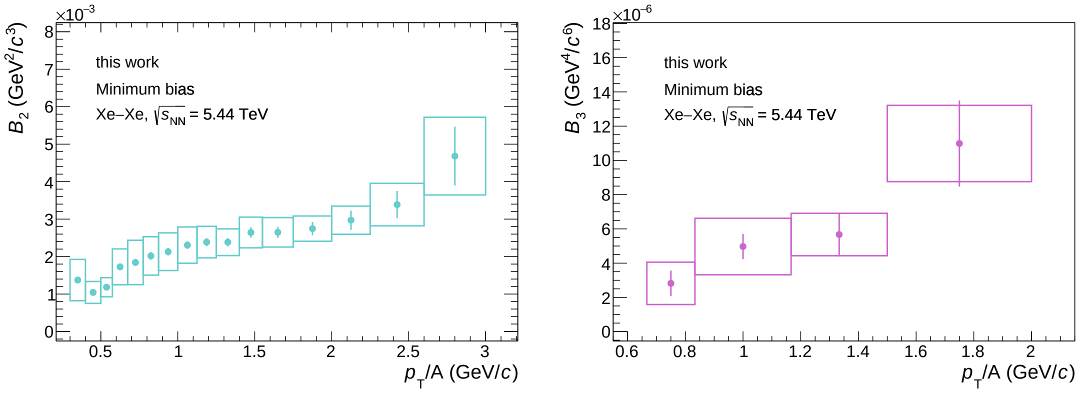

Figure 5.12: Coalescence parameters B_2 and B_3 as a function of p_{T}/A in the multiplicity-integrated MB events. Like before, lines result from propagation of the statistical uncertainties, boxes from the systematic ones.

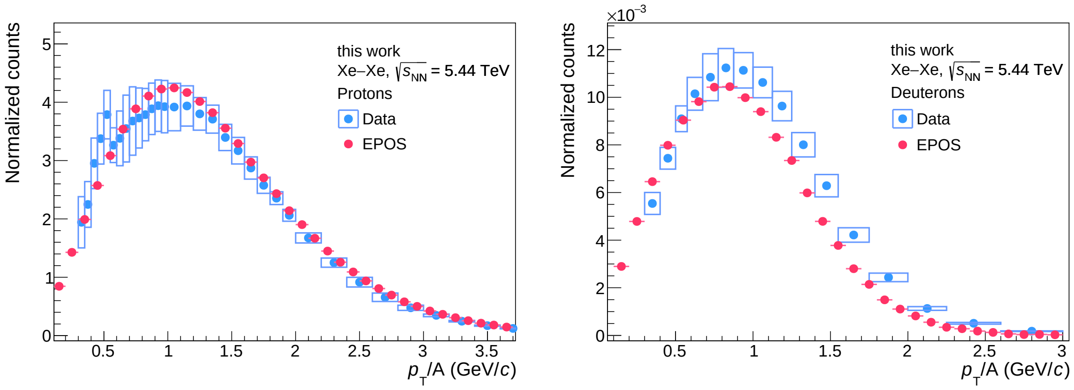

Figure 5.13: Spectra of protons (*left*) and deuterons (*right*) as a function of transverse momentum divided by the mass number. The EPOS simulations were performed and the results provided by Maximilian Horst in a private correspondence.

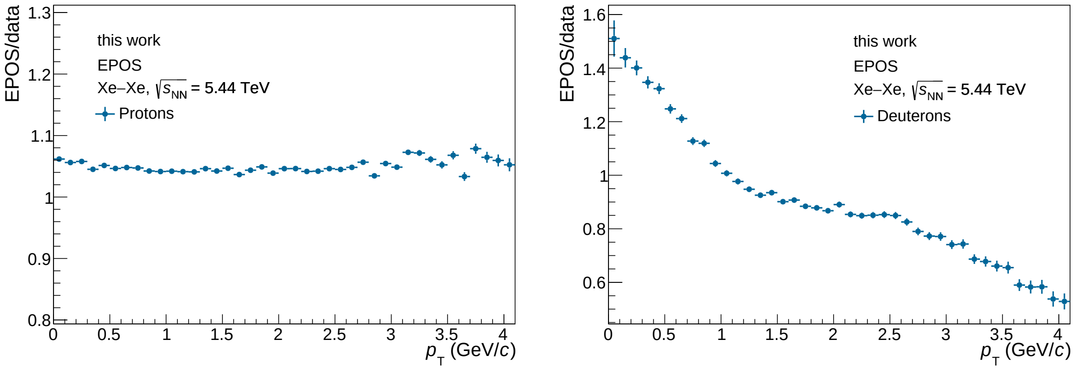

Figure 5.14: EPOS-to-data ratios for protons (*left*) and for deuterons (*right*) as a function of transverse momentum.

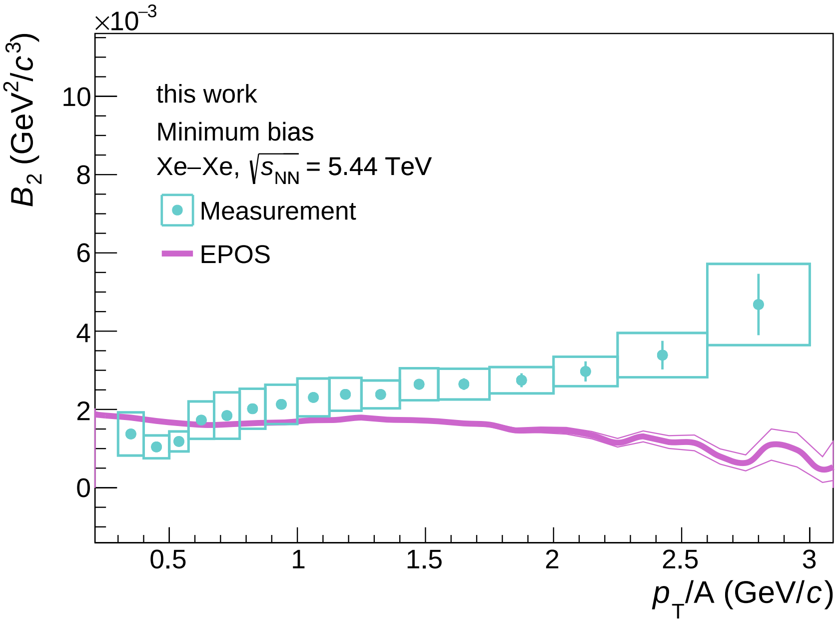

Figure 5.15: Comparison of B_2 from EPOS and the measurements. The EPOS simulations were performed and the results provided by Maximilian Horst in a private correspondence.

and fitted with:

$$\frac{\mathrm{d}N/\mathrm{d}y}{(2J+1)} = Ce^{-m/T_{\mathrm{ch}}}$$

where m is the particle mass and $2J+1$ accounts for the spin degeneracy of the particle (Figure 5.16). The fit yields the chemical freeze-out temperature

$$T_{\mathrm{ch}} = 158.6 \pm 2.8 \text{ MeV}$$

which is compatible with the values obtained in earlier ALICE measurements as well as lattice QCD calculations (Section 2.2). Particle yields in the Xe−Xe seem to follow an exponential trend with a penalty factor of 344 ± 51, which describes the yield suppression with every additional nucleon. As expected, this value is slightly higher then in Pb−Pb collisions (307 ± 76 at $\sqrt{s_{\mathrm{NN}}} = 2.76$ TeV [11]) and considerably lower then in p−Pb (668 ± 76 at $\sqrt{s_{\mathrm{NN}}} = 5.02$ TeV [13]) and pp (972 ± 169 at $\sqrt{s_{\mathrm{NN}}} = 5.02$ TeV [33]) collisions.

Particle yield ratios to protons offer a suitable observable to differentiate between light (anti)nuclei production mechanisms. The values obtained in this study together with all the other results of the ALICE Collaboration are shown as a function of charged particle multiplicity in Figure 5.17 for deuterons to protons in the top panel and for helium (and triton) to protons ratios in the bottom. Predictions by the coalescence and the canonical statistical models[2] are shown as well. The CSM assumes the chemical freeze-out temperature of 155 MeV and is realized for two values of the correlation volume, $V_c = \mathrm{d}V/\mathrm{d}y$ and $V_c = 3\mathrm{d}V/\mathrm{d}y$. In case of tritons and helions, the coalescence predictions for two- and three-body coalescence are plotted. The former assumes the creation of a deuteron as an intermediate step before the formation of a helion (triton).

The measurements in the Xe−Xe system confirm once again the smooth trend in multiplicity. The d/p and ^{3}He/p ratios measured by ALICE increase monotonously at lower multiplicities ($\langle \mathrm{d}N_{\mathrm{ch}}/\mathrm{d}\eta \rangle \lesssim 100$) and seem to saturate at higher. This is in qualitative agreement with both models. The coalescence models describe the deuteron ratios very well across the whole measured multiplicity range but are almost indistinguishable for values $\langle \mathrm{d}N_{\mathrm{ch}}/\mathrm{d}\eta \rangle \gtrsim 100$ from the CSM prediction. The increase in ratios going from pp to Pb–Pb and Xe–Xe systems is approximately 3 times greater for helions. Even if the measured ratio $(^{3}\mathrm{He} +^{3} \overline{\mathrm{He}})/(\mathrm{p} + \overline{\mathrm{p}})$ for Xe–Xe lies closer to the CSM line, it can still be compatible with the coalescence prediction considering the large statistical and systematic uncertainties, as well as the spread of measurements from Pb–Pb studies.

---

[2] Which, according to the standart statistical mechanics, converge to GC models at higher multiplicites.

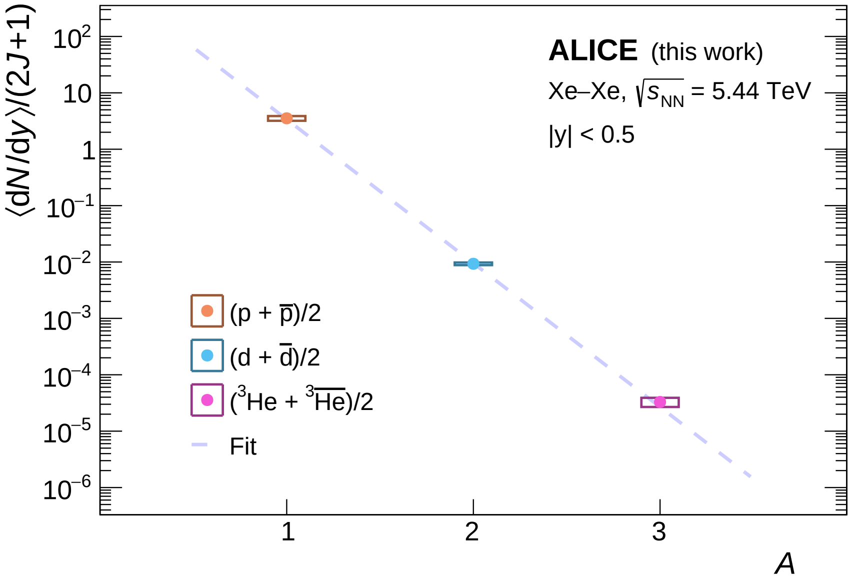

Figure 5.16: Yields of protons, deuterons and helions produced in Xe−Xe collisions at $\sqrt{s_{NN}} = 5.44$ TeV as a function of the mass number A. The height of the boxes corresponds to the quadratic sum of the statistical and systematic uncertainties, the width is chosen for visual purpose.

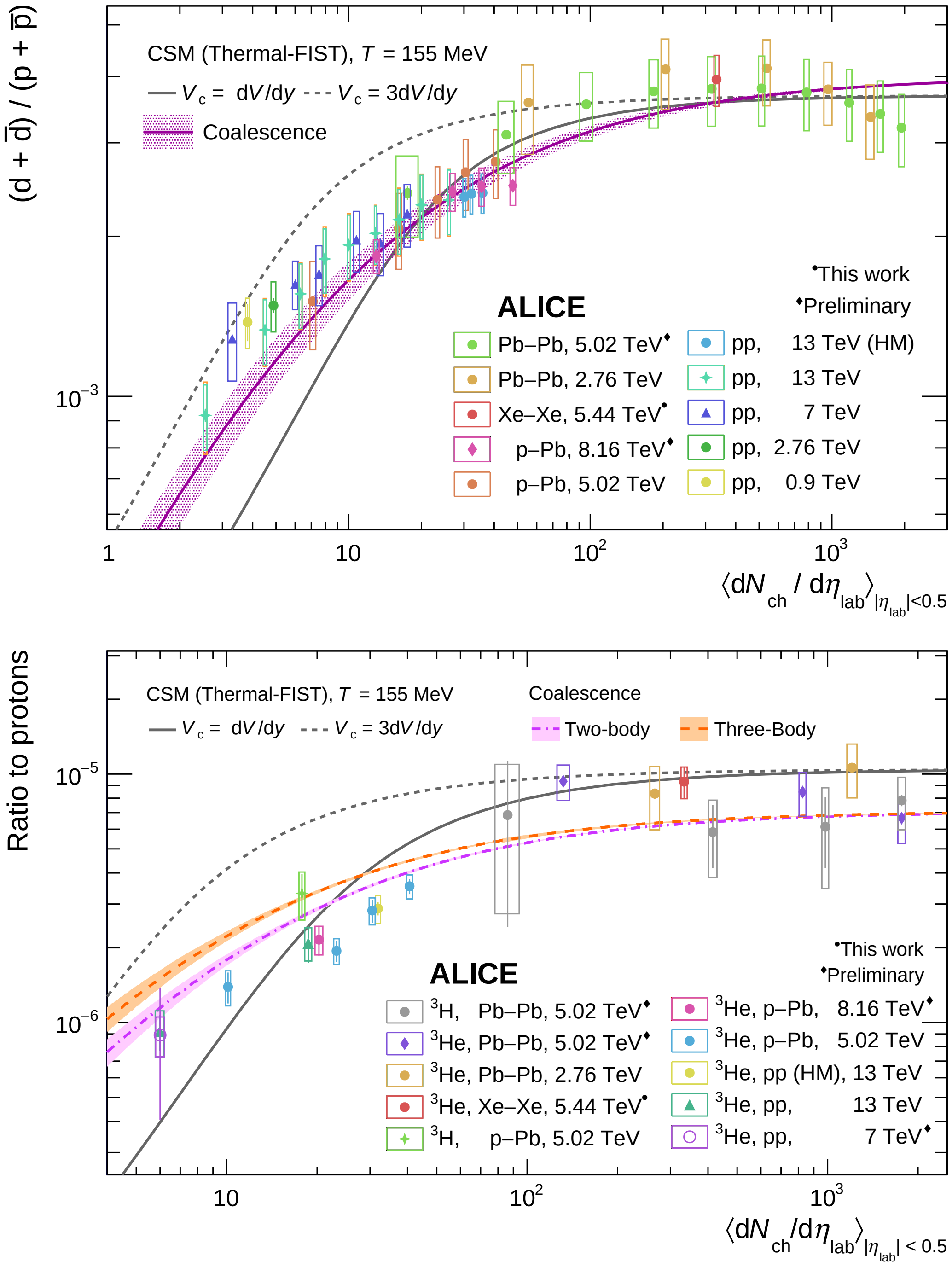

Figure 5.17: All available ALICE measurements of (anti)deuteron (*top*) and (anti)helion and (anti)triton (*bottom*) yields over proton yields as a function of the charged-particle multiplicity in different collision systems and energies, together with predictions of SHM and coalescence models. Vertical lines represent statistical uncertainties and boxes the systematic ones.

6 Conclusion and outlook

The first measurements of (anti)deuterons and (anti)helions in Xe−Xe collisions at $\sqrt{s_{\mathrm{NN}}} = 5.44$ TeV have been presented and discussed in this thesis. The data collected in October of 2017 at CERN by the ALICE detector provides a unique insight into a system of an intermediate size, bridging the gap between lower-multiplicity pp and p−Pb and high-multiplicity Pb−Pb collisions. The remarkable capabilities of the three main detector systems, the ITS, the TPC and the TOF, were exploited for track reconstruction and particle identification in the integrated-multiplicity class (MB). Helion and antihelion particles were analysed with the TPC in the transverse momentum range 2 GeV/$c < p_{\mathrm{T}} <$ 6 GeV/c, whereas the TPC and the TOF information was used for the identification of deuterons and antideuterons in the regions 0.6GeV /$c < p_{\mathrm{T}} <$ 1.15 GeV/c and 1.15 GeV/$c < p_{\mathrm{T}} <$ 6 GeV/c, respectively. Corrections to the raw spectra were applied using a dedicated GEANT4 simulation and the integrated yields were obtained by extrapolating the particle spectra to the unmeasured regions, with the extrapolated fraction being 17.3% for the average of helions and antihelions and only 5% for deuterons and antideuterons, thanks to the unique characteristics of the detector as well as the low field configuration of 0.2 T of the solenoidal magnet. The ratio of particles to the antiparticles was calculated in the total measured transverse momentum interval and was found to be consistent with unity for both (anti)helions (within uncertainties) and (anti)deuterons. The uncertainties of the integrated yields were slightly reduced in comparison with similar analyses at adjacent multiplicities (see, for example, Figure 5.17) by taking advantage of the better knowledge of the detector effects and differentiating between the correlated and uncorrelated contributions. Using the previously published results for protons, and the coalescence parameters B_2 and B_3 were calculated in the intervals 0.3 GeV/$c < p_{\mathrm{T}} <$ 3 GeV/c and 0.625 GeV /$c < p_{\mathrm{T}} <$ 2 GeV/c, respectively for deuterons and helions, and a rising trend was observed. In addition, a dedicated simulation was performed with EPOS, yielding a value of 6.9 fm for the size of the particle emitting source and a prediction for B_2, which, however, is not consistent with the measurement and requires further investigation. The common chemical freeze-out temperature was extracted from the fit of the total yields of protons, deuterons and helions in the present system and was found to be compatible with the previous studies and predictions hinting at the (local) thermodynamic equilibrium at some stage of the medium evolution. The yield penalty factor was measured to be close to previous results for Pb−Pb and much lower then for p−Pb, in agreement with the general considerations of the system size. Finally, the ratios to protons were given for the minimum bias centrality with the results supporting the idea of a smooth evolution with charged-particle multiplicity. This hints, once again, to a common production mechanism of particles independent of the colliding particles and the center-of-mass energy, but only depending the system size.

Outlook

After a three-year-long shutdown phase, a new period of operation of the LHC, Run 3, has started in July 2022. It was designed to provide considerably higher luminosities and collision rates, with the latter expected to reach 50 kHz in Pb−Pb collisions [34], to be compared with 80−150 Hz of the Xe−Xe collisions in 2017. To make use of these improvements the ALICE detector underwent a substantial upgrade during the shutdown. The ITS was restructured and now consists of 7 layers equipped with Monolithic Active Pixel Sensors (MAPS), each covering a smaller area then the SPD sensors and thus improving the resolution of the primary event vertex (and secondary decay vertices) as well as reducing the material budget thanks to the compact technology of MAPS[1]. An even more prominent change was made to the TPC, where the Multi-Wire Proportional Chambers (MWPCs) were replaced by the Gas Electron Multipliers (GEMs). GEMs consist of two copper surfaces under a voltage, enclosing an insulator layer in between; each such foil is perforated with small holes of the outer diameter of 70 μm. The purpose of this design is to reduce the dead time of the detector by preventing most of the ions (resulting from electron amplification) from travelling back into the drift region and distorting the otherwise homogeneous electric field. This results in a much higher data-taking rate of up to 50 kHz compared to the maximum of 3 kHz with the MWPC technology. Lastly, a new data handling system, the so-called Online-Offline O^2, is installed to cope with an increased data stream of up to 1.1 TB/s [35].

Higher data volumes will allow for more precise measurements of the light (anti)nuclei abundances, setting stricter constraints for the two models and helping to acquire a better understanding of particle production mechanisms as well as deeper insights into the nature of Quark Gluon Plasma. Higher luminosities will also pave way for the studies of heavier (hyper)nuclei, possibly the ones unobserved so far due to the statistics limitations. A better and deeper understanding of the production mechanism may eventually allow for a conclusive interpretation of any future measurements of antinuclei in space, reaching an important milestone in the searches of dark matter.

---

[1] More information on this and the other upgrades can be found in [34].

Acknowledgments

First, I would like to thank Professor Laura Fabbietti for the opportunity of working on such exciting project as a member of the world-renowned collaboration. It has been an honour to evaluate the measurements of one of the most complex machines ever created by humans, the ALICE detector at the LHC. Professor Fabbietti let me regularly present the status of my work to her and the whole TUM antinuclei group, taking time to listen to my updates and to give me valuable feedback, for which I am deeply grateful. I can not help but mention the atmosphere of science which I felt in group meetings, seminars, journal club and other events organized by the team of the Dense and Strange Hadronic Matter Group. The engagement of the Professor and the colleagues enriches the curriculum of Bachelor students like me with unique lectures, FoPras and research projects in a way not offered by any other group.

My special gratitude goes out to my supervisor, Dr. Chiara Pinto, who provided her guidance and support during the whole time that I have been working on the analysis and this thesis. She has shown nothing but genuine care about the project and has always been interested in helping me with any questions and challenges of the analysis, being open for communication and even often using her own free time to think about the challenges that were facing us at that moment and coming up with solutions. Her expertise has been invaluable to me and to this study.

I also want to thank the antinuclei group of TUM. In particular, I thank Dr. Luca Barioglio for providing helpful insights into ROOT, C++ and the ideas behind light (anti)nuclei production studies, as well as for operating my trains used to extract the data and simulations from the ALICE Grid. I am grateful to Maximilian Horst for his engagement with EPOS simulation of Xe–Xe system and for providing me with the results, as well as for his comments on this thesis. I also want to thank Berkin Ulukutlu, who prepared the figure shown on the cover page of this thesis (event display of a Xe-Xe collision) and also offered his advanced LaTeX template. I appreciate the friendly interactions that I had with him.

Last but not least, I thank my parents for their unconditional affection and support.

7 Appendix

Functions used for yield extrapolation

- Levy-Tsallis:

$$\frac{\mathrm{d}^2N}{\mathrm{d}y\,\mathrm{d}p_\mathrm{T}} = A_\mathrm{LT}\,p_\mathrm{T}\left[1-(1-q)\frac{p_T}{T}\right]^{\frac{1}{1-q}}$$

- Boltzmann:

$$\frac{\mathrm{d}^2N}{\mathrm{d}y\,\mathrm{d}p_\mathrm{T}} = A_\mathrm{B}\,p_\mathrm{T}\,m_\mathrm{T}e^{-m'_\mathrm{T}/T_\mathrm{B}}$$

- Fermi-Dirac:

$$\frac{\mathrm{d}^2N}{\mathrm{d}y\,\mathrm{d}p_\mathrm{T}} = A_\mathrm{FD}\,p_\mathrm{T}\left(e^{m'_\mathrm{T}/T_\mathrm{FD}}+1\right)^{-1}$$

- Bose-Einstein

$$\frac{\mathrm{d}^2N}{\mathrm{d}y\,\mathrm{d}p_\mathrm{T}} = A_\mathrm{BE}\,p_\mathrm{T}\left(e^{m'_\mathrm{T}/T_\mathrm{BE}}-1\right)^{-1}$$

- m_T-exponential:

$$\frac{\mathrm{d}^2N}{\mathrm{d}y\,\mathrm{d}p_\mathrm{T}} = A_\mathrm{mt}\,p_\mathrm{T}e^{-m'_\mathrm{T}/T_\mathrm{mt}}$$

- modified power law:

$$\frac{\mathrm{d}^2N}{\mathrm{d}y\,\mathrm{d}p_\mathrm{T}} = A_\mathrm{PL}\,p_\mathrm{T}\left(1+\left(\frac{p_\mathrm{T}}{p_0}\right)^2\right)^{-n}$$

Where p_T is transverse momentum, m_T is transverse mass: $m_\mathrm{T} = \sqrt{m^2+p_\mathrm{T}^2}$ and m'_T is modified transverse mass with an additional parameter p_0: $m'_\mathrm{T} = \sqrt{m^2+(p_\mathrm{T}+p_0)^2}$. The other quantities represent free parameters.

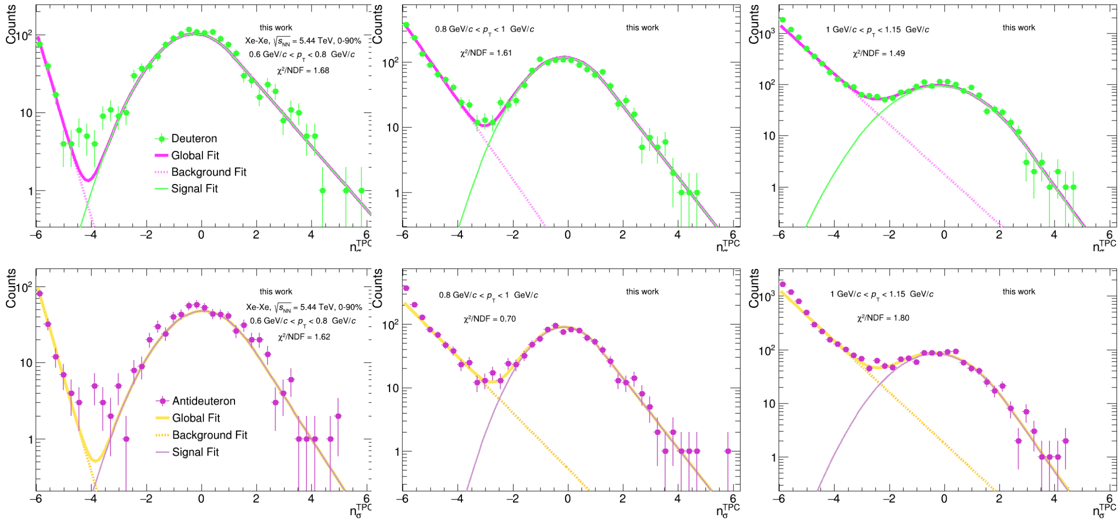

Figure 7.1: Deuterons (green datapoints and purple background) and antideuterons (purple datapoints and yellow background) signal extraction with the TPC in the transverse momentum region 0.6 GeV/c $\leq p_{\mathrm{T}} \leq$ 1.15 GeV/c

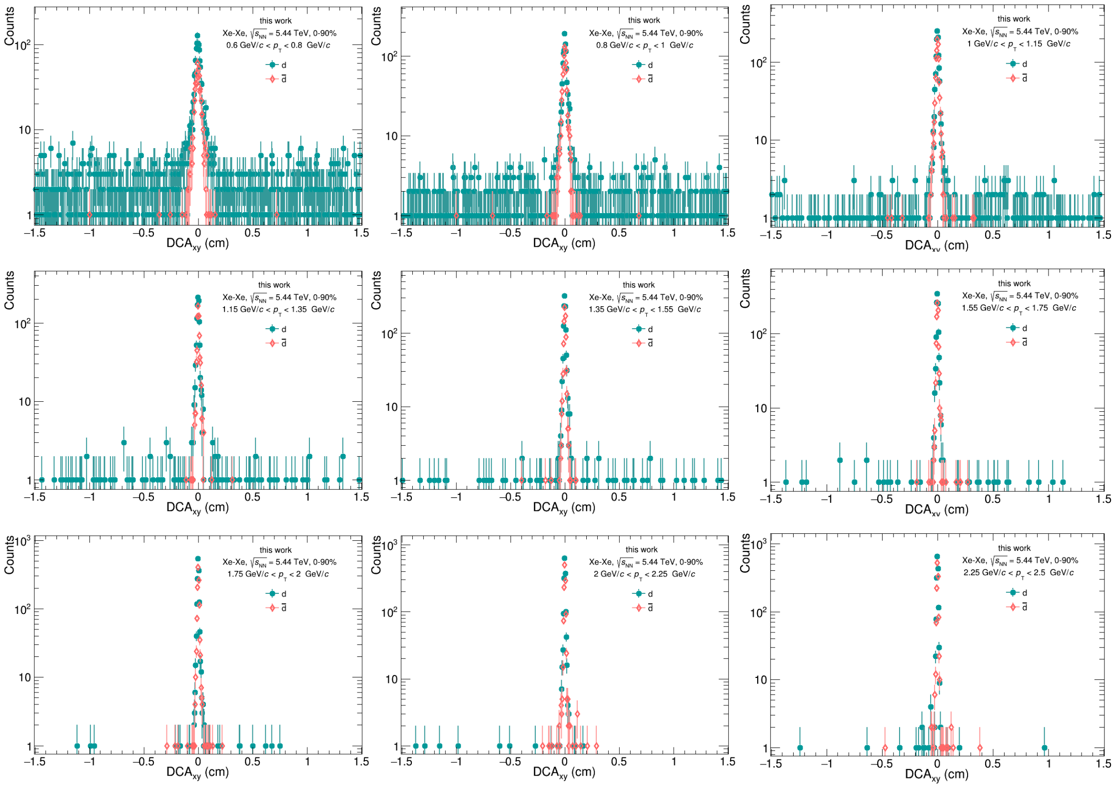

Figure 7.2: DCA$_{xy}$ distributions of deuterons (teal cirlces) and antideuterons (light pink diamonds) in the transverse momentum region 0.6 GeV/c $\leq p_{\mathrm{T}} \leq$ 2.5 GeV/c. Contribuion of the secondary nuclei is neglected starting from $p_{\mathrm{T}} = 1.8$ GeV/c

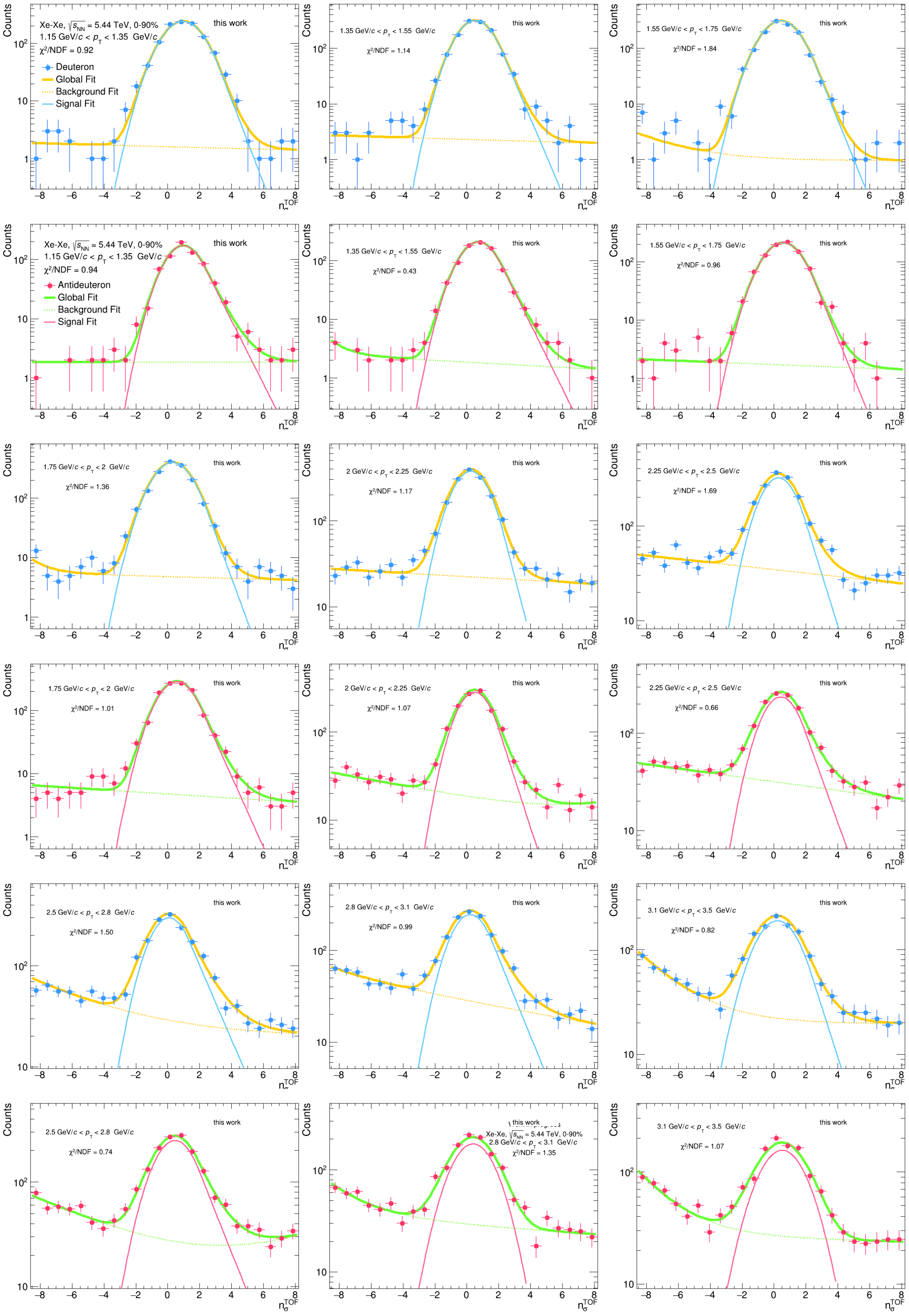

Figure 7.3: Deuterons (blue datapoints and signal fit, orange background) and antideuterons (pink datapoints and signal fit, green background) signal extraction with the TOF in the transverse momentum region 1.15 GeV/c $\leq p_T \leq$ 3.50 GeV/c

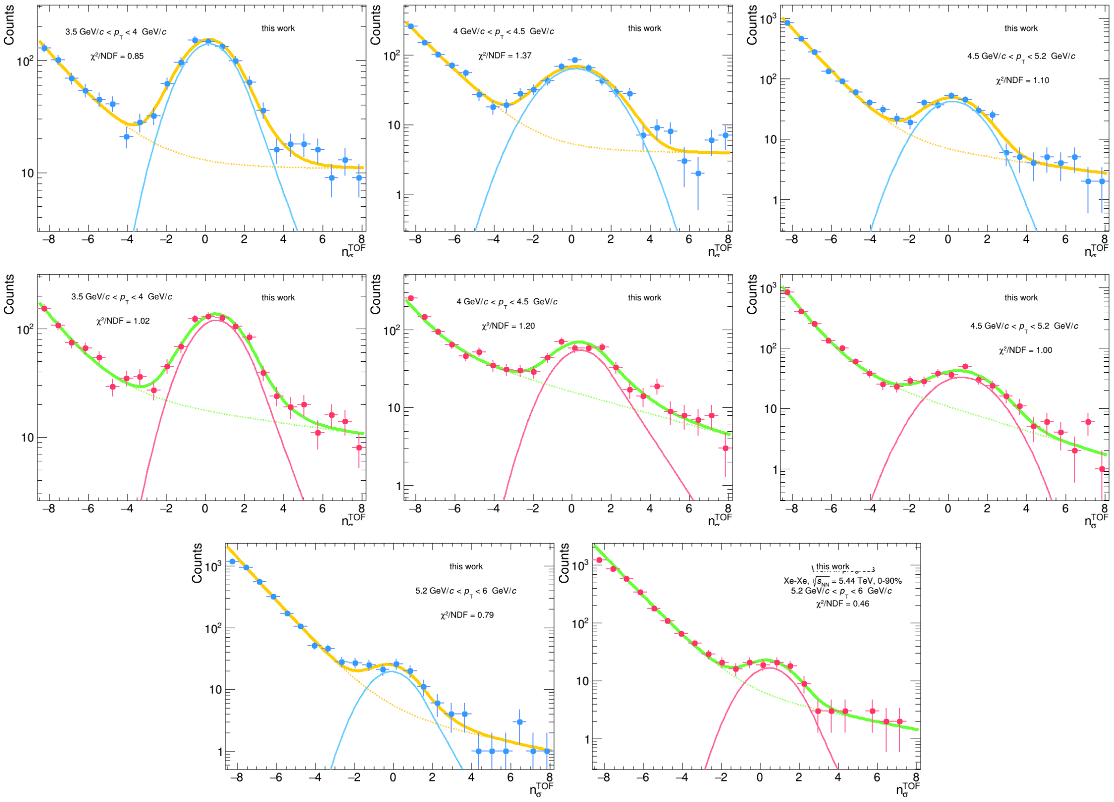

Figure 7.4: Deuterons (blue datapoints and signal fit, orange background) and antideuterons (pink datapoints and signal fit, green background) signal extraction with the TOF in the transverse momentum region 3.50 GeV/c $\leq p_{\mathrm{T}} \leq$ 6.0 GeV/c

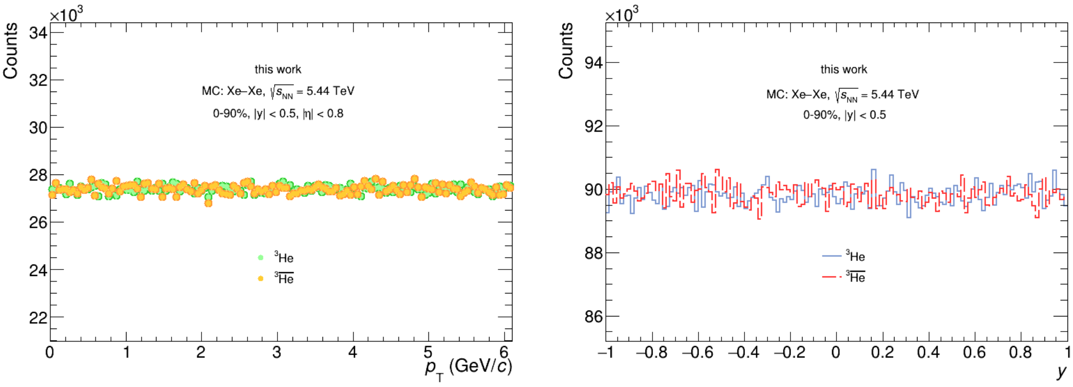

Figure 7.5: Transverse momentum distributions (*left*) and rapidity distribution (*right*) of the generated helions from a dedicated Monte Carlo simulation.

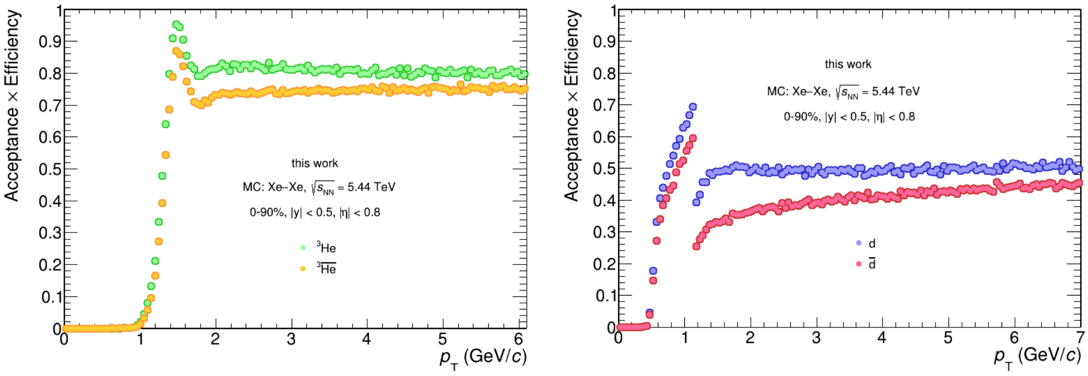

Figure 7.6: Acceptance × efficiency of the detector in narrow bins for (anti)helions (*left*) and (anti)deuterons (*right*) obtained from a dedicated Monte Carlo production.

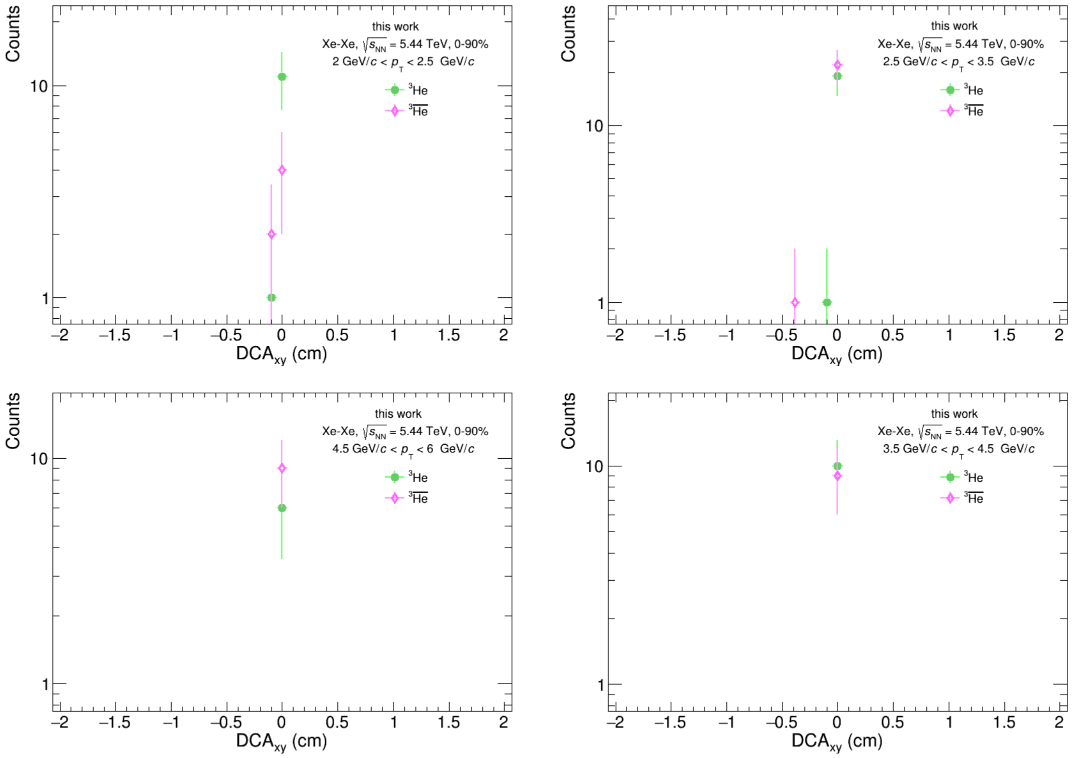

Figure 7.7: DCA$_{xy}$ distributions of helions (GREEN cirlces) and antideuterons (light pink diamonds) in the transverse momentum region 0.6 GeV/c $\leq p_{\mathrm{T}} \leq$ 2.5 GeV/c. Contribuion of the secondary nuclei is neglected.

Uncertainty	$\left({}^{3}\mathrm{He}+{}^{3}\overline{\mathrm{He}}\right)/2$	$(\mathrm{d}+\overline{\mathrm{d}})/2$	$(\mathrm{p}+\overline{\mathrm{p}})/2$
Statistical	15.0%	1.1%	0.2%
uncorrelated	4.28%	1.92%	(assumed correlated)
correlated	4.59%	4.61%	9.63%
shape	8.95%	1.78%	0.81%
Systematic	10.9%	5.3%	9.67%

Table 7.1: Summary of uncertainties of proton, deuteron, and helion yields. Systematic uncertainties of protons were conservatively assumed to be correlated due to the missing knowledge of the uncorrelated part.

List of Figures

List of Tables

Bibliography

[1] D. N. Spergel, L. Verde, H. V. Peiris, et al. "First-Year Wilkinson Microwave Anisotropy Probe (WMAP) Observations: Determination of Cosmological Parameters". In: *The Astrophysical Journal Supplement Series* 148.1 (Sept. 2003), pp. 175–194. DOI: `10.1086/377226`.

[2] A. Boveia and C. Doglioni. "Dark Matter Searches at Colliders". In: *Annual Review of Nuclear and Particle Science* 68.1 (Oct. 2018), pp. 429–459. DOI: `10.1146/annurev-nucl-101917-021008`. URL: `https://doi.org/10.1146%2Fannurev-nucl-101917-021008`.

[3] O. Buchmueller, C. Doglioni, and L.-T. Wang. "Search for dark matter at colliders". In: *Nature Physics* 13.3 (Mar. 2017), pp. 217–223. DOI: `10.1038/nphys4054`. URL: `https://doi.org/10.1038%2Fnphys4054`.

[4] P. von Doetinchem, K. Perez, T. Aramaki, et al. "Cosmic-ray antinuclei as messengers of new physics: status and outlook for the new decade". In: *Journal of Cosmology and Astroparticle Physics* 2020.08 (Aug. 2020), pp. 035–035. DOI: `10.1088/1475-7516/2020/08/035`.

[5] A. Kounine. "The Alpha Magnetic Spectrometer on the International Space Station". In: *Int. J. Mod. Phys. E* 21.08 (2012), p. 1230005. DOI: `10.1142/S0218301312300056`.

[6] S. Ting. "Latest Results from the AMS Experiment on the International Space Station". In: (2018). URL: `https://cds.cern.ch/record/2320166`.

[7] G. Bertone, D. Hooper, and J. Silk. "Particle dark matter: evidence, candidates and constraints". In: *Physics Reports* 405.5-6 (Jan. 2005), pp. 279–390. DOI: `10.1016/j.physrep.2004.08.031`. URL: `https://doi.org/10.1016Fj.physrep.2004.08.031`.

[8] B. Ratra and M. S. Vogeley. "The Beginning and Evolution of the Universe". In: *Publications of the Astronomical Society of the Pacific* 120.865 (Mar. 2008), pp. 235–265. DOI: `10.1086/529495`. URL: `https://doi.org/10.1086F529495`.

[9] *QCD phase diagram.* `https://cds.cern.ch/record/2729160`. Accessed: 04.10.2022.

[10] P. Braun-Munzinger, K. Redlich, and J. Stachel. "Particle production in heavy ion collisions". In: (Apr. 2003). Ed. by R. C. Hwa and X.-N. Wang, pp. 491–599. DOI: `10.1142/9789812795533_0008`. arXiv: `nucl-th/0304013`.

[11] J. Adam, D. Adamova, M. M. Aggarwal, et al., ALICE Collaboration. "Production of light nuclei and anti-nuclei in *pp* and Pb-Pb collisions at energies available at the CERN Large Hadron Collider". In: *Phys. Rev. C* 93 (Feb. 2016), 024917. 20 p. DOI: `10.1103/PhysRevC.93.024917`. arXiv: `1506.08951`. URL: `https://cds.cern.ch/record/2030480`.

[12] C. Pinto. "Light (anti)nuclei production with ALICE at the Large Hadron Collider". PhD thesis. 2021. URL: `https://cds.cern.ch/record/2801260`.

[13] S. Acharya, D. Adamová, S. Adhya, et al. "Multiplicity dependence of light (anti-)nuclei production in p–Pb collisions at $\sqrt{s_{\mathrm{NN}}} = 5.02$ TeV". In: *Physics Letters B* 800 (2020), p. 135043. ISSN: 0370-2693. DOI: `https://doi.org/10.1016/j.physletb.2019.135043`. URL: `https://www.sciencedirect.com/science/article/pii/S0370269319307658`.

[14] F. Bellini. "Testing the system size dependence of hydrodynamical expansion and thermal particle production with π, K, p, and ϕ in Xe-Xe and Pb-Pb collisions with ALICE". In: *Nucl. Phys. A* 982 (2019). Proceedings of the XXVIIth International Conference on Ultrarelativistic Nucleus-Nucleus Collisions (Quark Matter 2018), 4 pages, 5 figures, 427–430. 4 p. DOI: `10.1016/j.nuclphysa.2018.09.082`. arXiv: `1808.05823`. URL: `https://cds.cern.ch/record/2635029`.

[15] A. Andronic, P. Braun-Munzinger, K. Redlich, and J. Stachel. "Decoding the phase structure of QCD via particle production at high energy". In: *Nature* 561.7723 (Sept. 2018), pp. 321–330. DOI: `10.1038/s41586-018-0491-6`. URL: `https://doi.org/10.1038/s41586-018-0491-6`.

[16] T. Bhattacharya, M. I. Buchoff, N. H. Christ, et al. "QCD Phase Transition with Chiral Quarks and Physical Quark Masses". In: *Phys. Rev. Lett.* 113 (8 Aug. 2014), p. 082001. DOI: `10.1103/PhysRevLett.113.082001`. URL: `https://link.aps.org/doi/10.1103/PhysRevLett.113.082001`.

[17] J. I. Kapusta. "Mechanisms for deuteron production in relativistic nuclear collisions". In: *Phys. Rev. C* 21 (4 Apr. 1980), pp. 1301–1310. DOI: `10.1103/PhysRevC.21.1301`. URL: `https://link.aps.org/doi/10.1103/PhysRevC.21.1301`.

[18] M. Schaumann, R. Alemany-Fernández, P. Baudrenghien, et al. "First Xenon-Xenon Collisions in the LHC". In: (2018), MOPMF039. 4 p. DOI: `10.18429/JACoW-IPAC2018-MOPMF039`. URL: `https://cds.cern.ch/record/2648699`.

[19] R. Alemany-Fernández, S. Albright, O. Andujar, et al. "Performance of the CERN Low Energy Ion Ring (LEIR) with Xenon beams". In: (2018), TUPAF020. 4 p. DOI: `10.18429/JACoW-IPAC2018-TUPAF020`. URL: `http://cds.cern.ch/record/2648426`.

[20] *LHC report: xenon in action.* `https://home.cern/news/news/accelerators/lhc-report-xenon-action`. Accessed: 03.10.2022.

[21] *The CERN accelerator complex.* `http://cds.cern.ch/record/2197559/files/?docname=CCC-v2017&version=all`. Accessed: 03.10.2022.

[22] B. B. Abelev, A. Abramyan, J. Adam, et al., ALICE Collaboration. "Performance of the ALICE Experiment at the CERN LHC". In: *Int. J. Mod. Phys. A* 29 (2014), 1430044. 120 p. DOI: `10.1142/S0217751X14300440`. arXiv: `1402.4476`. URL: `https://cds.cern.ch/record/1648854`.

[23] B. Abelev, J. Adam, D. Adamová, et al. "Centrality determination of Pb-Pb collisions at $\sqrt{s_{NN}} = 2.76$ TeV with ALICE". In: *Phys. Rev. C* 88 (4 Oct. 2013), p. 044909. DOI: `10.1103/PhysRevC.88.044909`. URL: `https://link.aps.org/doi/10.1103/PhysRevC.88.044909`.

[24] S. Acharya, F. Torales - Acosta, D. Adamova, et al. "Centrality and pseudorapidity dependence of the charged-particle multiplicity density in Xe–Xe collisions at $\sqrt{s_{NN}}$ = 5.44 TeV". In: *Phys. Lett. B* 790 (Mar. 2019), 35–48. 14 p. DOI: `10.1016/j.physletb.2018.12.048`. arXiv: `1805.04432`. URL: `http://cds.cern.ch/record/2316786`.

[25] S. Acharya, D. Adamova, A. Adler, et al., ALICE Collaboration. "Production of pions, kaons, (anti-)protons and ϕ mesons in Xe–Xe collisions at $\sqrt{s_{\mathrm{NN}}} = 5.44$ TeV". In: *Eur. Phys. J. C* 81 (July 2021), 584. 27 p. DOI: `10.1140/epjc/s10052-021-09304-4`. arXiv: `2101.03100`. URL: `https://cds.cern.ch/record/2748271`.

[26] D. Leermakers. "Systematic study of track quality cuts at ALICE". In: (2015). URL: `https://cds.cern.ch/record/2045797`.

[27] S. Agostinelli, J. Allison, K. Amako, et al. "Geant4—a simulation toolkit". In: *Nuclear Instruments and Methods in Physics Research Section A: Accelerators, Spectrometers, Detectors and Associated Equipment* 506.3 (2003), pp. 250–303. ISSN: 0168-9002. DOI: `https://doi.org/10.1016/S0168-9002(03)01368-8`. URL: `https://www.sciencedirect.com/science/article/pii/S0168900203013688`.

[28] X.-N. Wang and M. Gyulassy. "HIJING: A Monte Carlo model for multiple jet production in pp, pA, and AA collisions". In: *Phys. Rev. D* 44 (11 Dec. 1991), pp. 3501–3516. DOI: `10.1103/PhysRevD.44.3501`. URL: `https://link.aps.org/doi/10.1103/PhysRevD.44.3501`.

[29] H. Kamada, J. Golak, K. Miyagawa, et al. "π-mesonic decay of the hypertriton". In: *Physical Review C* 57.4 (Apr. 1998), pp. 1595–1603. DOI: `10.1103/physrevc.57.1595`. URL: `https://doi.org/10.1103/Physrevc.57.1595`.

[30] *DPG - Analysis Object Tools - Systematic uncertainties on TPC-ITS matching in various Run-2 data samples.* `https://twiki.cern.ch/twiki/bin/view/ALICE/AliDPGtoolsTrackSystematicUncertaintyBookkeping`. Accessed: 01.10.2022.

[31] T. Pierog, I. Karpenko, J. M. Katzy, et al. "EPOS LHC: Test of collective hadronization with data measured at the CERN Large Hadron Collider". In: *Phys. Rev. C* 92 (3 Sept. 2015), p. 034906. DOI: `10.1103/PhysRevC.92.034906`. URL: `https://link.aps.org/doi/10.1103/PhysRevC.92.034906`.

[32] M. Kachelrieß, S. Ostapchenko, and J. Tjemsland. "Alternative coalescence model for deuteron, tritium, helium-3 and their antinuclei". In: *The European Physical Journal A* 56.1 (Jan. 2020). DOI: `10.1140/epja/s10050-019-00007-9`. URL: `https://doi.org/10.1140%2Fepja%2Fs10050-019-00007-9`.

[33] S. Acharya, D. Adamová, A. Adler, and J. Adolfsson. "Production of light (anti)nuclei in pp collisions at $\sqrt{s_{\mathrm{NN}} = 5.02 \text{ TeV}}$". In: *The European Physical Journal C* 82.4 (Apr. 2022). DOI: `10.1140/epjc/s10052-022-10241-z`. URL: `https://doi.org/10.1140%2Fepjc%2Fs10052-022-10241-z`.

[34] B. Abelev, J. Adam, D. Adamová, et al. *Upgrade of the ALICE Experiment: Letter of Intent.* Tech. rep. Geneva: CERN, 2014. DOI: `10.1088/0954-3899/41/8/087001`. URL: `https://cds.cern.ch/record/1475243`.

[35] P. Buncic, M. Krzewicki, and P. Vande Vyvre. *Technical Design Report for the Upgrade of the Online-Offline Computing System.* Tech. rep. 2015. URL: `https://cds.cern.ch/record/2011297`.